Charge Losses in Silicon Sensors and Electric-Field Studies at the Si-SiO_2 Interface

Dissertation
zur Erlangung des Doktorgrades
des Fachbereichs Physik
der Universität Hamburg

vorgelegt von
Thomas Pöhlsen

aus Hamburg

Hamburg 2013

Gutachter der Dissertation:

- Prof. Dr. Robert Klanner, Institut für Experimental Physik, Universität Hamburg, Luruper Chaussee 149, 22761 Hamburg, Germany
- Prof. Dr. Heinz Graafsma, Deutsches Elektronen-Synchrotron (FS-DS), Notkestrasse 85, 22607 Hamburg, Germany

Gutachter der Disputation:

- Prof. Dr. Erika Garutti, Institut für Experimental Physik, Universität Hamburg, Luruper Chaussee 149, 22761 Hamburg, Germany
- Prof. Dr. Eckhard Elsen, Deutsches Elektronen-Synchrotron (FH1), Notkestrasse 85, 22607 Hamburg, Germany

Datum der Disputation: 19.06.2013
Vorsitzender des Prüfungsausschusses: Dr. Georg Steinbrück
Vorsitzender des Promotionsausschusses: Prof. Dr. Peter Hauschildt
Leiterin des Fachbereichs Physik: Prof. Dr. Daniela Pfannkuche

Abstract

Electric fields and charge losses in silicon sensors before and after irradiation with x-rays, protons, neutrons or mixed irradiation are studied in charge-collection measurements. Electron-hole pairs (*eh* pairs) are generated at different positions in the sensor using sub-ns pulsed laser light of different wavelengths. Light of 1063 nm, 830 nm and 660 nm wavelength is used to generate *eh* pairs along the whole sensor depth, a few µm below the surface and very close to the surface, respectively.

Segmented p^+n silicon strip sensors are used to study the electric field below the SiO_2 separating the strip implants. The sensors are investigated before and after irradiation with 12 keV x-rays to a dose of 1 MGy. It is found that the electric field close to the Si-SiO_2 interface depends on both the irradiation dose and the biasing history. For the non-irradiated sensors the observed dependence of the electric field on biasing history and humidity is qualitatively as expected from simulations of the electrostatic potential for different boundary conditions at the surface. Depending on the biasing history incomplete collection of electrons, full charge collection or incomplete collection of holes is observed. After the bias voltage is changed, the amount of observed charge losses is time dependent with time constants being a function of humidity. For the irradiated sensors an increased effective oxide charge density and more electron losses are observed compared to the non-irradiated sensors.

Due to positive oxide charges which are always present at the Si-SiO_2 interface an electron-accumulation layer forms, if the oxide charge is not compensated by charges on top of the passivation. If negative charges overcompensate the oxide charge, a hole-accumulation layer forms. In both cases the number of accumulated charges can be temporarily increased by incomplete charge collection of either electrons or holes. How many additional charge carriers can be added to the accumulation layer and when the accumulation layer returns to steady state is investigated.

Irradiated silicon pad sensors are used to study the charge-collection efficiency (CCE) of charge carriers generated using laser light of 1063 nm wavelength, as a function of bulk material, active sensor thickness, voltage, temperature, particle type (for the irradiation) and fluence. As a cross check the CCE is also determined for charge carriers generated by electrons from a ^{90}Sr-source. A precision of 3 % in the CCE is achieved. Sensors of n-doped and p-doped silicon are compared, as well as sensors of different crystal-growing methods (magnetic Czochralski (MCz) and float zone (FZ)). The sensor thickness varies from 200 µm (MCz and FZ) to 320 µm (FZ). The 320 µm thick FZ sensors underwent a dopant-diffusion process (dd-FZ) to reduce the active sensor thickness. For the irradiation both protons of different energies (23 MeV and 23 GeV) and reactor neutrons (∼1 MeV) are used. The achieved fluences are between $3 \cdot 10^{14}$ cm^{-2} and $1.3 \cdot 10^{16}$ cm^{-2} 1 MeV-neutron equivalent.

The CCE is used to calculate the signal corresponding to a minimum-ionising particle (mip) traversing the sensor and to calculate the effective distance the generated charge carriers drift. While little difference in CCE between the 200 µm thick MCz and FZ materials is found, the dd-FZ materials of both ∼200 µm and ∼300 µm active thickness have a lower CCE, corresponding also to a shorter effective drift distance. The CCE and the effective drift distance are also calculated for *eh* pairs generated close to the sensor surface using laser light of 660 nm wavelength. The measurements are not compatible with a position-independent trapping probability, and qualitative agreement with a position-dependent occupation of radiation-induced trapping centres due to the dark current is found.

Zusammenfassung

Elektrische Felder und Ladungsträgerverluste in Siliziumzählern vor und nach Bestrahlung mit Röntgenlicht, Protonen, Neutronen oder gemischter Bestrahlung werden mittels Ladungssammlungsmessungen untersucht. Sub-ns gepulstes Laserlicht unterschiedlicher Wellenlänge λ wird benutzt, um Elektronen-Loch-Paare (EL-Paare) entlang der ganzen Zählertiefe ($\lambda =$ 1063 nm), wenige µm unterhalb der Oberfläche ($\lambda =$ 830 nm) oder direkt unterhalb der Oberfläche ($\lambda =$ 660 nm) zu erzeugen.

In segmentierten p^+n Siliziumstreifenzählern wird das elektrische Feld unterhalb des SiO_2 untersucht, welches die Streifenimplantierungen trennt. Zähler vor und nach Bestrahlung mit 12 keV Röntgenlicht werden untersucht und es werden Abhängigkeiten der Bestrahlungsdosis, der Luftfeuchtigkeit und der Spannungshistorie festgestellt. Für den nicht-bestrahlten Zähler werden die Effekte durch Simulationen erklärt, in denen verschiedene Randbedingungen an der Zähleroberfläche angenommen werden. Dabei wird sowohl unvollständige Sammlung von Elektronen, vollständige Ladungssammlung und unvollständige Sammlung von Löchern beschrieben. Nachdem die angelegte Spannung geändert wird, entwickeln sich die Ladungsverluste zeitlich mit Zeitkonstanten, die von der Luftfeuchtigkeit abhängen.

Aufgrund der positiven Oxidladung, die sich immer an der Si-SiO_2-Grenzschicht befindet, bildet sich eine Elektronenakkumulationsschicht, falls die Oxidladung nicht durch Oberflächenladungen auf der Passivierung kompensiert wird. Falls negative Ladungen die Oxidladung überkompensieren, bildet sich eine Löcherakkumulationsschicht. In beiden Fällen kann die Anzahl der akkumulierten Ladungsträger zeitweise erhöht werden. Es wird untersucht, wie viele Ladungsträger zur Akkumulationsschicht hinzugefügt werden können und wie lange es dauert bis die Akkumulationsschicht wieder ihren Gleichgewichtszustand erreicht.

In bestrahlte Siliziumflächenzählern wird die Ladungssammlungseffizienz (CCE) von Ladungsträgern, die mit Laserlicht der Wellenlänge 1063 nm erzeugt werden, in Abhängigkeit des Siliziummaterials, der aktiven Zählerdicke, der angelegten Spannung der Temperatur, der zur Bestrahlung verwendeten Teilchenart und der Fluenz bestimmt. Als Gegenprobe wird die CCE auch in einem weiteren Versuchsaufbau bestimmt, in dem die Ladungsträger durch Elektronen einer ^{90}Sr-Quelle erzeugt werden. Die erreichte Genauigkeit auf die Werte der CCE beträgt 3 %. Sowohl n-dotiertes und p-dotiertes Silizium, als auch unterschiedliche Methoden Siliziumkristalle herzustellen (Magnetic-Czochralski (MCz) und Float-Zone (FZ)) werden verglichen. Die verwendeten Zählerdicken sind 200 µm (MCz, FZ) und 320 µm (FZ). Auf die 320 µm FZ-Zähler wurde zusätzlich ein Diffusionsprozess von Dotierungsatomen angewendet (dd-FZ), um die aktive Zählerdicke zu reduzieren. Für die Bestrahlung der Zähler werden sowohl Protonen unterschiedlicher Energien (23 MeV und 23 GeV) also auch Reaktorneutronen ($\sim$1 MeV) verwendet. Die erreichten Fluenzen liegen zwischen $3 \cdot 10^{14}$ cm^{-2} und $1.3 \cdot 10^{16}$ cm^{-2} in 1 MeV Neutronenäquivalent.

Aus der CCE wird das Signal berechnet, das einem minimal-ionisierenden Teilchen entspricht, welches den Zähler durchquert. Während für die 200 µm dicken MCz- und FZ-Zähler kaum Unterschiede beobachtet werden, ist die CCE für die 200 µm dicken dd-FZ-Zähler niedriger. Dies entspricht einer kürzeren effektiv zurückgelegten Strecke der Ladungsträger. Die CCE und die effektiv zurückgelegte Strecke werden auch für EL-Paare berechnet, die direkt unterhalb der Zähleroberflächen durch Licht der Wellenlänge 660 nm erzeugt werden. Die Messungen sind nicht mit einer Positionsunabhängigen Ladungseinfangswahrscheinlichkeiten vereinbar und die Abweichungen stimmen qualitativ mit unterschiedlichen Besetzungswahrscheinlichkeiten der einfangenden Defekte aufgrund des Dunkelstroms überein.

Contents

Chapter 1

Introduction

Silicon sensors are used for radiation detection in many applications. Typical examples are the European X-Ray Free-Electron Laser (X-FEL) [1, 2] which is currently under construction at DESY [3] in Hamburg, and the Large Hadron Collider (LHC) [4] at the European Organization for Nuclear Research (CERN) [5] in Geneva.

The European X-FEL is a research facility which will generate extremely intense X-ray pulses [1, 2]. Photon densities of up to 10^4 photons per pixel and pulse of typically 12.4 keV in ∼100 fs are a challenge for the detector system, which also needs to separate single photons from noise. For the high dynamic range an adaptive gain integrating pixel detector (AGIPD) is foreseen [6, 7]. For the silicon sensors, a high operation voltage is required in order to provide sufficiently fast charge collection also for high densities of generated *eh* pairs [8]. At the same time, sensors at the X-FEL will experience x-ray radiation damage with doses of up to 1 GGy [9], potentially causing low breakdown voltages if the sensors are not optimised for high doses [10, 11]. In order to achieve sufficiently high bias voltages it is essential to optimise the sensor layout close to the sensor surface, since this region and its passivating SiO_2 layers are most relevant for the sensor stability. After silicon sensors are introduced in Chapter 2, and information on the experimental methods are given in Chapter 3, the transient current technique (TCT) is used in Chapter 4 to investigate the electric-field distribution in this region and the accumulation of charge carriers at the Si-SiO_2 interface, and to learn how they depend on the humidity and on the biasing history.

The LHC is a proton-proton collider which has been built to uncover fundamental questions in particle physics, and in order to test and possibly extend the standard model of particle physics which describes interactions at the smallest scales. For the analysis of the data taken at the LHC experiments, many collision events are required, creating a challenge for the silicon trackers due to significant radiation damage. For the silicon sensors crystal damage in the sensor bulk is especially relevant. In Chapter 5, charge collection in sensors of different silicon bulk materials is investigated. The studied materials are possible candidates for the strip tracker of the Compact Muon Solenoid (CMS) [12, 13] experiment at the LHC, after a foreseen high-luminosity upgrade in ∼2022.

Chapter 2

Silicon sensors

In this chapter the principles of silicon sensors which are the most relevant for this work, will be presented. The chapter is based on Refs. [14, 15, 16, 17, 18]. Parts are also taken from my diploma thesis [19].

2.1 The working principle

Silicon sensors "are essentially solid state ionisation chambers" [15]. Particles traversing the silicon generate electron-hole pairs (eh pairs) by ionisation, which move towards the electrodes due to an applied bias voltage as illustrated in Figure 2.1. On the electrodes they induce a current pulse which can be measured.

For visible light typically one eh pair per photon is generated and many photons are needed in order to obtain a measurable signal. For high energetic photons ($E > 1.5$ keV) many eh pairs are generated, and on average 3.67 eV is needed to generate one eh pair [15]. The number of eh pairs generated by minimum-ionizing particles depends on the ionisation-energy loss and may be described by a Landau distribution. The most probable amount of eh pairs generated along the trajectory in a 300 µm thick silicon sensor is 22 000 [15]. In thinner sensors fewer eh pairs are generated.

For particle tracking typically segmented sensors are used with either strip or pixel electrodes. The signals from the different electrodes are amplified and processed, and the position of the particle track is reconstructed.

2.1.1 p-n junction and depletion width

A key element of silicon sensors is a p-n junction making it possible to deplete the sensor from free charge carriers so that the small signals can be detected. The p-n junction is discussed in detail elsewhere [17, 14] and only the most important features are summarised here.

The band structure of semiconductors is characterised by the energy gap between valence band and conduction band. For silicon the energy gap at room temperature is approximately 1.12 eV. The silicon can be doped by replacing some of the silicon atoms by either donors

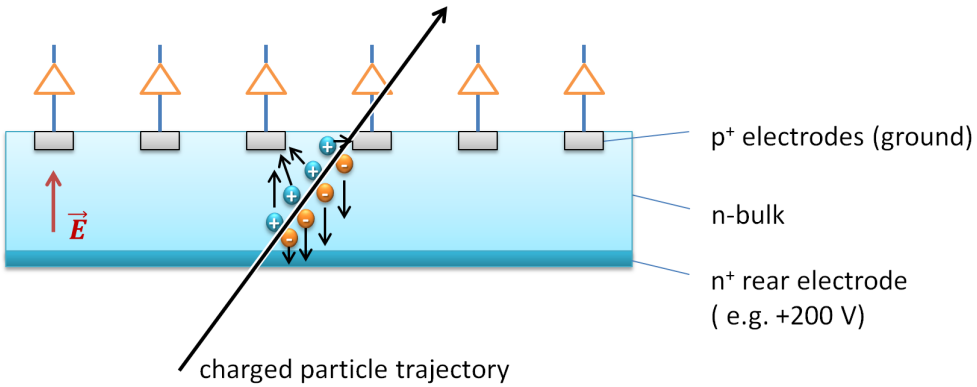

Figure 2.1: Principle of a silicon detector. The schematic cross section of a p-on-n silicon strip sensor is shown, *eh* pairs are generated along the trajectory of a charged particle and are collected at the electrodes due to the applied bias voltage and local electric fields.

(n-type silicon) or by acceptors (p-type silicon). Donors have five valence electrons. Four of these electrons will form the covalent bonding to the neighbouring silicon atoms while the fifth electron is only loosely bound (∼45 meV ionisation energy for silicon doped with phosphor). In the energy band the donor with its electron corresponds to a filled state close to the conduction band. Its electron can be easily excited into the conduction band producing a free electron. At room temperature nearly all donor electrons will be excited. Acceptors have only three valence electrons and can accept a fourth electron. Their energy level is close to the valence band. At room temperature most of the acceptors are filled with electrons from the valence band leading to free holes.

If n-type silicon and p-type silicon are joined together free electrons of the n-type silicon will diffuse into the p-type silicon. In the same way free holes from the p-type region will diffuse into the n-type silicon. A steady state forms with negative space charge at the filled acceptor states in the p-type silicon and positive space charge at the free donor states in the n-type silicon.

Due to the space charge close to the p-n junction an electric field is created. According to Gauss' law we have

$$\vec{\nabla} \cdot \vec{E} = \frac{\rho}{\epsilon_{Si}\epsilon_0}, \tag{2.1}$$

with the space charge density, ρ, the vacuum permittivity, ϵ_0, and the relative permittivity for silicon, $\epsilon_{Si} = 11.9$ [15]. The electric field leads to a drift current of the free charge carriers opposing the diffusion of electrons and holes. The space without free charge carriers is called depleted and its space charge density ρ in units of elementary charge q_0 is the same as the doping concentration N.

For homogeneous doping and an abrupt p-n junction in planar pad sensors the electric field is linear in sensor depth with a slope proportional to the doping concentration as seen in Equation (2.1). If no bias voltage is applied, the integral of the electric field is called built-in voltage, V_{bi}, and is typically about 0.5 V [15]. The electric-field integral and the depletion

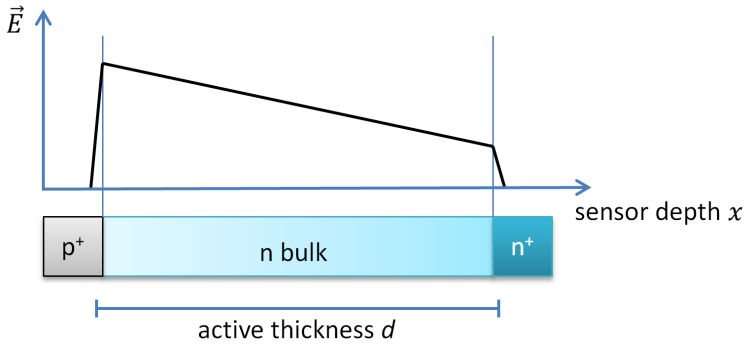

Figure 2.2: Typical doping structure and electric field of an n-type pad sensor. Highly doped p^+ and n^+ electrodes are shown, and a lightly doped n bulk.

width is decreased, if a forward bias is applied, and it is increased, if a reverse bias is applied. For the operation of sensors for particle detection typically a reverse bias voltage is used, in order to limit the dark current and to provide an electric field in the entire sensor which is needed for a fast signal collection.

For sensors typically an asymmetric structure is used, e.g. a highly doped p-electrode (p^+) and a lightly doped n-bulk [15]. Another highly doped electrode (n^+) is used to cut off the electric field at the otherwise only lightly doped sensor edge as illustrated in Figure 2.2. For an abrupt p^+-n junction with a donor concentration, N, and an applied reverse bias voltage, V, the depletion width, W, for a partially depleted diode is given by

$$W = \sqrt{\frac{2\epsilon\epsilon_0(V + V_{bi})}{q_0 N}} \qquad [15]. \tag{2.2}$$

Usually a reverse voltage V large compared to V_{bi} will be applied and the equation may be simplified to

$$W = \sqrt{\frac{2\epsilon\epsilon_0 V}{q_0 N}}\,. \tag{2.3}$$

The voltage needed for full depletion of a sensor with active thickness d is called the full-depletion voltage V_{fd}. For planar pad sensors it can be derived from Equation 2.3:

$$V_{fd} = \frac{d^2 q_0 N}{2\epsilon\epsilon_0}\,. \tag{2.4}$$

For $V \geq V_{fd}$ the sensor is fully depleted and the depletion width is equal to the active thickness of the diode, i.e. $W = d$. In this case d is assumed to be the width of the bulk material as illustrated in Figure 2.2 and the depletion into the highly doped electrodes is neglected.

2.1.2 Capacitance and current characteristics

Capacitance and sensor thickness

For non-irradiated planar sensors with active thickness d, pad area A and depletion width W the capacitance between pad and rear side is given by

$$C = \frac{dQ}{dV} = \epsilon\epsilon_0 \frac{A}{W} \qquad [17]. \tag{2.5}$$

For fully-depleted sensors with $W = d$ the active thickness of the sensor d can be derived from capacitance measurements and is given by

$$d = \epsilon\epsilon_0 \frac{A}{C}. \tag{2.6}$$

Due to irradiation-induced bulk defects the capacitance changes with irradiation and becomes frequency dependent. Usually d is determined only for pad sensors before irradiation.

Sensor current

Electron-hole pairs are thermally generated, dominantly at defects close to the middle of the band gap. If the electron-hole pairs are generated in the depleted region they contribute to the sensor current. Otherwise most of them will recombine. For an uniform current generation the current generated in the silicon bulk, I_{bulk}, is proportional to the depleted volume and hence approximately also to the sensor depth W. In this case I_{bulk} saturates for fully-depleted sensors.

2.2 Charge collection

2.2.1 Velocities of charge carriers

Charge carriers generated in the silicon bulk drift to the electrodes due to the local electric field which is mainly caused by the applied bias voltage. The drift velocity of a charge carrier, $\vec{v}_{dr}$, is a function of the electric field, $E(\vec{x})$, and is different for electrons and for holes as shown in Figure 2.3.

For low electric fields the drift velocity is proportional to the electric field, for high electric fields a saturation is observed. According to Jacoboni [20] the drift velocity may be parameterised as following:

$$v_{dr} = \frac{\mu_0 E}{\left(1 + (\frac{\mu_0 E}{v_{sat}})^{\beta}\right)^{1/\beta}}, \tag{2.7}$$

with the low-field mobility μ_0, the saturation velocity v_{sat} and the parameter β close to 1. All parameters, μ_0, v_{sat} and β are temperature dependent. Jacoboni investigated the drift velocity in <111>-oriented silicon.

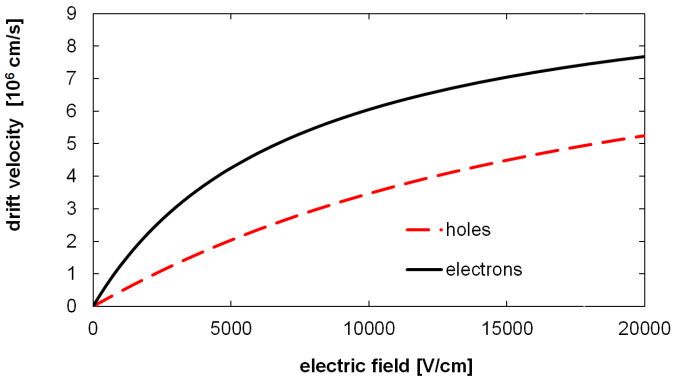

Figure 2.3: Drift velocity of electrons (solid line) and holes (dashed line) as a function of electric field. Values according to Ref. [21] for $T = 300$ K in <100>-oriented silicon.

In Ref. [21] v_{dr} is investigated for both <111>- and <100>-oriented silicon using the Jacoboni parameterisation. Values for the electron drift in <111> orientation are found to be in good agreement with [20]. For electron drift in the <100> direction different values are found, leading to smaller drift velocities. In Figure 2.3 the drift velocities for electrons and holes as a function of electric field are shown for <100>-oriented silicon and values according to Ref. [21] are shown .

Carrier drift mobility is studied in irradiated silicon up to fluences of a few 10^{14} cm^{-2} [22, 23]. No significant difference to non-irradiated silicon is found.

Diffusion

The thermal movement of free charge carriers leads to diffusion. The diffusion constant in equilibrium is given by $D = \mu kT/q_0$, with the mobility μ and the Boltzmann constant k, leading to a spread of the charge carriers with time t. In one dimension for an initially point-like distribution at $x = 0$ and $t = 0$, the distribution at each time $t > 0$ is proportional to $e^{-x^2/4Dt}$ [18].

2.2.2 Induced current and weighting potential

According to the Schockley-Ramo theorem [24, 25, 26] the induced current of a point charge q in a fully-depleted sensor is given by

$$I = q \cdot \vec{\nabla}\phi_w \cdot \vec{v}, \tag{2.8}$$

with the instantaneous velocity of the charge carrier, v, and the weighting potential, ϕ_w. The dimensionless weighting potential is a measure of the coupling of a test charge to the read-out electrode. It is 1 at the read-out electrode and 0 at all other electrodes in the case of DC coupled sensors. If only fixed charge carriers are present in the sensor bulk the weighting potential is equal to the electrostatic potential in Volts, for the case that 1 V is applied at the

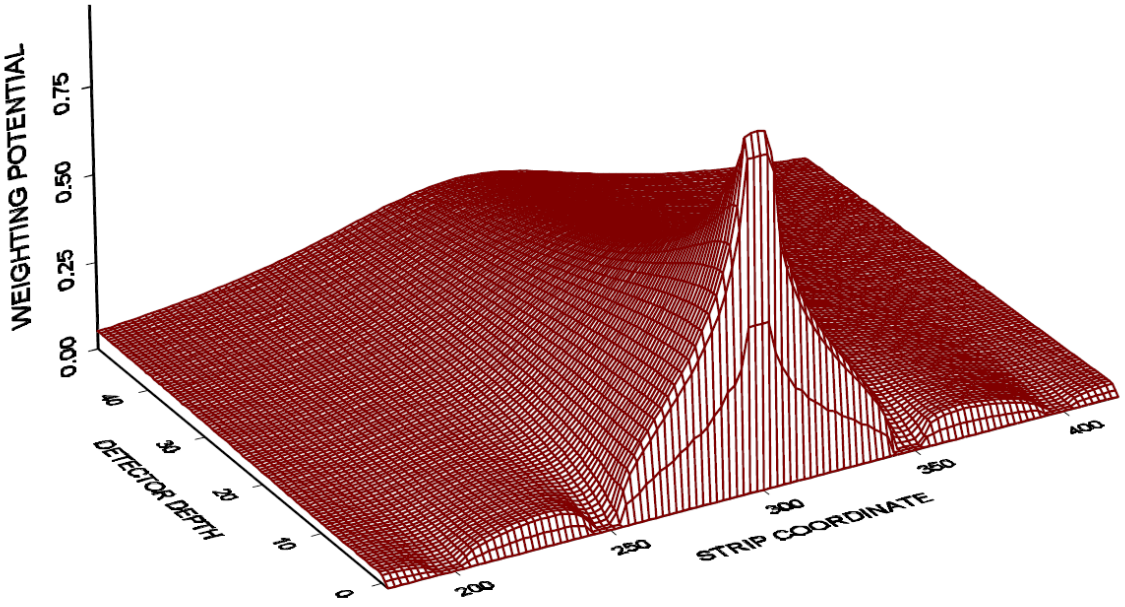

Figure 2.4: Weighting potential for a 300 µm thick strip sensor with 50 µm pitch taken from Ref. [28]. Only the first 50 µm of the sensor depth is shown.

read-out electrode and 0 V to all other electrodes. If polarisation of charges present in the sensor bulk is relevant, the weighting potential may be calculated according to Ref. [27].

For fully-depleted pad sensors with an active thickness d the weighting potential is linear in sensor depth and its gradient is constant with an absolute value of $\nabla\phi_w = \frac{1}{d}$. For segmented sensors the weighting potential is non-linear. An example of a weighting potential in a strip sensor is given in Figure 2.4.

Integrated signals The integrated signals Q_i on a read-out electrode i for a point charge q moving from position $\vec{a}$ to position $\vec{b}$ is given by

$$Q_i = \int_{t(\vec{a})}^{t(\vec{b})} I_i \, \mathrm{d}t = \int_{t(\vec{a})}^{t(\vec{b})} q \cdot \vec{\nabla}\phi_w^i \cdot \vec{v} \, \mathrm{d}t = q \cdot \int_{\vec{a}}^{\vec{b}} \vec{\nabla}\phi_w^i \, \mathrm{d}\vec{x} = q \cdot (\phi_w^i(\vec{b}) - \phi_w^i(\vec{a})). \tag{2.9}$$

Hence for integrated signals only the weighting potential at the start position $\vec{a}$ and the final position $\vec{b}$ is relevant.

2.2.3 Charge multiplication

Charge multiplication, sometimes also called avalanche effect, is the generation of further eh pairs by electrons or holes drifting in high electric fields. To be relevant in silicon sensors an electric field of $> 10^5$ V/cm is needed [19, 29, 16]. Charge multiplication for N drifting

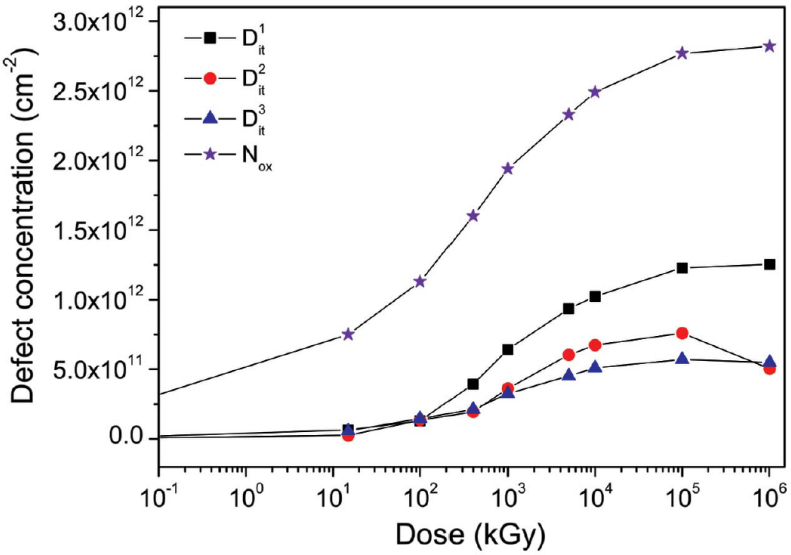

Figure 2.5: Fixed oxide-charge density N_{ox} and the three dominant X-ray-induced interface traps as a function of irradiation dose after annealing for 10 min at 80 °C. Taken from Ref. [31].

electrons (or holes) can be described with the ionisation rate α by

$$\mathrm{d}N = \alpha\, N\, \mathrm{d}x. \tag{2.10}$$

Further information on charge multiplication can be found in Ref. [16], and a detailed study on charge multiplication in irradiated silicon pad sensors can be found in Ref. [29].

2.3 Radiation damage

Particles traversing a silicon sensor may interact with the material leading to ionising or non-ionising energy deposition. In both cases damage to the silicon sensor is possible. One distinguishes between surface damage and bulk damage.

2.3.1 Surface damage

Ionising energy loss in the surface layers of silicon sensors leads mainly to positive oxide charges close to the Si-SiO_2 interface [30, 31]. If *eh* pairs are generated in the SiO_2 layer they either recombine or separate, e.g. due to diffusion. Due to the higher mobility of electrons compared to holes, electrons move away much faster and a positive oxide charge remains. Consequently the electric field distribution close to the sensor is changed, an electron accumulation layer builds up and inter-strip isolation degrades. Additionally interface traps are introduced at the Si-SiO_2 interface and the generation of current at the interface increases.

The radiation-induced oxide-charge density and interface-state density as a function of dose is similar for different particle types if ionising energy loss dominates. For high doses a

saturation may be observed. An example for the dose dependence of oxide charge density and radiation-induced interface states is given in Figure 2.5.

2.3.2 Bulk damage

Particles crossing a silicon sensor may cause crystal defects by non-ionising energy loss (NIEL) [32]. If the generated defects are electrically active they influence the sensor performance. Int the following sections different consequences are discussed.

Full-depletion voltage and type inversion

If generated defects are donor- or acceptor-like the effective doping concentration N_{eff} is changed, which is the difference of donor and acceptor concentration:

$$N_{eff} = N_d - N_a \qquad [17]. \tag{2.11}$$

The doping concentration is also influenced by donor or acceptor removal, i.e. the deactivation of doping atoms. Changes in N_{eff} will influence the full-depletion voltage V_{fd}, which is proportional to the doping concentration in pad sensors as seen in Equation (2.4). Only those charge carriers which are generated in the depleted volume contribute to the signal. If the applied bias voltage is not sufficient to fully deplete the sensor ($V < V_{fd}$), the charge-collection efficiency may be smaller than 1 if some charge carriers are generated in the non-depleted region.

If the sign of N_{eff} changes due to irradiation-induced defects, the sensor is considered to be type inverted. The effect is also called space charge sign inversion. However, in highly irradiated silicon sensors the space charge distribution is position dependent and is not described by a single doping concentration. More information on this effect, including simulations of the electric field, can be found in Refs. [33, 34].

High irradiation-induced doping concentrations can also lead to locally high electric fields and hence to charge multiplication and to charge-collection efficiencies greater than 1 [29].

Trapping

Radiation-induced defects also can act as trapping centres: they can capture free charge carriers (trapping) and re-emit them later (detrapping). If the detrapping time constant is large with respect to the integration time, the trapped charges do not contribute to the induced signal after being trapped. In the case of planar pad sensors this effect leads to a reduction in charge-collection efficiency (CCE).

Trapping can be described as a loss of free electrons N_e and free holes N_h as following

$$\mathrm{d}N_{e,h} = -N_{e,h} \sum_i \sigma_i^{e,h} \cdot T_i^{e,h} \, \mathrm{d}x, \tag{2.12}$$

where the index i runs over all trapping defects, $T_i^{e,h}$ is the concentration of unfilled trapping centres for electrons (e) and holes (h), with the trapping cross-section $\sigma_i^{e,h}$.

If the thermal velocity is large compared to the drift velocity, the instantaneous velocity v of the charge carriers may be considered to be field independent. If further, the cross sections and the number of filled trapping defects is considered to be uniform in the silicon and independent of the electric field or current densities, then trapping may be also described by

$$\mathrm{d}N_{e,h} = -\frac{1}{\tau_{eff}^{e,h}}\mathrm{d}t, \tag{2.13}$$

with the effective trapping time, τ_{eff}, a single constant. If any of the assumptions is not true the same description is possible, but τ_{eff} may vary with the electric field or with the occupation of traps, which depends on the local electric field, the temperature and the electron- and hole-current densities. Investigations of charge collection in pad sensors made from epitaxial silicon and irradiated with fluences $> 10^{15}$ cm^{-2} show, that the CCE cannot be described with an overall constant trapping time [14, 19]. Instead voltage or field dependent trapping times may be assumed.

Sensor current and NIEL scaling

Radiation-induced defects close to the middle of the band gap may act as current-generation centres, and the sensor current increases with irradiation. Often the irradiation-induced current generation is assumed to be independent of the particle type and the particle energy causing the crystal defects, if particle fluences with the same non-ionising energy loss (NIEL) are compared. Typically particle fluences are scaled to the equivalent fluence of 1 MeV neutrons (neq) which cause the same NIEL [17, 35].

However, the probabilities that different defects are produced depends on the type of irradiation: for neutron irradiation a high number of cluster defects is seen, while for irradiation with charged hadrons there are more point defects, especially at low energies in the order of 10 MeV [94].

Defect kinetics and annealing

Due to the high mobility of vacancies and silicon interstitials and their kinetics, which are produced by NIEL, sensor properties may change in time. Approximately 60 % of the created vacancy-interstitial pairs recombine, in cluster regions even up to ∼95 %. Vacancies and interstitials which do not recombine may form new defects, typically with lower mobility.

To accelerate the defect kinetics the sensors may be heated up, e.g. to 60 °C. A decrease of current generation with annealing time is observed [17]. The effective doping concentration N_{eff} first increases, which corresponds to a reduction of acceptors (Figure 2.6). For p-type silicon and type inverted n-type silicon this corresponds to a reduction of the full-depletion voltage with annealing time, and the effect is usually called beneficial annealing. After

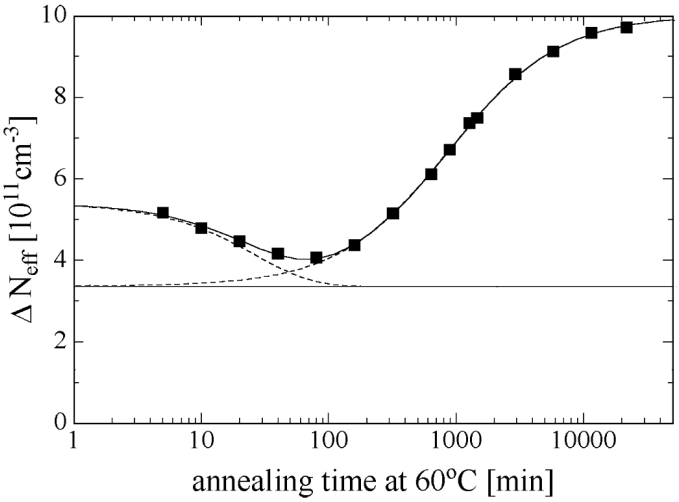

Figure 2.6: An example of the radiation-induced change in N_{eff} as a function of annealing time at 60° C after neutron irradiation with a fluence $1.4 \cdot 10^{13}$ cm^{-2}. Taken from Ref. [17] and simplified.

$\gtrsim$ 80 min annealing time at 60 °C reverse annealing is observed, corresponding to a generation of acceptors. More details on defect kinetics can be found in Ref. [17].

2.4 Growing of silicon crystals

There are three main growing techniques for silicon crystals: Czochralski (Cz), float zone (FZ) and epitaxial (EPI) [14, 17].

Czochralski For Czochralski silicon a monocrystalline seed crystal is placed on the surface of a silicon melt. The crystal is slowly drawn upwards while the melt is rotated. In order to stabilise the melt magnetic fields may be used, leading to the name magnetic Czochralski (MCz). At the melt-crystal interface the melt solidifies with the same crystal orientation as the seed. A high amount of impurities characterises the Czochralski silicon and oxygen concentrations are typically a few 10^{17} cm^{-3}.

Float zone For float-zone silicon again a monocrystalline seed is needed. It is brought in contact with polycrystalline silicon and the region around the contact is melted with a radio-frequency field. The melted region is called the floating zone. The floating zone is shifted so that the monocrystalline seed grows. Compared to Czochralski silicon fewer impurities occur and the oxygen concentration is typically in the range of a few 10^{16} cm^{-3}. However, there is also float-zone silicon with higher oxygen concentrations.

Epitaxial For epitaxially-grown silicon, wafers cut from a single-crystal substrate with high doping concentration are used. On this inactive wafers a thin epitaxial layer with a

low doping concentration is grown, which adopts the crystal orientation of the substrate. Thus the epitaxial layer is monocrystalline. The growing of the epitaxial layer usually takes about 1 min/µm. The thickest epitaxial layers available so far have a thickness of 150 µm. Depending on the substrate, the active thickness and the processing epitaxial layers may have oxygen concentration between 10^{16} cm^{-3} and a few 10^{17} cm^{-3} [14].

Thin active layers In order to have sensors with a thin active volume either the volume is grown epitaxially, or handling wafers with a high doping concentration are used for mechanical stability. As an alternative thicker silicon wafers can be produced and a part of the volume is deactivated by the introduction of a high doping concentration. The introduction of high doping concentrations can be achieved by diffusion at high temperature above 1000 °C and is usually called deep diffusion. By this process also the oxygen content is increased.

Chapter 3

Experimental methods

In this chapter information is given on capacitance and current measurements, as well as on the different setups used for charge-collection measurements. The chapter is based on my diploma thesis [19].

3.1 Capacitance and current measurements

Capacitance and current measurements are performed on pad sensors, in order to extract different quantities like the full-depletion voltage V_{fd}, the sensor thickness d, the effective doping concentration N_{eff}, and the volume normalised current I/V. In strip sensors the strip currents, the inter-strip currents, and the inter-strip capacitances are measured.

A Keithley Kei6517 (max. 1 000 V, 1 mA) is used as both bias source and current meter. All measurements are performed with the high voltage applied to the rear side: positive voltages for p-on-n sensors and negative voltages for n-on-p sensors. The guard ring (for strip sensors the charge-collection ring) is connected to ground and measurements are performed in the dark to avoid photo currents.

In this work an emphasis is laid on charge-collection measurements. For pad sensors presented in Chapter 5, capacitance and current measurements will be presented and discussed in Ref. [36]. However, since some of the charge-collection measurements are compared to the full-depletion voltage (V_{fd}) extracted from capacitance measurements, the determination of V_{fd} will be summarised briefly.

3.1.1 Determination of the full-depletion voltage from the capacitance measurement

The capacitance between pad and back side is determined in parallel mode using either a Hewlett Packard HP4263 or an Agilent capacitance bridge. For irradiated diodes the measured capacitance depends on frequency and temperature. V_{fd} is determined at a temperature of -20 °C using an AC amplitude of 0.5 V at a frequency of 455 Hz. The capacitance is plotted as C^{-2} as a function of voltage and two linear fits are performed, one in the region of highest

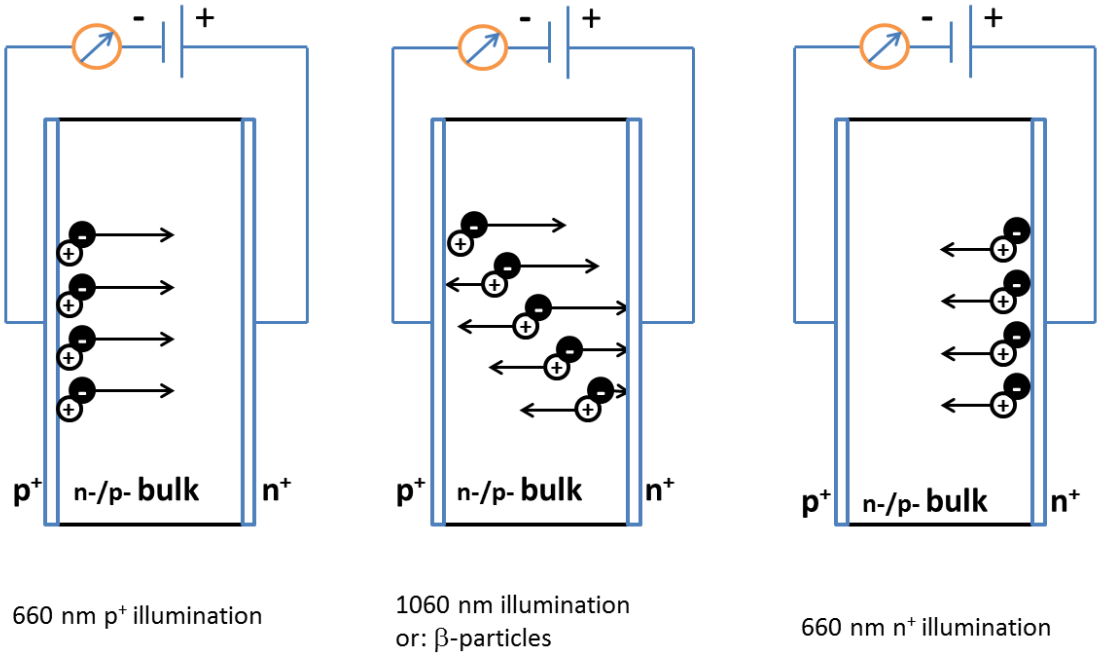

Figure 3.1: Generation and movement of free charge carriers for different illumination modes.

slope and one in the linear region at high bias voltages. The intersection point of the two fitted curves defines V_{fd}.

3.2 Charge-collection measurements

Charge-collection measurements are performed with sensors in reverse bias using three different setups. For time resolved measurements the transient current technique (TCT) is used in two different setups. Free charge carriers are generated using sub-ns pulsed laser light of different wavelengths. The free charge carriers drift in the electric field and induce current in the read-out electrodes. After amplification the currents are read out using a high-bandwidth digital oscilloscope, which is triggered externally by the laser controller.

Laser light of different wavelength is used to study the movement of charge carriers generated at different positions in the silicon sensor. The different positions of charge generation and the resulting charge carrier collection is illustrated in Figure 3.1.

If red laser light with a wavelength of 660 nm or 670 nm is used, the *eh* pairs are generated close to the sensor surface. Light of this wavelength has an absorption length in silicon of about 3.5 µm at room temperature [37]. If no deep implant and no handling wafer is used, both are possible, front-side and rear-side illumination. For pad sensor measurements and charge generation close to the surface, one charge carrier type is collected fast compared to the time resolution of ∼600 ps, and the signals induced on the electrodes are small. The measured signal is dominated by the other charge carrier type, drifting through the entire

sensor. For strip sensors and illumination between the strips, both the collection of holes and the collection of electrons is relevant.

For infrared laser light with a wavelength of ∼1063 nm, *eh* pairs are generated along the whole sensor depth [18, 37] and both electrons and holes contribute to the induced current.

Additionally to the two TCT setups, with which most measurements are performed, a third setup is used. In this setup electrons of a ^{90}Sr source are used to generate charges along the whole sensor depth. The charge-collection efficiency (CCE) is determined to cross-check CCE measurements made with the TCT setup.

The three setups are discussed in more detail in the following.

3.2.1 TCT setup for pad sensors

For measuring pad sensors with the transient current technique a TCT setup was built in 2009. Both the laser driver and the two laser heads are manufactured by Advanced Laser Diode Systems [38]. A red laser head with 670 nm wavelength and a pulse width of 30 ps (FWHM), and an infrared laser head with 1063 nm wavelength and a pulse width of 50 ps (FWHM) are available. Peltier cooling is used to stabilise the chuck at temperatures down to below -30 °C. In this work only temperatures of -20 °C and 0 °C are used.

The pad sensor is fixed with vacuum on a gold-plated metal chuck to provide the rear-side contact. The pad on the front side is biased using a needle, the guard ring is kept floating. The signal is brought via a 2 m cable to a Picosecond Pulse Lab 5531 bias-T followed by a Phillips-Scientific current amplifier, before it is digitised using a Tektronix DPO 4104 oscilloscope with 1 GHz bandwidth. For the sensors investigated in this work rise times of ∼600 ps are achieved.

The laser is operated with a repetition rate of 200 Hz and the time resolved current signal $I(t)$ is recorded as an average of 512 samples. The collected charge Q is determined by offline integration over an interval of 30 ns. The CCE is determined from the ratio of collected charge Q to generated charge Q_0. To determine Q_0, full charge collection is assumed in fully depleted non-irradiated pad sensors and Q_0 is determined at 400 V in a non-irradiated reference sensor of the same type as the sensor under test. The CCE is then given by

$$CCE = \frac{Q}{Q_0} = \frac{Q}{Q^{400\mathrm{V}}_{non-irradiated}}. \tag{3.1}$$

Both sensors, the sensor under test and the non-irradiated reference sensor, are measured on the same day and under the same measurement conditions. The accuracy of the normalisation is discussed in Section 3.2.4.

3.2.2 Multi-channel TCT setup for strip and pad sensors

To study the charge collection in strip sensors and to perform position scans on pad sensors a multi-channel TCT setup is used [18]. Four different laser heads are available to generate

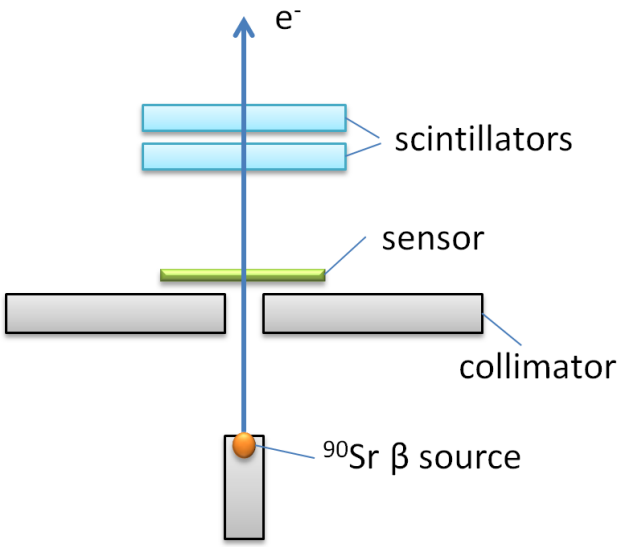

Figure 3.2: Working principle of the β setup, reproduced from Ref. [40].

sub-ns pulses of different wavelengths: 660 nm, 830 nm, 1015 nm and 1052 nm. Both the laser heads and the SepiaII laser driver are manufactured by Picoquant [39]. An optical system makes it possible to focus the light down to 3 µm rms. The beam position is controlled mechanically in the x, y and z direction with a precision of 0.1 µm.

The front side contact between the sensor and the sample holder is provided by wire bonding, the rear side contact through silver glue. Needles are used to contact the sample holder. After a ∼2 m signal cable, Agilent 8496G attenuators are used to provide a high dynamic range. Femto HSA-X-2-40 current amplifiers with a rise time of 180 ps are used before the signal is digitised in a Tektronix DPO 7254 oscilloscope with 2.5 GHz bandwidth. The high voltage is applied to the rear side and is decoupled from the amplifier by a bias-T. The temperature is logged using a PT100 temperature sensor close to the sample holder. 5 000 samples are averaged and recorded as time resolved signals for up to four channels in parallel. For strip-sensor measurements presented in this work two strips and the rear-side contact are read out. The induced charge is determined by off-line integration.

3.2.3 β setup for pad sensors

The working principle of the β setup is shown in Figure 3.2. An electron from a ^{90}Sr β source traverses the silicon sensor and reaches the scintillators. The event will be triggered if the electron has enough energy to reach the second scintillator. The signals are recorded using a charge-sensitive amplifier and the signal distribution is fitted by a convolution of a Landau curve with a Gauss function. The most probable value (mpv) of the Landau is taken as signal. The setup is calibrated using both internal charge injection and the 60 keV γ line of a ^{241}Am source. The calibration uncertainty is ∼0.5 % at 16 ke, and the non-linearity is ∼1 %. The pedestal uncertainty is ∼100 e. More details on the setup can be found in Ref. [40].

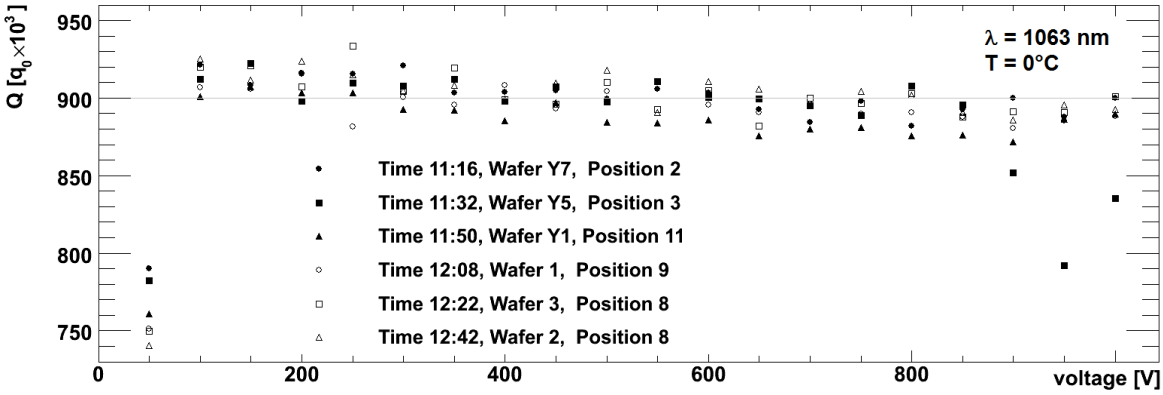

Figure 3.3: Spread and voltage dependence of the integrated signals for six non-irradiated sensors. Results of six measurements are shown using non-irradiated 200 µm thick p-type MCz sensors from six different wafers and five different positions on the wafer. The pad sensors from three of the wafers have a p-spray isolation (Y) between the n^+ pad implant and the n^+ guard-ring implant.

3.2.4 Uncertainty of the charge-collection efficiency

In order to estimate uncertainties on the determined CCE, the stability of the TCT setup for pad sensor measurements is investigated. The used laser heads are found to give stable light output after ∼3 hours of operation within ∼1 % fluctuation within one day [19]. However, to determine the CCE of an irradiated sensor two measurements are necessary: additionally to the irradiated sensor a non-irradiated sensor of the same production run is measured as a reference. Both measurements are performed on the same day with as little time difference as possible, typically ∼1 hour. The reference sensor is taken from a different position on the same wafer or from a different wafer as the irradiated sensor.

To estimate the uncertainty of this procedure, including the positioning and the contacting of the sensors, six non-irradiated sensors of the same production run are measured on the same day. For this test infrared laser light is used and the integrated signals as a function of bias voltage are shown in Figure 3.3. The collected charge at a fixed voltage above full depletion is observed to show a spread of ∼2 %. Additionally to this fluctuation, less collected charge is observed at higher bias voltage above full depletion. This effect may be explained by more signal losses in the electronic circuit for shorter pulses. Compared to the signals at 400 V a drop of ∼2 % is observed at 1 000 V.

For the determination of $CCE = Q/Q_0$, the collected charge for a non-irradiated sensor at 400 V bias voltage, $Q_0^{400\,\mathrm{V}}$, is used. Since both the measurement of Q and the measurement of $Q_0^{400\,\mathrm{V}}$ have a statistic uncertainty of ∼1 % and an additional systematic uncertainty by the response of the electronic circuit is given by up to ∼2 %, the total uncertainty on the CCE is estimated to be ∼3 %.

	β setup	TCT setup
charge generation	electrons	infrared 1063 nm light
generated charge (1/200 µ)	~14 000 eh pairs	~1 000 000 eh pairs
trigger	two scintillator coincidence	laser driver
determination of Q	MPV of Gauss-Landau	512 averages of $I(t)$, $Q = \int I \, \mathrm{d}t$
determination of CCE	$CCE = Q/Q_0$	$CCE = Q/Q_0$

Table 3.1: Comparison of the features of the β setup and the TCT setup for pad sensors.

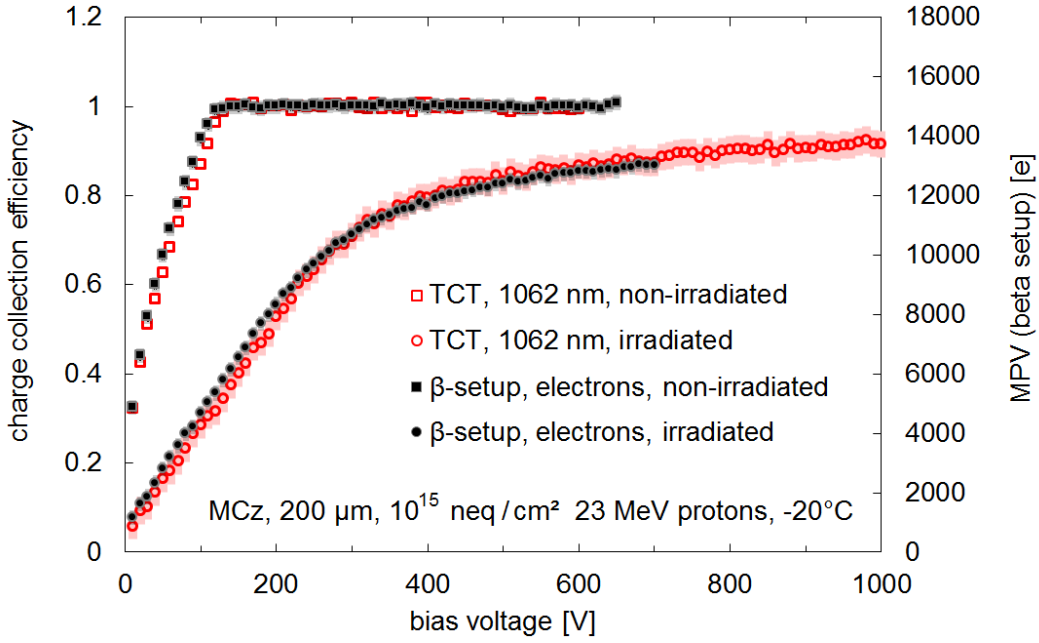

Figure 3.4: Comparison of the CCE determined with two different test setups. 200 µm thick MCz n-type pad sensors are measured at a temperature of -20 °C before and after irradiation with 10^{15} neq/cm^2 23 MeV protons.

Cross-check with different setups

To crosscheck the CCE, which is determined in the TCT setup for pad sensors, additional checks are made. As an alternative readout the current amplifiers and the digital oscilloscope are replaced by a charge integrating amplifier using otherwise the same setup. Results are presented in [19] and agree within the 3 % uncertainty.

As a further test the CCE of an irradiated pad sensor is determined in both the TCT setup for pad sensors and the β setup. Both setups are described above in this section and an overview over the differences between the TCT setup and the β setup is given in Table 3.1. In both setups the CCE is determined by normalising the signal of the irradiated sensor to the signal of the non-irradiated sensor. A comparison of the CCE determined in both setups is shown in Figure 3.4. The results agree within the 3 % uncertainty. Higher charge values for the β setup at low voltages may be explained by a longer integration time: a shaping time of 100 ns is used for the β setup and an offline integration time of 30 ns for the TCT setup.

Chapter 4

Electric-field studies at the Si-SiO_2 interface of p^+n strip sensors using interface charge losses

4.1 Overview

In this chapter charge losses at the Si-SiO_2 interface of p^+n silicon strip sensors, and their relation to the electric field, the surface potential and to the accumulation layer will be discussed. It contains three publications [41, 42, 43], of which I am first and corresponding author, as well as unpublished material.

Introduction to charge losses at the Si-SiO_2 interface and a comparison to simulated electrostatic potentials

Section 4.2 contains an introduction to charge carrier losses at the Si-SiO_2 interface. Incomplete charge collection is observed using the transient current technique (TCT) with focussed and sub-ns pulsed laser light of 660 nm wavelength. Light of this wavelength only penetrates $\sim$3.5 µm into the silicon and generates *eh* pairs close to the Si-SiO_2 interface. The charge losses are described as a function of the light-spot position for strip read out and for the rear-side read out, using a model calculation. Time-resolved current signals confirm the observed charge losses.

Charge carrier losses at the Si-SiO_2 interface are discussed for sensors before and after irradiation with 12 keV x-rays to a dose of 1 MGy in the SiO_2, and as a function of humidity and biasing history. Depending on the biasing history and on the irradiation, both incomplete collection of electrons and incomplete collection of holes is observed.

The observed charge losses are compared to the electrostatic potential which is obtained from device simulations. Different boundary conditions at the surface of the passivation layer are used, in order to simulate different humidities and biasing histories. It is shown that

for the non-irradiated sensor the simulated potentials qualitatively agree with the observed interface charge losses:

- if electron losses are observed, the simulated electric field points out of the oxide,
- if no losses are observed, the simulated electric field points in the direction of the read-out strips,
- if hole losses are observed, the simulated electric field points into the oxide.

For the irradiated sensor charge losses are also observed to depend on the biasing history and both situations with electron losses and situations without charge losses occur. However, if a fixed interface charge density of 10^{12} cm^{-2} is assumed, in each case the simulated electrostatic potential is very similar and the electric field points out of the oxide independently of biasing history.

Section 4.2 is published [41] in the journal Nuclear Instruments and Methods in Physics Research Section A. The title of the publication is *Charge losses in segmented silicon sensors at the Si-SiO$_2$ interface*. Several authors contributed to the work and comments by the reviewers in the peer-review process have been taken into account.

Additional material complementing Section 4.2 is added in Section 4.5:

- In Section 4.2 a model calculation is used to describe the integrated signals as a function of position of charge carrier generation, but no comparison between the model calculated signals and the data is made. The graphical comparison is given in Section 4.5.1 and shows that the measured signals are well described by the model calculation.
- In Section 4.2 only results for a DC-coupled sensor with crystal orientation <111> produced by Hamamatsu [44] are shown. Additional measurements and fit results for an AC-coupled sensor with crystal orientation <100> produced by CiS [45] are presented in Section 4.5.1. The results for both producers are similar and show that the observed effects are valid for more than one sensor technology.
- In Section 4.2 losses of charge carriers generated very close to the surface using 660 nm light are studied. An additional measurement using laser light with a wavelength of 830 nm is added in Section 4.5.2. 830 nm light penetrates further into the silicon ($\sim$13 µm at room temperature, compared to $\sim$3.5 µm for 660 nm light) and information on the electric field in the region of a few µm below the interface is gained. The position of the saddle point of the electrostatic potential is extracted and is found to be compatible with device simulations.

Time development of the electric field close to the Si-SiO$_2$ interface

In Section 4.3 the time development of the electric field close to the Si-SiO$_2$ interface is studied using interface charge losses. After the bias voltage is changed charge losses are

observed to be time dependent. In dry conditions it takes between six hours and several days until a steady state is reached. In humid conditions time constants are about two orders of magnitude shorter. For the non-irradiated sensor the time development of charge losses is explained by a change in surface potential due to charge transport at the sensor surface. For the irradiated sensor, with an interface trap density of $\sim 1.6 \cdot 10^{12}$ cm^{-2}, the case is found to be more complicated and additional effects are relevant.

Section 4.3 is published [42] in the journal Nuclear Instruments and Methods in Physics Research Section A. The title of the publication is *Time dependence of charge losses at the Si-SiO$_2$ interface in p$^+$n-silicon strip sensors*. Several authors contributed to the work and comments by the reviewers in the peer-review process have been taken into account.

In Section 4.3 it is distinguished between measurements in humid atmosphere with a humidity of > 60 % and measurements in dry atmosphere with a humidity of < 1 %. In Section 4.5.3 more information is given for the non-irradiated sensor. Time constants for different humidities (< 1 %, $\sim$40 %, $\sim$70 % and $\sim$85 %) are compared. It is observed that time constants depend strongly on humidity, and that their humidity dependences after a bias voltage increase (from 0 V to 200 V) and after a bias voltage decrease (from 500 V to 200 V) are similar. Further, the interpretation of surface charge transport is supported by a comparison to the humidity dependence of the sheet resistance.

Study of the accumulation layer using interface charge losses

In Section 4.4 the accumulation layer is studied using charge-carrier deposition close to the Si-SiO$_2$ interface. It is tested how much charge can be locally added to the accumulation layer, and how much time is required for the accumulation layer to return to steady state after charge deposition. The charge is generated using a 660 nm laser operated in burst mode with 30 pulses per burst. Insight is gained on how much charge is needed to significantly change the local electric field and on the time constants relevant for charge transport out of the accumulation layer.

Section 4.4 is published [43] on the electronic archive and distribution server arXiv and accepted for publication to the journal Nuclear Instruments and Methods in Physics Research Section A. The title of the submission is *Study of the accumulation layer and charge losses at the Si-SiO$_2$ interface in p$^+$n-silicon strip sensors*. Several authors contributed to the work and comments by the reviewers in the peer-review process have been taken into account.

Contributions to the work presented in this chapter

Several authors contributed to the work which is presented in Sections 4.2 – 4.4, and which is published elsewhere [41, 42, 43]. The charge collection measurements presented in this chapter and their evaluation using model calculations are performed by me. They are the central part of the experimental study. Further, strip current measurements for different humidities and biasing histories are performed by me. The device simulations, which are essential for

the discussion of the obtained results, are performed by Joern Schwandt [11], and x-ray irradiations as well as measurements on gate-controlled diodes by Jiaguo Zhang [46]. The text of the three publications is edited by both Robert Klanner and me. All authors contributed with different ideas, comments and suggestions. Also the comments by the reviewers in the peer-review processes have been taken into account.

4.2 Introduction to charge losses at the Si-SiO_2 interface and a comparison to simulated electrostatic potentials

This section is published in the journal Nuclear Instruments and Methods in Physics Research A with the title *Charge losses in segmented silicon sensors at the Si-SiO_2 interface* [41].

Abstract

Using multi-channel time-resolved current measurements (multi-TCT), the charge collection of p^+n silicon strip sensors for electron-hole pairs produced close to the Si-SiO_2 interface by a focussed sub-nanosecond laser with a wavelength of 660 nm has been studied. Sensors before and after irradiation with 1 MGy of X-rays have been investigated. The charge signals induced in the readout strips and the rear electrode as a function of the position of the light spot are described by a model which allows a quantitative determination of the charge losses and of the widths of the electron-accumulation and hole-inversion layers close to the Si-SiO_2 interface. Depending on the applied bias voltage, biasing history and environmental conditions, like humidity, incomplete electron or hole collection and different widths of the accumulation layers are observed. In addition, the results depend on the time after biasing the sensor, with time constants which can be as long as days. The observations are qualitatively explained with the help of detailed sensor simulations. Finally, their relevance for the detection of X-ray photons and charged particles, and for the stable operation of segmented p^+n silicon sensors is discussed.

4.2.1 Introduction

In the last 30 years segmented silicon sensors underwent an impressive development and found many applications. Examples are precision tracking in particle physics, imaging in photon science and many applications in industry and medicine. These sensors rely on a high quality SiO_2 layer grown on the silicon [47, 48] to separate the finely segmented electrodes fabricated by doping the silicon. It is well known [30] that the positive charges, which are always present in the SiO_2, induce an electron-accumulation layer at the interface between the SiO_2 and n-type silicon, and that ionizing radiation, like X-rays or charged particles passing through the SiO_2, further increases the density of positive oxide charges and produces traps at the Si-SiO_2 interface.

For sensors with p^+ electrodes fabricated on high-ohmic n-type silicon, which are investigated in this work, potential consequences of the accumulation layer are:

- an increase of the capacitance between the p^+ electrodes,
- a decrease of the resistance between the p^+ electrodes,
- an increase of the depletion voltage of the sensor,

- an increase of the electric field near the p^+ implants, possibly causing charge-carrier multiplication or breakdown,
- charge losses at the Si-SiO$_2$ interface, and
- an increase of charge-collection times which may result in a ballistic deficit or pile-up.

The accumulation layer is also sensitive to charges on the surface of the passivation layer. They influence the electric boundary condition [49, 50] which have to be known for the mathematical modeling. The density of charges close to the interface depends on many parameters, like the biasing history, the quality of the oxide, the properties of the passivation layer, the cleanliness of surfaces and the humidity of the environment. The time scale to reach stable conditions can be as long as days, with a corresponding time dependence of sensor performance.

In this work the time resolved pulses produced by a sub-nanosecond laser focussed to an rms of 3 µm in two different p^+n strip sensors are measured as a function of the position of the light spot. The wavelength of the light is 660 nm, which corresponds to an absorption length in silicon of 3.5 µm at room temperature. The strip sensors investigated have a pitch of 50 and 80 µm, respectively. The measurements are made before and after irradiating the sensors with 12 keV X-rays to 1 MGy (SiO$_2$). Similar measurements are discussed in Refs. [51, 52].

Above measurements are performed at different voltages and for different humidities. It is found that the measured current transients and the fraction of the generated charges collected are different for irradiated and non-irradiated sensors. They also depend on the biasing history and change with time, with time constants which depend on humidity. The measurements can be described quantitatively by losses of electrons and/or holes in the region close to the Si-SiO$_2$ interface. The results provide insight into the influence of X-ray radiation damage, biasing history and humidity on the accumulation layer, as well as on the local electric fields close to the Si-SiO$_2$ interface of segmented silicon sensors.

The paper first describes the sensors investigated and the measurement techniques used. A qualitative discussion of the integrated charge expected as a function of the position of the generated *eh*-pairs with and without charge losses follows, and a simple model is developed. Next, the expectations are compared to selected measurements which demonstrate situations of electron losses, hole losses and no losses. Then the model is fitted to the data and parameters like the numbers of electrons and holes collected and the width of the accumulation layer are determined. It is observed that the measured parameters change with time, with a time constant that depends on humidity. Finally, an interpretation of the results is presented and their relevance for the understanding and use of sensors discussed.

The work has been done within the AGIPD collaboration [6, 7] which is developing a large area pixel detector system for experimentation at the European X-ray Free-Electron Laser XFEL [1, 2] and other X-ray sources.

4.2.2 Measurement techniques and analysis

Sensors under investigation

Two different p^+n strip sensors have been investigated: A DC-coupled sensor produced by Hamamatsu [44], and an AC-coupled sensor produced by CiS [45]. Sensors from two vendors have been studied to get an idea how much the observed effects depend on technology. Overall, the results found are similar. Finally we concentrated on the DC-coupled sensor because AGIPD [6, 7] will use a DC-coupled sensor, and detailed TCAD[1] simulations of AC-coupled sensors are significantly more complex. The relevant parameters for both sensors are listed in Table 4.1. All measurements presented in this work refer to the Hamamatsu sensor whose cross-section is shown in Figure 4.1. The sensors are covered by a passivation layer with openings at the two ends of each strip for bonding. Both sensors were investigated as produced, and after irradiation with 12 keV photons to 1 MGy (SiO_2) followed by annealing for 60 minutes at 80 °C. The corresponding values for oxide charge density, N_{ox}, integrated interface trap density, N_{it}, and surface current density, I_{surf}, shown in Table 4.2 have been derived from measurements on MOS capacitors and gate-controlled diodes from Hamamatsu [31, 53, 54, 46] and scaled to the measurement conditions of the sensor.

[1] TCAD = technology computer aided design

producer	Hamamatsu	CiS
coupling	DC	AC
pitch	50 µm	80 µm
depletion voltage	∼155 V	∼63 V
doping concentration	$\sim 10^{12}$ cm^{-3}	$\sim 8 \cdot 10^{11}$ cm^{-3}
single strip capacitance	∼1.4 pF	∼0.5 pF
rear side capacitance	∼12 pF	∼24 pF
gap between p^+ implants	39 µm	60 µm
width p^+ implant window	11 µm	20 µm
depth p^+ implant	unknown	1.2 µm
aluminium overhang	2 µm	-2 µm
number of strips	128	98
strip length	7.956 mm	7.8 mm
sensor thickness	450 µm	285 µm
thickness SiO_2	700 nm	300 nm
thickness Si_3N_4	none	50 nm
passivation layer	unknown	unknown
crystal orientation	⟨111⟩	⟨100⟩

Table 4.1: Parameters of the Hamamatsu sensor and of the CiS sensor. For the simulations of the Hamamatsu sensor a Gaussian p^+ implantation with a maximum density of $1.7 \cdot 10^{19}$ cm^{-3} and a junction depth of 1.5 µm has been assumed. For the passivation layer we assume Si-SiO_2 with a thickness of 700 nm.

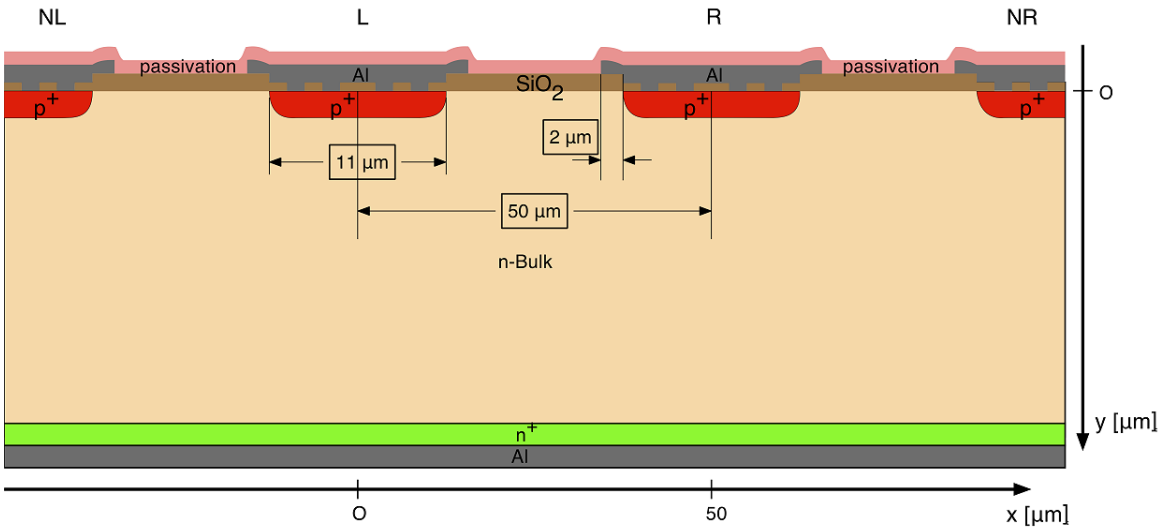

Figure 4.1: Schematic cross section of the DC-coupled p^+n sensor, and definition of the x and y coordinates. The drawing is not to scale.

X-ray dose	0 Gy	1 MGy (60 min. at 80°C)
N_{ox}	$1.3{\cdot}10^{11}$/cm^2	$1.4{\cdot}10^{12}$/cm^2
N_{it}	$0.87{\cdot}10^{10}$/cm^2	$1.6{\cdot}10^{12}$/cm^2
I_{surf}	9.8 nA/cm^2	2.2 µA/cm^2

Table 4.2: Oxide charge density, N_{ox}, interface trap density integrated over the Si-band gap, N_{it}, and surface current density, I_{surf}, obtained from measurements on test structures (a MOS capacitor and a gate-controlled diode) produced by Hamamatsu. The values for a temperature of 22.9 °C before and after X-ray irradiation to 1 MGy and annealing for 60 minutes at 80 °C are presented. The actual measurements were taken at 21.8 °C and, for the irradiated structures after annealing for 10 minutes at 80 °C, and then scaled (scale factor ~ 0.7) to above values, which correspond to the measurement conditions of the sensor investigated.

TCT measurements

To study the charge collection and charge transport in the sensors, the instantaneous currents which are induced in the electrodes by the moving charges are measured (Transient Current Technique - TCT [55, 21, 18]). The multi-channel TCT setup described in detail in Ref. [18] has been used for the measurements. Electron-hole pairs in the sensor close to its surface are generated by red light (660 nm) from a laser focussed to 3 µm, which has an absorption length at room temperature of approximately 3.5 µm. The number of generated eh-pairs is controlled by optical filters. Between 30 000 and few millions of eh-pairs are used for the measurements. The absolute number of eh-pairs produced has been obtained to an accuracy of ~ 5 % from the integrated charge measured for non-irradiated sensors and the known gain of the amplifiers. The bias voltage (up to 500 V) is applied on the n^+-rear side of the sensor. The current signal is read out on the rear side and on two strips on the front side using Agilent 8496G attenuators, Femto HSA-X-2-40 current amplifiers with a rise time of 180 ps (10 to

90 %) and a Tektronix digital oscilloscope with 2.5 GHz bandwidth (DPO 7254). The readout strips are grounded through the DC-coupled amplifiers (∼50 Ω input impedance). The seven strips to right and the seven to the left of the readout strips are connected to ground by 50 Ω resistors.

The collected charge per strip is calculated off-line by integrating the current signal. For most measurements the laser is used with a repetition rate of 1 kHz and the current is integrated over 25 ns. For longer integration times the noise increases and no significant change of the integrated charge is observed.

Naive expectations from simulations and analysis method

In this section 2-D simulations using SYNOPSIS TCAD [56, 11] are presented. They illustrate the distribution of the field and potential in the region of the strips and the Si-SiO$_2$ interface, and are used to calculate the weighting potentials [24, 25, 27], which are required to estimate the expected signals, i.e. the charges induced in the readout strips and the rear electrode, as a function of the position of the injected light.

The simulated electric potential in a strip sensor close to the Si-SiO$_2$ interface between the strip implants depends on the boundary conditions at the SiO$_2$ surface, the oxide charge density, the density of charged interface states and the current distribution in the sensor.

Figure 4.2 shows for Neumann (zero electric field perpendicular to the outer SiO$_2$ surface) and Dirichlet boundary conditions (zero potential at the outer SiO$_2$ surface) the electric potential for the Hamamatsu sensor with the strips at 0 V and the rear contact at 200 V.

Figure 4.3 shows the electron density for the same simulations. The high electron density of several 10^{18} cm^{-3} shows that an accumulation layer with a width of about 35 µm has formed below the Si-SiO$_2$ interface. The dark current is mainly due to the surface generation current from the depleted Si-SiO$_2$ interface. The holes generated at the interface drift to the p^+ strips. The electrons drift along the field lines to the rear contact, as can be seen from the increased electron density at the symmetry plane between the strips for larger y values. Between the readout strips, approximately 6 µm below the Si-SiO$_2$ interface, the potential has a saddle point and the electric field points from the accumulation layer into the sensor. Thus, electrons produced close to the accumulation layer may not reach the rear contact during the integration time of the measurement. Simulations with an oxide charge density of 10^{11} cm^{-2}, which is typical for a non-irradiated sensor, also show an accumulation layer for Neumann boundary conditions. For the Dirichlet boundary conditions however, the accumulation layer is absent. It should be noted that, given the uncertainties on the boundary conditions, the simulations presented only serve as an illustration.

Figure 4.4 shows the weighting potential for strip L (centred at $x = 0$), $\phi_{w,L}$, for the above mentioned simulations of the Hamamatsu strip sensor. Both the two-dimensional distributions, as well as its x dependence for y values of 0.01, 1, 2 and 3 µm below the Si-SiO$_2$ interface are shown. $\phi_{w,L}$ is obtained from the difference of the potential calculated with strip L at 1 V and all other strips at 0 V minus the potential with all strips at 0 V. In both cases the backplane

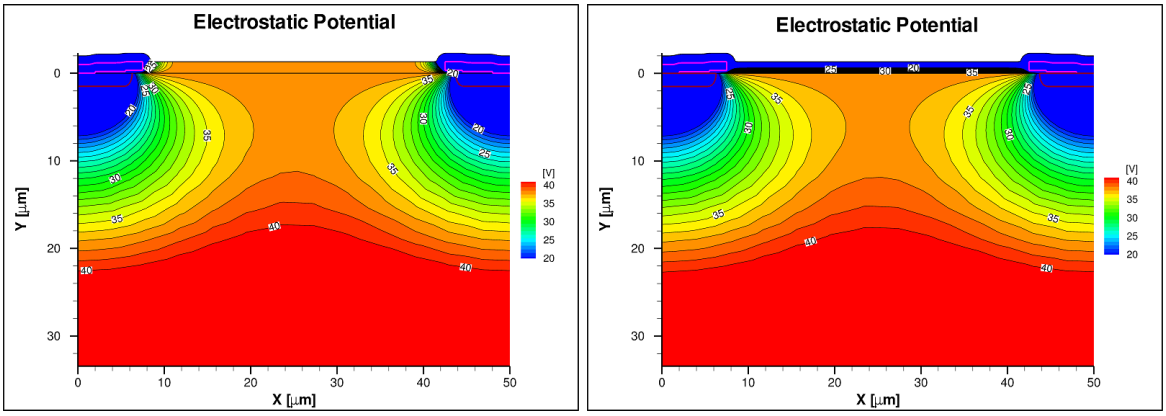

Figure 4.2: Electric potential for the Hamamatsu strip sensor calculated using SYNOPSIS TCAD. Neumann boundary conditions (left) and Dirichlet boundary conditions (right) on the SiO_2 surface, a positive oxide charge density of $2 \cdot 10^{12}$ cm^{-2} and a surface current density of 8 µA/cm^2 are assumed. The bias voltage, applied to the rear contact is 200 V. The sensor has a pitch of 50 µm and a thickness of 450 µm. Only the region 35 µm from the strip surface is shown. The colour scale covers only the range between 20 and 40 V, and the distance between the equipotential lines is 1 V.

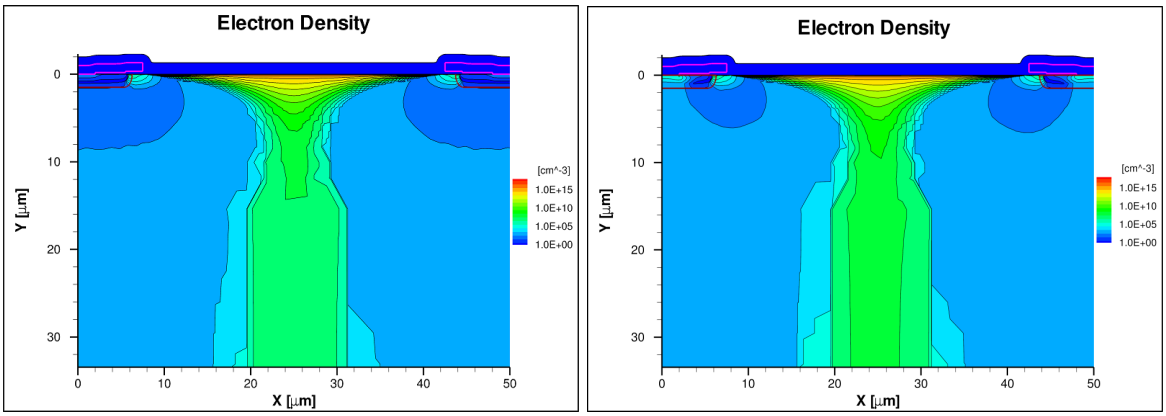

Figure 4.3: Free electron density for the Hamamatsu strip sensor. The conditions for the simulations are the same as for Figure 4.2.

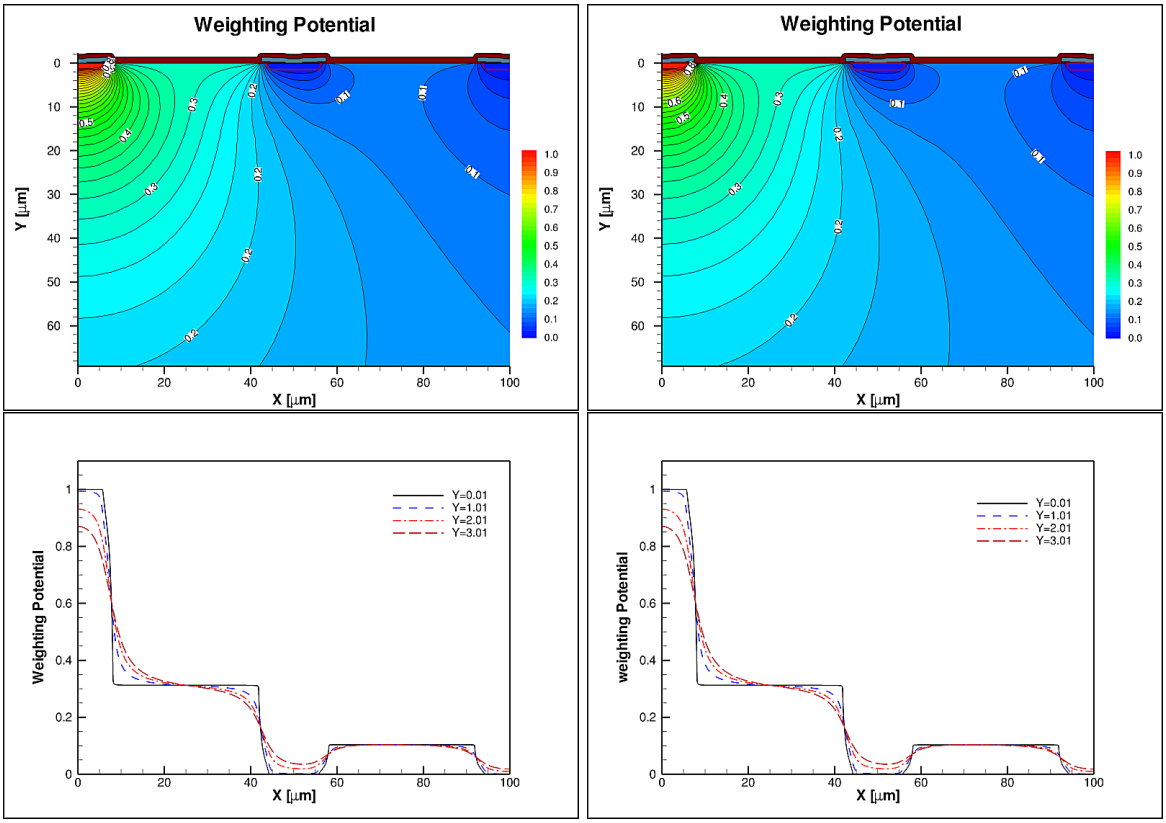

Figure 4.4: Weighting potential for strip L for the Hamamatsu strip sensor. The top row shows the two-dimensional distributions, the bottom row the one-dimensional distributions 0.01, 1.0, 2.0 and 3.0 µm below the Si-SiO$_2$ interface. The parameters for the simulations are the same as for Figure 4.2.

is biased to 200 V. In this way the effects of the mobile charge carriers in the accumulation layer are properly taken into account [27]. One consequence is that $\phi_{w,L}$ is constant over the accumulation layer. We also note that, as expected, the weighting potential is hardly affected by the boundary conditions on the sensor surface.

In order to estimate the charge collected by the individual strips and by the rear contact separately for electrons and holes, the following assumptions for the spot size of the laser beam and for the weighting potential close to the Si-SiO$_2$ interface are made:

- The beam spot is assumed to have a Gaussian distribution with an rms width of 2 µm. The light transmission is assumed to be zero for aluminum and constant for SiO$_2$.
- The holes generated by the laser light, possibly only a fraction of them if hole losses occur, are collected by the closest strip. The electrons not trapped at the interface are collected by the rear electrode. Thus, diffusion effects are neglected.
- The charge Q induced on electrode i by a charge q moving from position x to electrode j is given by $Q_i = q \cdot (\phi_w^i(j) - \phi_w^i(x))$, i.e. the product of the charge q times the difference of the weighting potential at the electrode where the charge q was collected minus the

weighting potential at the position where it was generated. Note, that the sign of the induced signal Q depends on the sign of the charge q. "Lost charges" are assumed to remain at the point where they have been generated, and therefore do not contribute to the signal.

- Inspired by the simulation shown in Figure 4.4, we make following assumptions for the weighting potentials ϕ_w^i. They are shown in Figure 4.5. By definition, ϕ_w^L is 1 at strip L, and 0 for all other strips and for the rear contact. Over the width of the accumulation layer (20 µm in the Figure) ϕ_w^L is assumed to be constant, with a value of 0.35 at the accumulation layers adjacent to L, and 0.05 at the next one. Between the edges of the Al strips and the edges of the accumulation layers weighting potentials linear in x are assumed. The weighting potentials for the other strips considered are obtained by symmetry considerations.

- The weighting potential for the rear contact ϕ_w^{Rear} has a value of 1 at the rear contact, 0.06 at the accumulation layer, 0 at the strips, and a linear dependence in x in-between.

For the situation where all electrons and holes generated are collected, Figure 4.5 shows separately for electrons, holes and for the sum of electrons and holes, the predictions for the charge collected by strips L and R, their sums L + R, the charge collected by the strips beyond the neighbours, NL and NR, the sum of NL + L + R + NR, and the charge collected by the rear contact. A width of 20 µm for the accumulation layer and the weighting potentials presented above, is assumed. The signals are normalised to one eh pair generated and q_0 is the elementary charge. We note, that a hole produced close to the accumulation layer and collected by strip L induces a positive signal in strip L and a negative signal in strip R. For the assumed weighting potential of 0.35 at the accumulation layer the hole signals are $Q_L^h = q_0 \cdot (1 - 0.35) = 0.65 \cdot q_0$ and $Q_R^h = q_0 \cdot (0 - 0.35) = -0.35 \cdot q_0$, respectively. An electron which drifts from the accumulation layer to the rear contact induces a positive signals $Q_L^e = Q_R^e = -q_0 \cdot (0 - 0.35) = 0.35 \cdot q_0$. If for an eh pair the hole is collected by strip L and the electron by the rear contact, the signals are $Q_L = Q_L^e + Q_L^h = q_0$ and $Q_R^e + Q_R^h = 0$. In the two strips NL and NR, positive electron and negative hole signals of $0.05 \cdot q_0$ are induced, which cancel in the sum. In the rear contact a small negative hole signal ($-0.06 \cdot q_0$) and a much larger negative electron signal ($-0.94 \cdot q_0$) are induced, which again add to q_0.

At the centre between the strips, at $x = 25$ µm, the hole signal shows a rapid transition from positive to negative, whereas the electron signal remains constant. As expected for the situation without charge losses and no diffusion, the strip closest to the light spot and the rear contact record the total generated charge. However, current pulses are also induced in non-adjacent strips, as the collection time for the holes, which are produced close to the collecting strip, is much shorter than for the electrons, which drift through the entire detector. The integrals however are zero. In Section 4.2.3 measurements of such current signals will be shown.

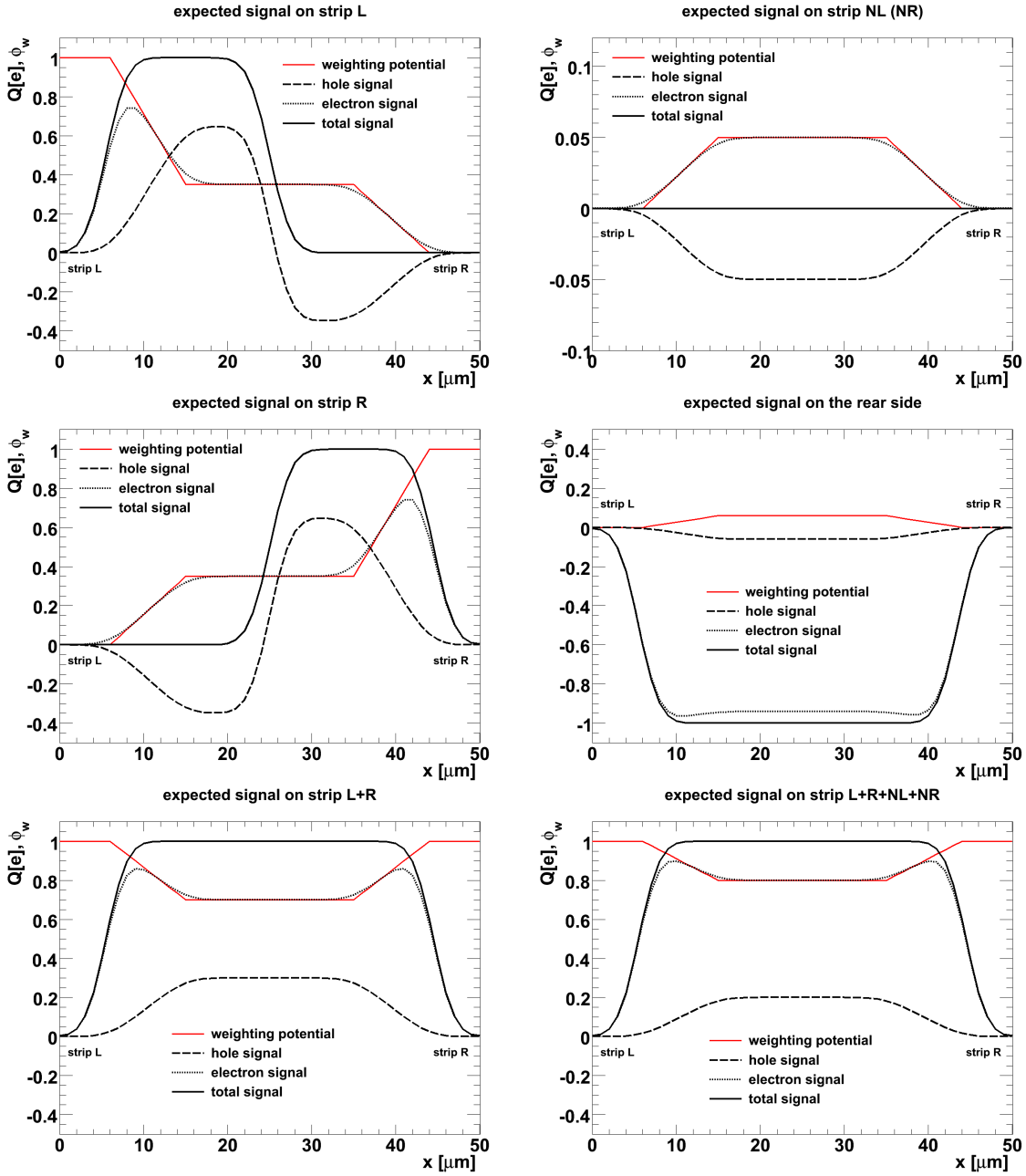

Figure 4.5: Weighting potential and expected integrated hole and electron signals as a function of the position x of the light spot between the strips L and R for the situation of complete charge collection. The signals are normalised to one produced electron-hole pair. A Gaussian light profile with an rms width $\sigma = 2$ μm is used. For more details see text.

Figure 4.6 shows the predicted charge distributions for complete hole collection and 50 % electron losses. Here the fraction of lost electrons is assumed to be independent of the position x of illumination. It is assumed that the electrons are trapped at the x position of the Si-SiO$_2$ interface where they were produced for a time longer than the integration time used in the analysis (25 ns). The weighting potential at this position is used to calculate the charge losses. A reduction of the sum of the electron plus hole signals from the neighbouring strips L and R to about 65 % is predicted. The signal on the rear side is reduced to about 50 %. In addition, negative signals of about 3 % appear at the next to neighbouring strips NL and NR. In a similar way the signals for hole losses can be obtained by multiplying the signals due to the holes in Figure 4.5 with the fraction of holes collected. In this case a positive signal is predicted for strips NL and NR.

When comparing the measurements, which are shown in Chapter 3, to the predictions discussed above, differences are found, and some of the assumptions have to be changed for a quantitative description of the data. We note that these changes have been first derived from the experimental data and later, at least to some extent, explained by the simulations presented in Chapter 4.

The ad-hoc assumption of an x-independent loss of electrons at the Si-SiO$_2$ interface has to be replaced by a loss linear in x between the centre of the gap and the strip edge. Introducing position dependent hole losses, however, does not improve the description of the data, and is therefore not used. Figure 4.7 shows the predicted signal distributions for position dependent electron losses, with losses of 100 % at the Al-strip edge and 0 % at the centre between strips.

In addition we observe in some of the measurements, that even when the light is injected quite some distance from the centre between the strips, a significant number of holes reach the far readout strip. This is taken into account by an additional hole-diffusion term.

Model for determining the charge losses from the data

This section discusses the parameters of the model which is used in Chapter 3 to fit the charges Q_i collected at the electrodes i as a function of the position x of the laser beam. For the laser beam between strips L and R ($0 \leq x \leq 50$ µm) it is assumed that no holes are collected by strip NL nor by strip NR. N_h is the total number of holes collected: $f_L(x) \cdot N_h$ by strip L, and $(1 - f_L(x)) \cdot N_h$ by strip R. The number of electrons collected by the rear contact is N_e. Using the weighting potentials discussed in the previous section, we obtain for the signal charge induced in strips L, NL and in the rear contact:

$$Q_L(x) = N_h(x) \cdot [f_L(x) \cdot (1 - \phi_w^L(x)) + (1 - f_L(x)) \cdot (-\phi_w^L(x))] - N_e(x) \cdot (-\phi_w^L(x))$$

$$Q_{NL}(x) = N_h(x) \cdot (-\phi_w^{NL}(x)) - N_e(x) \cdot (-\phi_w^{NL}(x))$$

$$Q_{rear}(x) = N_h(x) \cdot (-\phi_w^{rear}(x)) - N_e(x) \cdot (-\phi_w^{rear}(x))$$

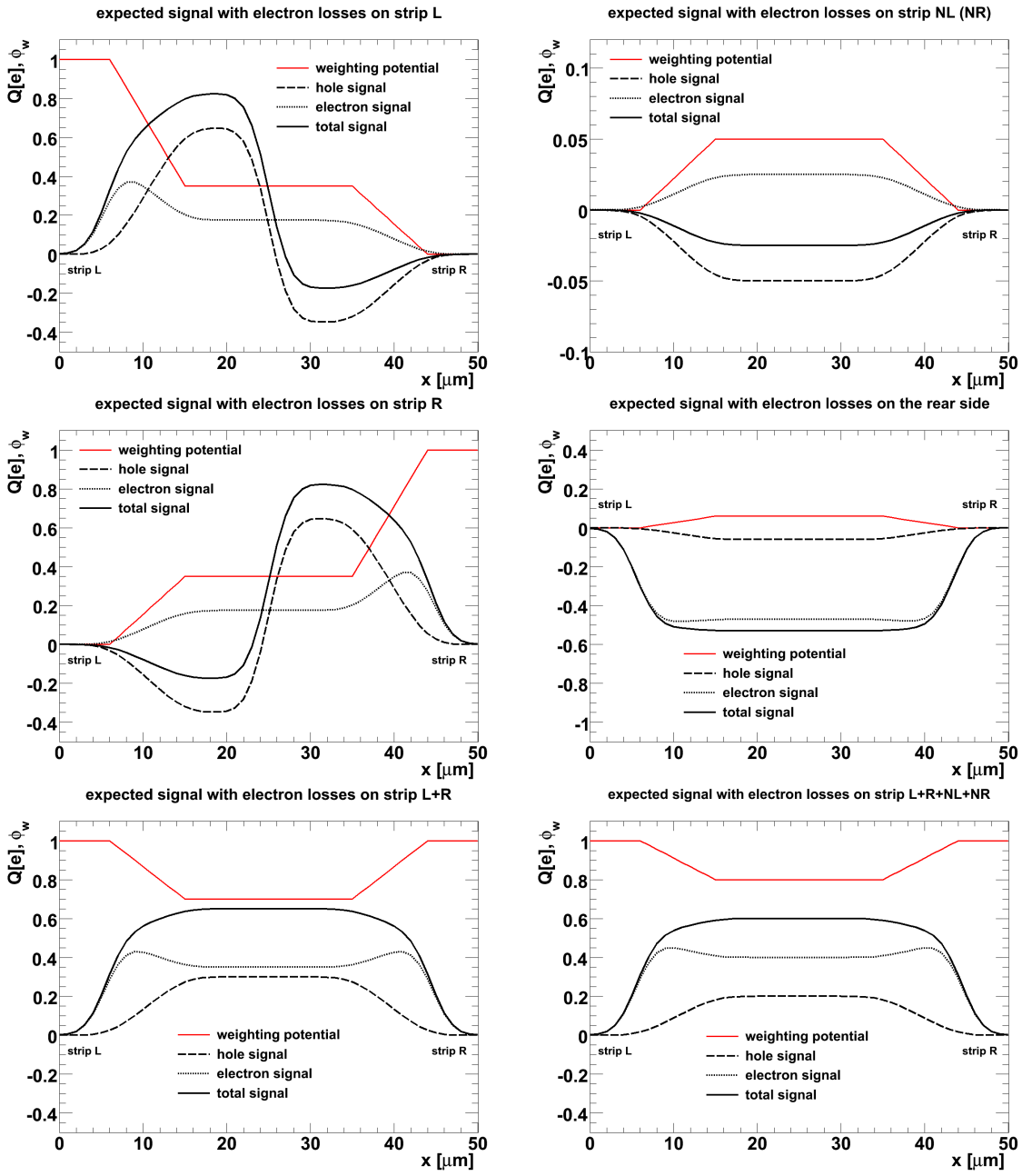

Figure 4.6: Weighting potential and expected hole and electron signals as a function of the position x of the light spot between the strips L and R for the situation of 100 % hole collection and 50 % electron losses. The signals are normalised to one produced electron-hole pair. For more details see text.

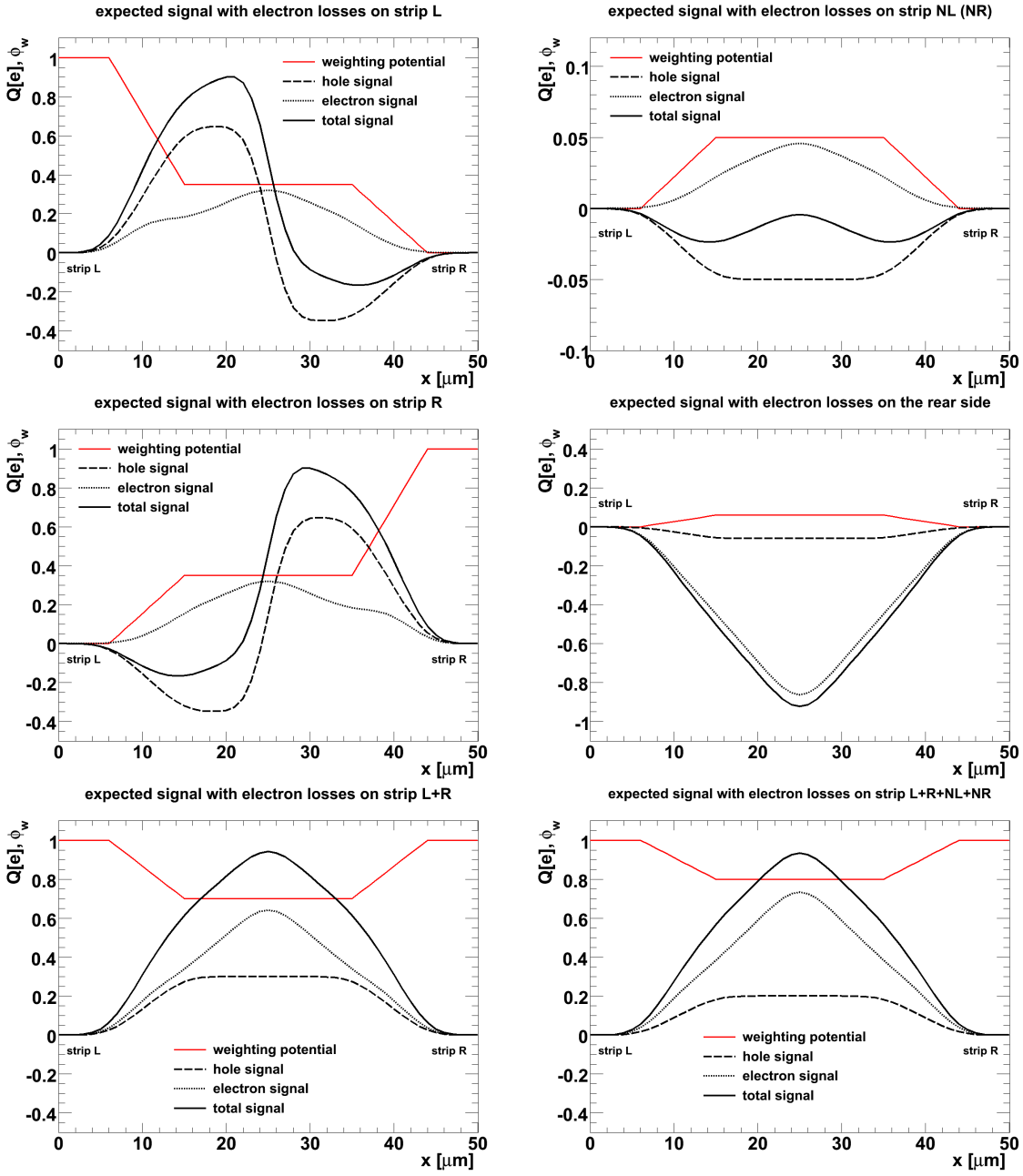

Figure 4.7: Weighting potential and expected hole and electron signals as a function of the position x of the light spot between the strips L and R for the situation of 100 % hole collection and position-dependent electron losses (100 % at the strip edge at $x = 6$ µm, and 0 % at the gap center at $x = 25$ µm). The signals are normalised to one produced electron-hole pair. For more details see text.

Similar formulae apply for strips R and NR.

The individual parameters of the model are:

- x_0, the position of strip L relative to the zero of the moving stage of the laser (free); (x is replaced by $x - x_0$ in the fit),
- the width of the Al strips: $d_{Al} = 14$ µm (fixed),which is assumed to have zero light transmission; it should also be noted that the actual width of the p^+ implant is 11 µm and the metal overhang over the oxide 2 µm,
- $N_e(x) = N_e^c + (N_e^e - N_e^c) \cdot \frac{|0.5 \cdot pitch - x|}{0.5 \cdot (pitch - d_{Al})}$, with N_e^c the number of electrons contributing to the signal in the gap centre, N_e^e the number of electrons contributing to the signal at the Al edge of the strip, and the strip pitch *pitch*,
- N_h, the number of holes contributing to the signal (free), which is assumed to be independent of x,
- d_{acc}, the width of the accumulation layer, which corresponds to the plateau of the weighting potential (free, however, can only be determined if either hole or electron losses occur),
- the weighting potentials at the accumulation layer: 0.35 for the strips adjacent to the accumulation layer, 0.05 for the next to neighbour strips, and 0.06 for the rear contact (all fixed),
- three parameters for the shape of the light spot (all fixed): Two Gaussians with widths $\sigma_{light}^{(1)} = 3$ µm and $\sigma_{light}^{(2)} = 9$ µm and relative normalisation 3 : 1; this shape is derived from the measurements reported in Chapter 3, and is compatible with the laser spot measured using a metal edge on a pad sensor,
- the parameter of the hole diffusion σ_{diff} (free), which is parameterised by

$$f_L^{diff}(x) = 0.5 \cdot (1 + \mathrm{erf}((0.5 \cdot pitch - x)/\sigma_{diff}));$$

  $f_L(x)$ is obtained by convoluting $f_L^{diff}(x)$ with the two Gaussians describing the light spot.

The free parameters of this model are obtained from a fit to the measured distributions of the signals from strip L and the rear contact when the laser is moved from $x = -100$ µm to $x = 100$ µm in steps of 2 µm.

4.2.3 Results

In order to study the charge losses close to the Si-SiO$_2$ interface as a function of the irradiation dose, environmental conditions (humidity) and biasing history, many measurements have been

performed for the two sensor types. They will be documented in [Section 4.5]. Here we only show a limited number of results for the DC-coupled Hamamatsu sensor, which are typical for the effects observed. The effects observed for the AC-coupled CiS sensor are similar.

Evidence for charge losses

In this section three measurements are presented, which are examples for the situations of no charge losses, of electron losses, and of hole losses. The measurements were performed at room temperature and at a bias voltage of 200 V:

- "humid – 0 Gy": non irradiated sensor biased to 200 V in a humid atmosphere (relative humidity > 60 %),
- "dried at 0 V – 1 MGy": irradiated sensor (1 MGy) stored at 0 V for a long time, then put into a dry atmosphere for > 60 minutes (relative humidity < 5 %), and then biased to 200 V for the measurements,
- "dried at 500 V – 0 Gy": non-irradiated sensor kept for a few hours at 500 V in a humid atmosphere (relative humidity > 60 %), then dried for > 60 minutes and afterwards biased in the dry atmosphere to 200 V for the measurements.

For the values of oxide charge density, N_{ox}, interface trap density, N_{it}, and surface current density, I_{surf}, for the irradiated and non-irradiated sensor we refer to Table 4.2.

As will be shown later, a sensor is not in a steady state after the bias voltage is changed, and the time constant to reach the steady state depends on the humidity of the surrounding atmosphere: It is of the order days in a dry atmosphere and two orders of magnitude shorter in a humid atmosphere.

The measurements for "humid" were started ∼20 minutes after reaching the bias voltage of 200 V, the ones for "dry" after ∼5 minutes. The focussed light with an attenuation length of ∼3.5 µm in silicon, was scanned in steps of 2 µm from $x = -100$ µm to $x = 100$ µm and the signals from strips L and R, and from the rear contact were recorded by the digital oscilloscope with 10 Gsamples/s. As shown in Figure 4.1, $x = 0$ corresponds to the centre of strip L. The repetition rate of the laser was 1 kHz. In order to reduce the fluctuations due to random noise the average of 5 000 pulses has been taken. One light scan took ∼90 minutes.

Figure 4.8 shows, as a function of the position x of the light spot, the charge collected within 25 ns on strips L, R, NL, on the rear contact, the sums L + R, and the sums for all four strips NL + L + R + NR for the three measurement conditions. The signal NL was not measured simultaneously with strips L and R, but obtained from the signal in strip L, when the laser spot was to the right of strip R. The signal NR was obtained in an analogous way. The comparison with the expectations shown in Figures 4.5 and 4.6 allows to interpret the data:

- "humid – 0 Gy" resembles the situation without charge losses shown in Figure 4.5: The signal from strip L has a broad maximum for x values between 10 and 20 µm. However, the transition in between the strips at $x = 25$ µm in the data is much more gradual than expected, an indication that ignoring diffusion might be a crude approximation. The signals in NL and NR are zero, and the rear side signal is the negative of the signal L + R, as expected for zero charge losses,

- "dried at 0 V – 1 MGy" resembles the situation of electron losses shown in Figure 4.6: The signal from strip L shows a broad maximum for x values between 10 and 20 µm, followed by a sharp drop at $x = 25$ µm, reaching negative values above 30 µm. The signals in NL and NR are negative as expected for electron losses. As the sum signals L + R and L + R + NL + NR without charge losses as well as the rear-sides signal are dominated by the electrons, the electron losses result in a strong reduction of these signals,

- "dried at 500 V – 0 Gy" agrees with the expectations from hole losses: The x dependencies are quite similar to the electron signal shown in Figure 4.5, and a small positive signal is induced in strips NL and NR. Both the rear-side signal as well as the sum signals are only slightly reduced compared to situation of no charge losses.

Fitting the model discussed in Section 4.2.2 to these measurements gives the values for the free parameters shown in Table 4.3.

For all these measurements the laser has been adjusted to the same intensity, corresponding to approximately 140 000 produced eh-pairs with an uncertainty of ∼5 %.

For "humid – 0 Gy" the fit indicates that in the centre between the strips there are electron losses of ∼10 %, no electron losses close to the readout strips, and hole losses of ∼7 %. The width determined for the accumulation layer of 34 µm is close to the distance of 39 µm between the p^+-implants. However, given the systematic uncertainties of the model, the results could also be compatible with zero charge losses. In this case the value of d_{acc} cannot be determined by this method.

For "dried at 500 V – 0 Gy" hole losses of ∼55 % and a width of the accumulation layer of 31 µm are found. The data for "dried at 0 V – 1 MGy" show that there is an accumulation layer of 36 µm covering most of the region between the p^+-implants, and practically all electrons are lost. This can be directly seen in Figure 4.8 where the signal measured at the rear contact has practically disappeared. In addition, hole losses of about 12 % are observed.

The measured current transients shown in Figure 4.9 confirm above interpretation of the data, in particular of no or little charge losses for "humid – 0 Gy", electron losses for "dried at 0 V – 1 MGy", and hole losses for "dried at 500 V – 0 Gy". Shown are the transients for the two strips L and R at the positions of the light spot $x = 12$ µm, which is about 5.5 µm from the edge of the aluminum of strip L, and at $x = 20$ µm, 5 µm away from the centre between the strips towards strip L.

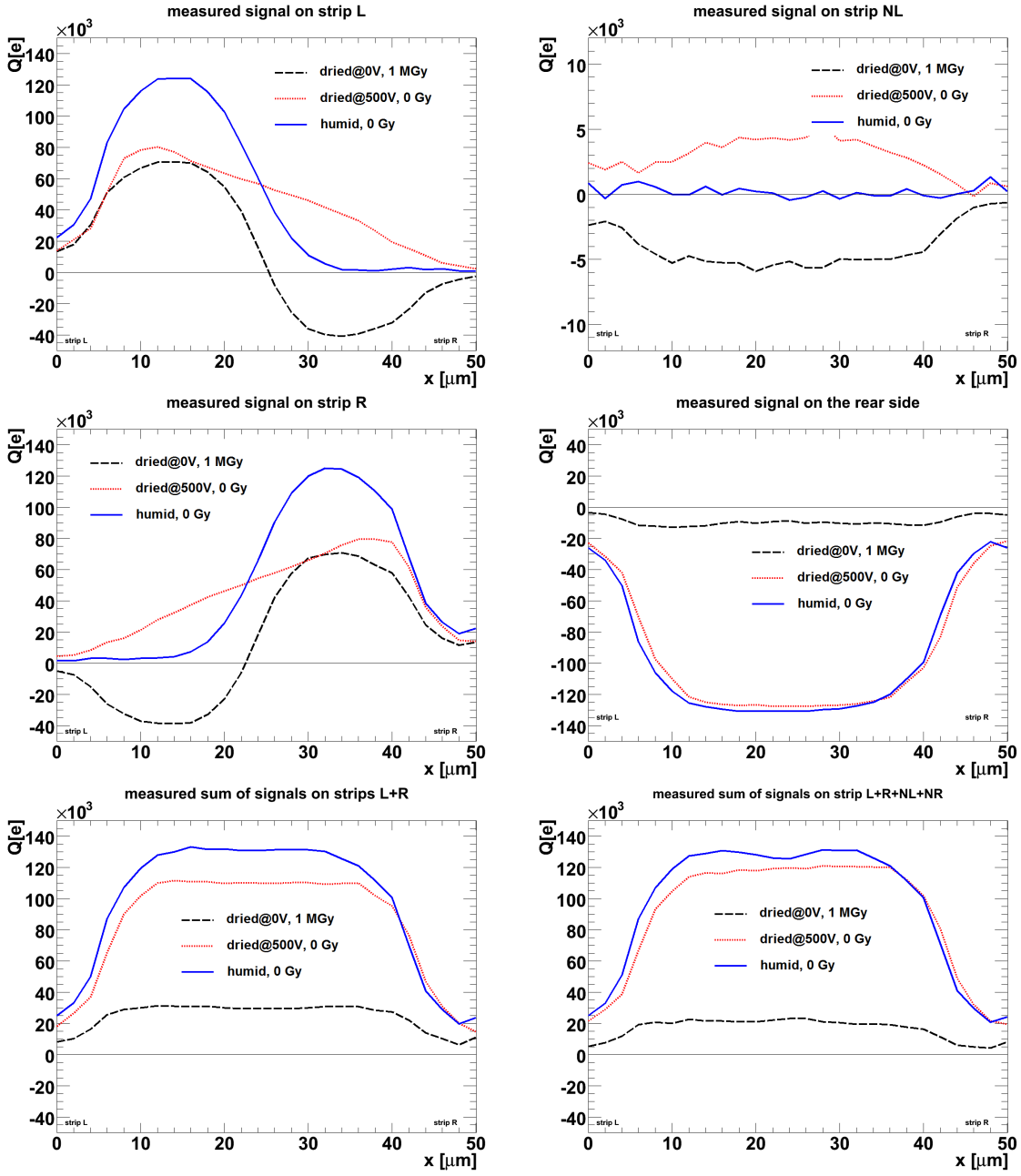

Figure 4.8: Charge signals measured in strips L, R, NL, NR and the rear contact and summed signals as function of the position x of the light spot between strips L and R for the three sets of measurements described in the text. For the definition of x, see Figure 4.1. "humid – 0 Gy", "dried at 0 V – 1 MGy", and "dried at 500 V – 0 Gy", correspond to the situations "no losses", "electron losses" and "hole losses".

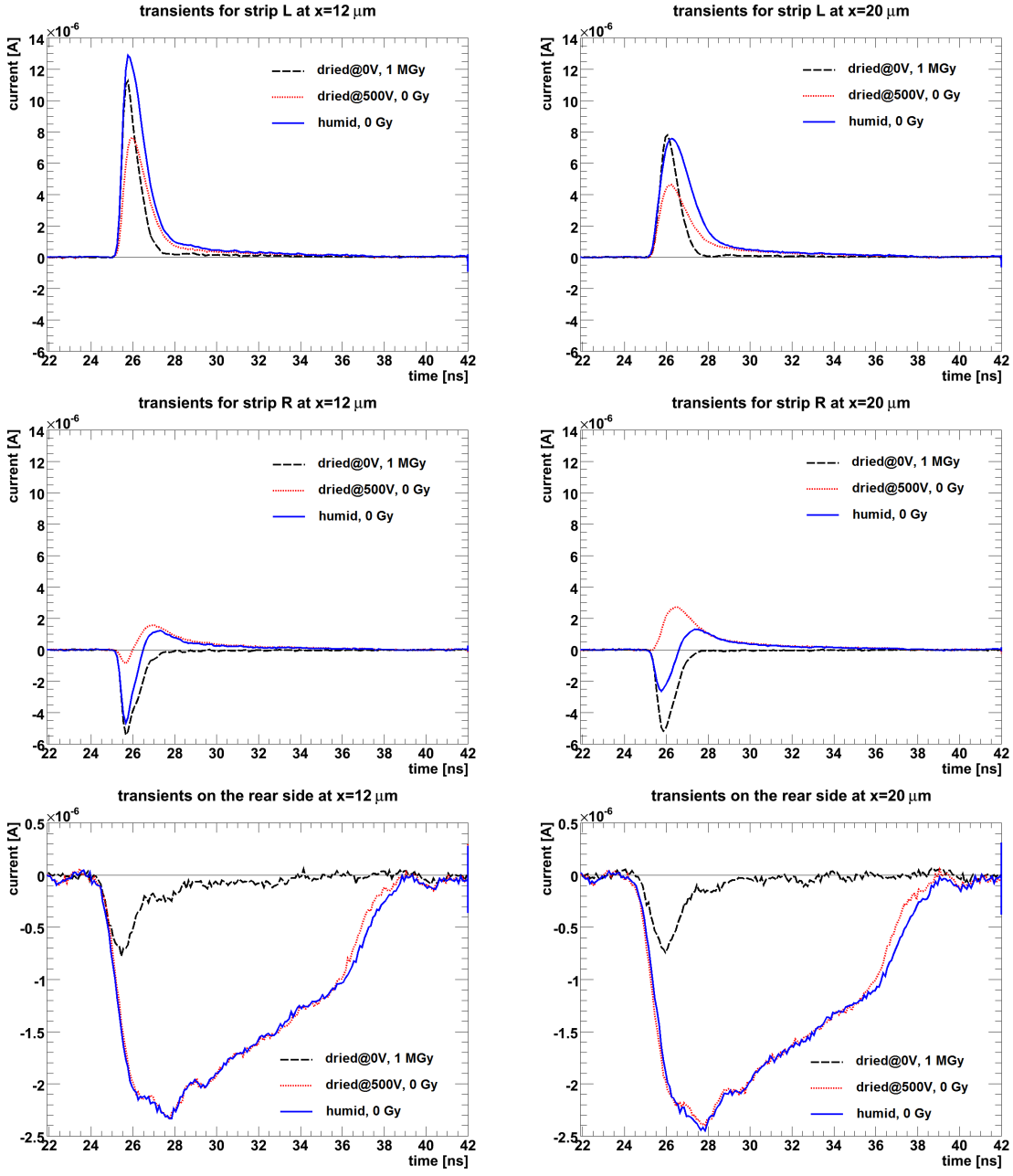

Figure 4.9: Measured transients on strips L and R and the rear contact for light injected at the two positions $x = 12$ μm and $x = 20$ μm for the three sets of measurements described in the text. "humid – 0 Gy", "dried at 0 V – 1 MGy", and "dried at 500 V – 0 Gy", correspond to the situations "no losses", "electron losses" and "hole losses".

	humid 0 Gy	dried@500 V 0 Gy	dried@0 V 0 Gy	humid 1 MGy	dried@0 V 1 MGy	dried@500 V 1 MGy
N_e^c	128 000	129 000	53 000	109 000	0	123 000
N_e^e	143 000	145 000	63 000	72 500	9 400	124 000
N_h	133 000	64 000	133 000	121 000	126 000	112 000
x_0	0.90 µm	1.83 µm	- 0.18 µm	1.64 µm	0.77 µm	0.80 µm
d_{acc}	(34 µm)	31 µm	36 µm	34 µm	36 µm	(6 µm)
σ_{diff}	2.7 µm	14.1µm	3.1 µm	2.2 µm	2.1 µm	5.4 µm

Table 4.3: Results of the fits using the model described in Section 4.2.2. Values of d_{acc} in parenthesis indicate that the charge losses are insufficient for a reliable determination of the width of the accumulation layer. The laser is adjusted to generate ∼140 000 eh-pairs.

At $x = 12$ µm:

- For strip L in all three cases positive signals are observed. Compared to no charge losses ("humid – 0 Gy"), the signal is shorter for electron losses ("dried at 0 V – 1 MGy"), as the electrons which drift through the entire sensor generate the signal at later times. For hole losses ("dried at 500 V – 0 Gy") the signal is correspondingly smaller at short times.

- For strip R, for no charge losses, a bipolar signal with an integral of zero is observed. The initial negative signals are due to holes drifting away from strip R minus a positive signal from the electrons moving towards strip R. Once the holes are collected the positive signal from the electrons drifting towards the rear contact remains. For electron losses there is just the negative signal due to the holes drifting away from strip R, and for hole losses there is essentially just the longer positive signal due to the electrons drifting through the entire sensor.

- For the rear contact the signal is mainly due to electrons, and the holes drifting to the strips contribute only little to the signal. Therefore, the signals with and without hole losses are essentially identical. For electron losses the signal is drastically reduced and a small fast negative signal due to the holes drifting to the readout strip is observed. The signal from the rear contact, which has the biggest capacitance, shows some ringing at a frequency of about 1 GHz.

At $x = 20$ µm:

- For strip L, for electron losses and for no charge losses, a shift of the peak to later times is observed compared to $x = 12$ µm, due to the longer distance the holes have to drift. For no charge losses the signal at strip L is reduced, which is described in the model by holes diffusing to strip R.

- For strip R, corresponding effects are observed: For electron losses a shift of the negative peak to later times, for no charge losses an increased signal (holes diffusing to strip R),

and for hole losses the negative part of the signal is absent, and only a positive signal mainly due to electrons remains.

- As expected, for the rear side little dependence of the signal on the x position is observed.

To summarise: Convincing evidence has been found for situations with little or no charge losses, complete hole collection and significant electron losses, and complete electron collection and significant hole losses. The signals from the readout strips and the rear contact as a function of the position of the laser spot can be described by the model presented, which allows determining quantitatively the charge losses and the width of the accumulation layer at the Si-SiO$_2$ interface.

Time constants to reach stable charge losses

Above it has been shown, that significant hole losses are observed for the non-irradiated sensor biased at 200 V for the scenario "dried at 500 V – 0 Gy", and hardly any charge losses for "humid – 0 Gy". Next we show that, after changing the voltage from 500 V to 200 V, the hole losses decrease with time, with a time constant which depends on the humidity.

For this measurement approximately 100 000 eh-pairs were generated by the laser light at $x \approx 25$ µm, close to the centre between the strips L and R. The hole losses are calculated from Q_{NL}, the signal measured on strip NL, using $Q_{NL}/(q_0 \cdot 0.05)$. For the weighting potential a value of $\phi_w^{NL} = 0.05$ is assumed, and q_0 is the elementary charge. The measurements were made at room temperature in a dry (relative humidity < 5 %) and a humid (> 65 %) atmosphere. The results are shown in Figure 4.10. At time $t = 0$, when the voltage was changed from 500 to 200 V, approximately 65 % of the holes are lost. As a function of time, the hole losses decrease following an S-shaped curve and finally reach a steady state of little hole losses. The shape of the curves are similar for "dry" and "humid", the time constants however, are very different: The reduction to 50 % of the initial losses is reached after ∼40 minutes for "humid", and after ∼80 hours for "dry". The measurements were made once in the middle of the ∼8 mm long strips, and once ∼1 mm from the end of the strips, where the openings in the passivation layer for the bonding are located. The results are similar. In Section 4.2.4 the explanation for these results will be given: The change of the charge losses with time is due to the change of the charge distribution on the surface of the sensor, which influences both the field close to the Si-SiO$_2$ interface as well as the extension of a possible accumulation or inversion layer. The time constant for reaching the steady-state conditions depends on the surface resistivity, which is a strong function of humidity. We note that the situation for the irradiated sensor is quite different. In particular, for "humid – 1 MGy" the steady state situation is reached on a much shorter time scale [Section 4.3].

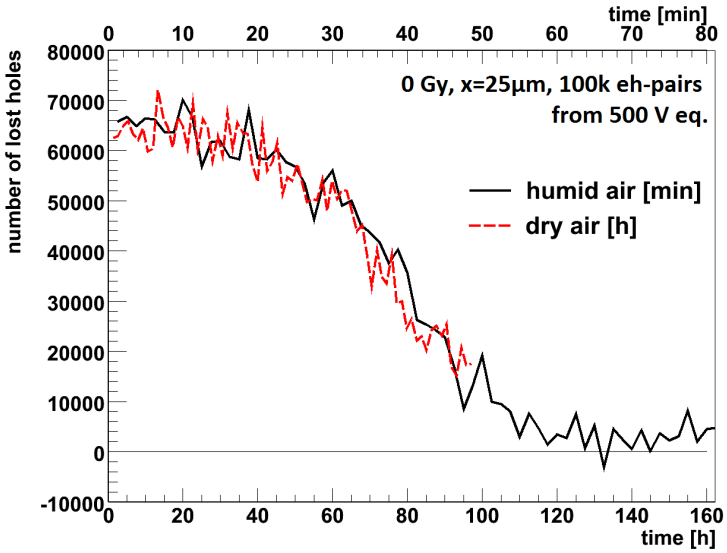

Figure 4.10: Number of holes lost for light pulses generating ∼100 000 *eh*-pairs as a function of the time after the voltage applied to the non-irradiated sensor has been reduced from 500 V in steady-state conditions, to 200 V . The upper scale of the horizontal axis (in minutes) refers to the situation "humid", the lower one (in hours) to "dry".

Correlation of the dark current and the accumulation layer width

For X-ray irradiated sensors the dark current is expected to be dominated by the surface generation current from the depleted Si-SiO$_2$ interface. As the width of the depleted Si-SiO$_2$ interface is $d_{gap} - d_{acc}$, where d_{gap} is the distance between the p^+ implants and d_{acc} the width of the accumulation layer, an anti-correlation of the dark current and the width of the accumulation layer is expected. Table 4.4 shows for the 1 MGy-irradiated sensor biased at 200 V for the three experimental conditions: "dried at 0 V – 1 MGy", "humid – 1 MGy", which corresponds to steady-state conditions on the sensor surface, and "dried at 500 V – 1 MGy" the measured dark currents for a single strip, I_{dark}^{meas}, the widths of the accumulation layer, d_{acc}^{fit}, determined from the fits, and the widths of the accumulation layer, d_{acc}^{calc}, calculated from the measured dark current and the value of the surface generation current $I_{surf} = 2.2$ µA/cm^2 from Table 4.2. For the measurement "dried at 500 V – 1 MGy" the charge losses are small and d_{acc} cannot be determined reliably. The agreement is certainly not perfect, however qualitatively the results are similar, and give us some confidence in the method used to determine the widths of accumulation layers from the TCT measurements. Also the measured time dependence of the dark current to a steady state (not shown) agrees with the measured time dependence to reach a steady state for the charge losses, which has been discussed in the previous Section.

	dried at 0 V – 1 MGy	humid – 1 MGy	dried at 500 V – 1 MGy
I_{dark}^{meas}	1.2 nA	1.8 nA	3.3 nA
d_{acc}^{fit}	36 µm	34 µm	-
d_{acc}^{calc}	32 µm	29 µm	21 µm

Table 4.4: For the sensor irradiated to 1 MGy, biased at 200 V under three different measurement conditions: I_{dark}^{meas}, the dark current for a single strip, d_{acc}^{fit}, the width of the accumulation layer determined from the fit, and the width of the accumulation layer, d_{acc}^{calc}, obtained from the measured dark current, the surface generation current from the test structures (Table 4.2), and the geometrical parameters of the sensor (Table 4.1). The current values refer to a temperature of 22.9 °C

.

Charge losses as a function of voltage for the irradiated sensor

As discussed before, electron losses are observed for the irradiated sensor for the measurement conditions "humid – 1 MGy" and "dried at 0 V – 1 MGy". Here we present the number of holes and electrons collected as a function of the applied voltage ramped up from 0 to 500 V in 50 V steps with the sensor in a dry atmosphere (relative humidity < 5 %). At each voltage a position scan between $x = -100$ µm and $x = 100$ µm was performed. A position scan took ∼1.5 hours, and there may be some time effects, in particular at longer times and thus at the higher voltages. The number of generated eh-pairs was approximately 30 000. The number of collected electrons and holes is determined from the fit of the model described in Section 4.2.2 to the data.

The results are shown in Figure 4.11. The number of holes collected shows a small increase between 50 and 150 V, and then remains constant. Up to 150 V practically no electrons are collected at the center between the strips. Above this voltage the fraction of electrons collected increases approximately linearly with voltage, reaching ∼25 % at 500 V. The fraction of electrons collected close to the edge of the readout strips, increases from ∼5 % to ∼40 %. We note that for all voltages significant electron losses are observed and, that the width of the accumulation layer, d_{acc} (not shown), is between 34 and 36 µm. Thus the accumulation layer covers most of the 39 µm wide gap between the p^+-implants. We also observe (not shown) that the diffusion term is below 3 µm, the width of the light spot.

4.2.4 Discussion of the results

In this Chapter an attempt is made to qualitatively interpret the results and discuss their relevance for the operation of p^+n sensors. We first discuss the cause of the charge losses and their dependence on time and humidity. Our explanations are supported by detailed two-dimensional simulations of the sensor assuming different boundary conditions on the surface of the passivation and different values of $q_0 \cdot N_{int}^{eff} = q_0 \cdot (N_{ox} + N_{it}^{don} - N_{it}^{acc})$, the effective charge density at or close to the Si-SiO$_2$ interface. q_0 is the elementary charge, N_{ox} the density of positive oxide charges, and N_{it}^{don} and N_{it}^{acc} the density of filled donor and

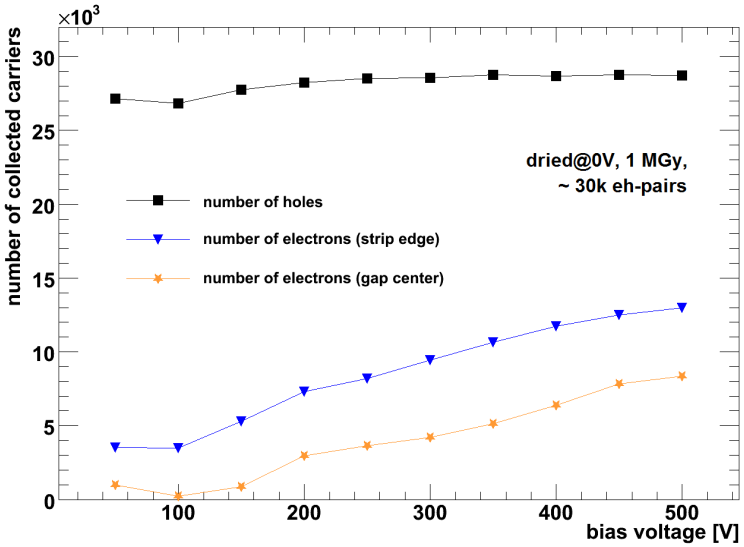

Figure 4.11: Irradiated sensor operated in a dry atmosphere for voltages between 50 and 500 V: Number of electrons collected for light injected in the middle between and close to the readout strip, and number of holes collected. The number of *eh*-pairs generated by the light is approximately 30 000.

acceptor states at the interface, integrated over the silicon band gap.

Charge losses and their time dependence

For the non-irradiated strip sensor the most relevant results, which were presented in Chapter 3, are:

- Electron losses when ramping up the voltage in a dry atmosphere ("dried at 0 V – 0 Gy"),
- hole losses when ramping down the voltage in a dry atmosphere ("dried at 500 V – 0 Gy"),
- no or little charge losses in a humid atmosphere ("humid – 0 Gy"), and
- the time to reach the steady state after a voltage change is about an hour in a humid and ∼100 hours in a dry atmosphere.

We explain these observations in the following way: We assume that the sensor is in steady-state conditions at 0 V with zero charge density on its surface. When the sensor is biased, parts of the p^+ implants will be depleted, resulting in negative charges at the p^+n junctions of the strips. These negative charges are balanced by the positive charges of the depleted n bulk and of the n^+ implant of the rear contact, if the sensor is biased above depletion. These charges produce an electric field at the Si-SiO$_2$ interface and at the sensor surface. If surface charges on top of the passivation do not move, the electric field at the surface will have a longitudinal component which points to the p^+ implants and a transverse component at the

Si-SiO$_2$ interface which points into the sensor [2]. This is seen in the top left plot of Figure 4.12, which shows for a sensor biased to 200 V a TCAD simulation of the longitudinal surface field for a density $N_{int}^{eff} = 10^{11}$ cm^{-2} and zero surface-charge density. This longitudinal surface field, which reaches values of 100 kV/cm in the simulation, will cause the redistribution of surface charges until a uniform surface potential is reached. This is the steady-state condition for a given applied voltage. As the effective surface conductivity increases with increasing humidity, the steady state will be reached in a shorter time for humid than for dry conditions. The left plot of Figure 4.13 shows the simulated surface charge distribution for $N_{int}^{eff} = 10^{11}$ cm^{-2}, the p^+ implants at 0 V, and the rear contact at 200 V, which approximately represents the steady-state condition. The potential on the surface is also set to 0 V. In principle the potential on the surface should have been set to a voltage so that the integrated charge on the surface is zero. We however did not manage to perform such a simulation. A crude estimation indicates that the surface potential is between 1/3 to 1/2 of the potential of the accumulation layer.

If the sensor is in steady-state conditions under bias and the voltage is ramped down, the field direction will be opposite to the situation discussed above: The transverse component of the electric field will point into the SiO$_2$ and the longitudinal component of the surface field will point away from the p^+ implants. This can be seen at the bottom left plot of Figure 4.12, which shows the simulated longitudinal field distribution for the sensor initially in steady-state conditions at 500 V and then biased to 200 V in a dry atmosphere, i.e. assuming the surface charge distribution from the steady-state simulation at 500 V. We note, that the maximum value of the simulated surface field is only 25 kV/cm, significantly smaller than the value for the case discussed above. The wiggles in the curves are an artifact of the simulation: The surface charge distribution at 500 V has been parameterised by the sum of 10 Gaussians. We stress that, given the assumptions made in the simulations, the results should be understood as indicative only.

For completeness we also show on the right sides of Figures 4.12 and 4.13 the simulated surface fields and surface-charge distributions for a density $N_{int}^{eff} = 10^{12}$ cm^{-2}, which corresponds to a sensor with X-ray radiation damage. We note that qualitatively the results are similar to the non-irradiated situation. However, both the surface fields and the surface-charge densities are significantly higher than for the non-irradiated sensor.

The dependence of the surface sheet resistance, $R_\square$, on humidity, and the impact on the performance of MOS structures, are well documented [57, 58, 59]. Under the simplified assumption that the sheet resistance is independent of the electric field, the time dependence of the distribution of the surface charge on the way to the steady state scales with $R_\square$. This scaling is observed in the measurements shown in Figure 4.10. The ratio of the time constants of $\sim$120 is compatible with values from the literature. A crude estimation of the surface

[2] In the simulation this is realised by defining a boundary at $y = -100$ µm where Neumann boundary conditions are applied. On the surface of the passivation layer, fixed charges, in this case zero, are put. For the simulation "dried at 500 V" the surface-charge distribution obtained for the steady-state conditions at 500 V is used.

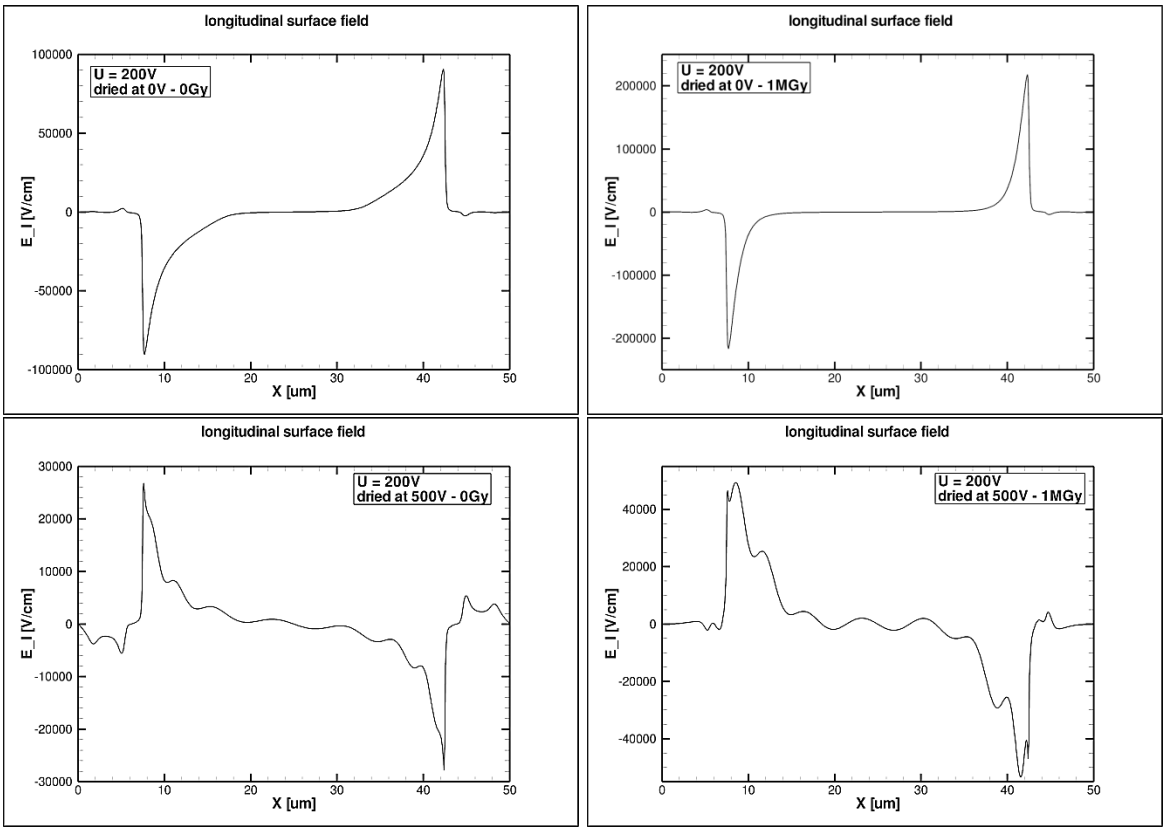

Figure 4.12: Simulated longitudinal component of the surface field for the sensor biased to 200 V under dry conditions. Left: Non-irradiated sensor ($N_{int}^{eff} = 10^{11}$ cm^{-2}); right: Irradiated sensor ($N_{int}^{eff} = 10^{12}$ cm^{-2}); top: Steady-state conditions at 0 V, and bottom at 500 V. The strips are centred at $x = 0$ and 50 µm.

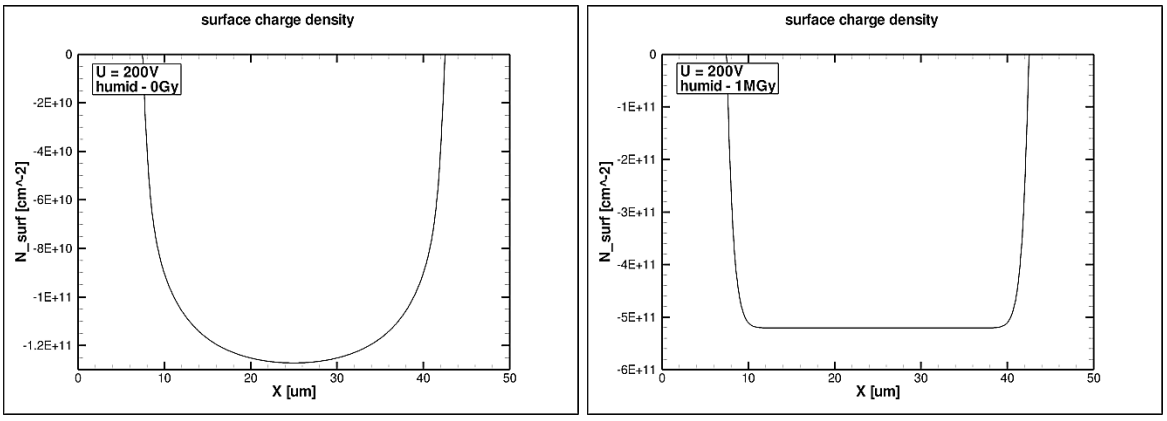

Figure 4.13: Simulated distribution of the charge-carrier density on the surface of the sensor biased to 200 V for steady-state conditions. Left: Non-irradiated sensor ($N_{int}^{eff} = 10^{11}$ cm^{-2}); right: Irradiated sensor ($N_{int}^{eff} = 10^{12}$ cm^{-2}).

resistivity, following the approach presented in [60], gives values for $R_\square$ of the order of 10^{17} Ω for the humid, and approximately a factor 120 higher for the dry conditions. Similar values for $R_\square$ are reported in [59, 60].

In Section 4.2.3 we have mentioned that the time it takes to reach the steady state on the surface of the sensor does not depend on the distance between the injected light and the end of the strips where the openings in the passivation are located. This agrees with the expectation that the steady state on the sensor surface is reached by a local redistribution of the surface charges, and not by charges moving from or to the bond pads.

Next we explain the reasons for the different type of charge losses for the different measurement conditions with the help of selected TCAD simulations [11]. Figures 4.14 and 4.15 show simulated distributions of the electric potential and of the electron and hole densities in the sensor close to the Si-SiO$_2$ interface for different measurement conditions. We start by discussing the situation of significant electron losses, which are observed for the condition "dried at 0 V – 0 Gy". For an explanation of the nomenclature we refer to Section 4.2.3.

We assume that in steady-state conditions with the strips and the rear contact at 0 V, the charge density on the surface of the sensor is zero. If the sensor is biased to 200 V in the condition "dried at 0 V – 0 Gy" the surface-charge density remains zero, and an electron-accumulation layer forms below the Si-SiO$_2$ interface as seen by the high electron density visible in the middle left plot of Figure 4.15 and the top plot of Figure 4.16: The electron density reaches a maximum value of $\sim 3 \cdot 10^{16}$ cm^{-3} at the interface for a depth of ∼5 nm in y. The white lines in Figures 4.14 and 4.15 indicate the electron density of $\sim 10^{12}$ cm^{-2}, which corresponds to the n doping of the sensor. Inspection of the corresponding potential distribution (middle left plot of Figure 4.14) shows, that the potential has a saddle point ∼5 µm below the Si-SiO$_2$ interface, and that the electric field points from the interface into the sensor. Thus holes produced close to the interface will drift in a short time along the field lines to the readout strips where they are collected. Hole losses due to recombination in the accumulation layer are estimated to be negligible. However, a fraction of the electrons produced close to the accumulation will reach the accumulation layer and, like those produced in this layer, will spread over the layer with a time constant given by the dielectric relaxation time $\tau_R = \varepsilon_{Si}/(q_0 \cdot \mu_e \cdot n)$. ε_{Si} denotes the dielectric constant of silicon, μ_e the electron mobility and n the position dependent electron density. For $n = 10^{15}$ cm^{-3} the value is $\tau_R = 5$ ps [59], which is short compared to the charge collection time of a few nanoseconds. These electrons are "lost", as they do not induce a significant signal within the integration time of the measurements. As they spread at least over the entire length of the accumulation layer along the sensor strips, the resulting increase in electron density and change of the local electric field will be quite small. A study of the impact of the number of electrons "lost" on the charge collection, and the time required to return to the pre-light injection state, is the topic of a separate publication ([43] and Chapter 4.4). We also note from Figure 4.15, that the depths of the electron-accumulation layers have their maxima in the symmetry plane between the readout strips and decrease towards the readout strips.

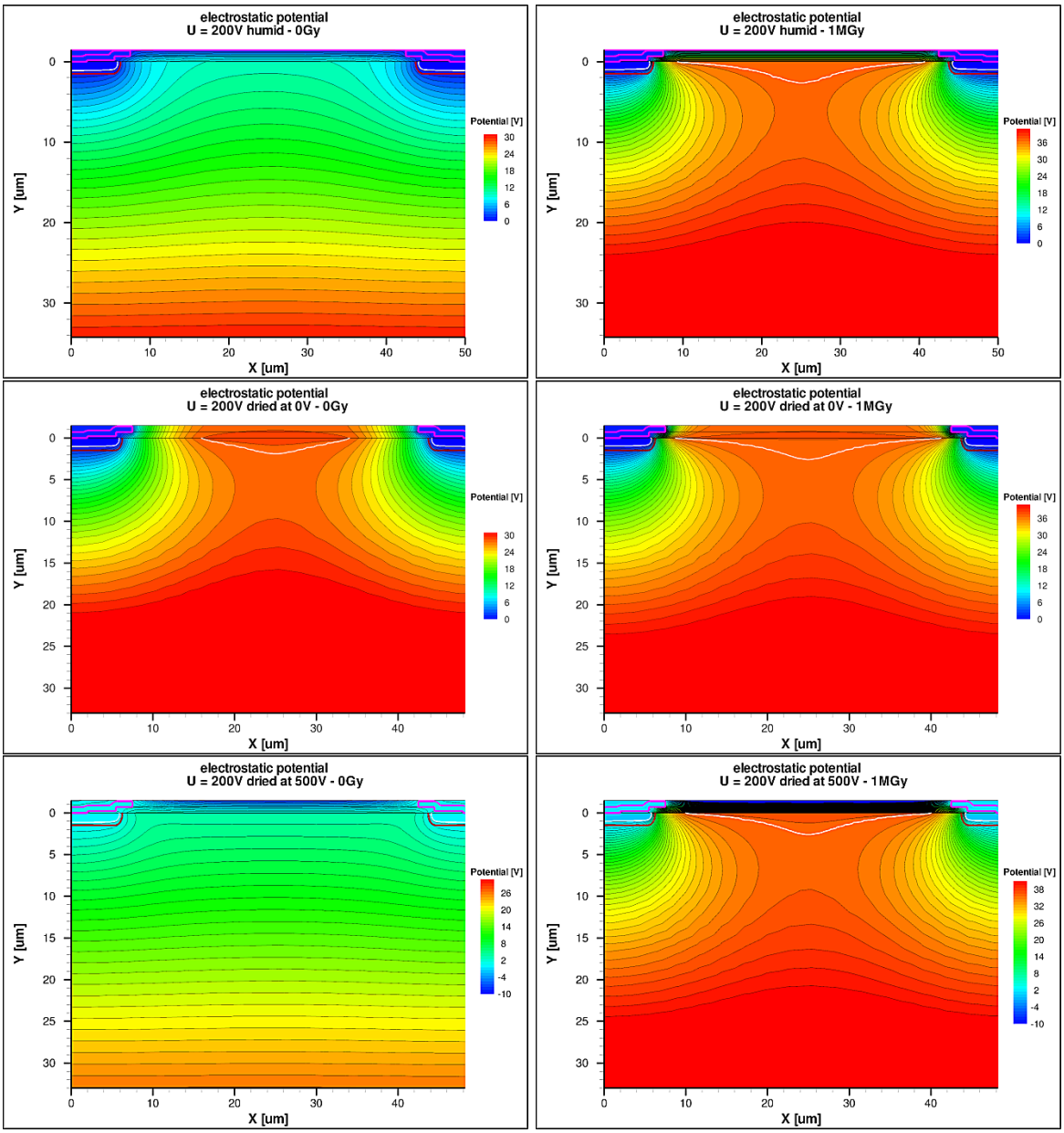

Figure 4.14: Simulated potential distribution for the sensor biased to 200 V: Non-irradiated (left - $N_{int}^{eff} = 10^{11}$ cm^{-2}) and irradiated to 1 MGy (right - $N_{int}^{eff} = 10^{12}$ cm^{-2}) for the conditions "humid" (top), "dried at 0 V" (middle) and "dried at 500 V" (bottom).

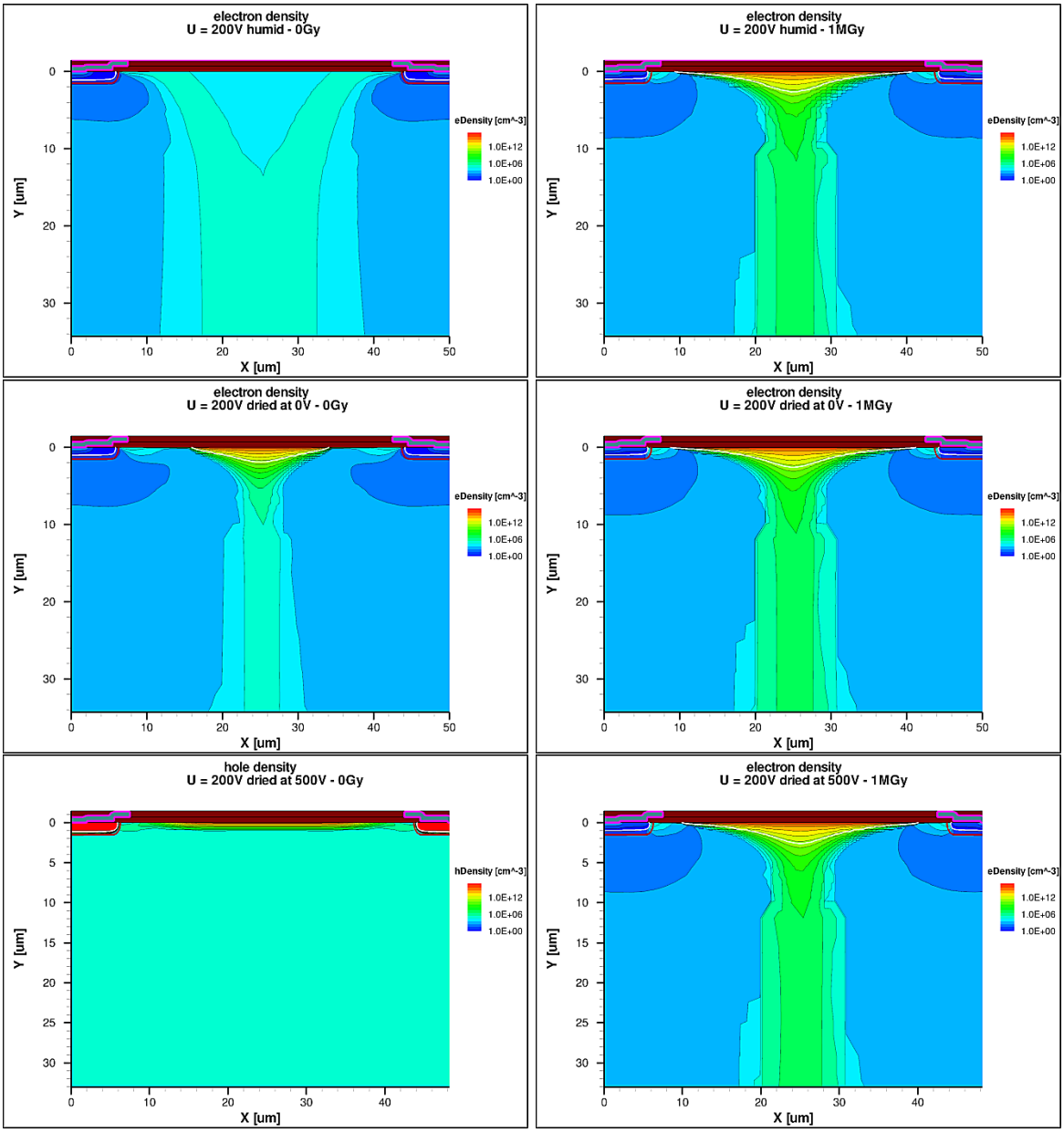

Figure 4.15: Simulated electron and hole densities close to the Si-SiO$_2$ interface for the sensor biased to 200 V: Non-irradiated (left - $N_{int}^{eff} = 10^{11}$ cm^{-2}) and irradiated to 1 MGy (right - $N_{int}^{eff} = 10^{12}$ cm^{-2}) for the conditions "humid" (top), "dried at 0 V" (middle) and "dried at 500 V" (bottom). Except for the bottom left plot, which shows the holes density, only the electron densities are shown.

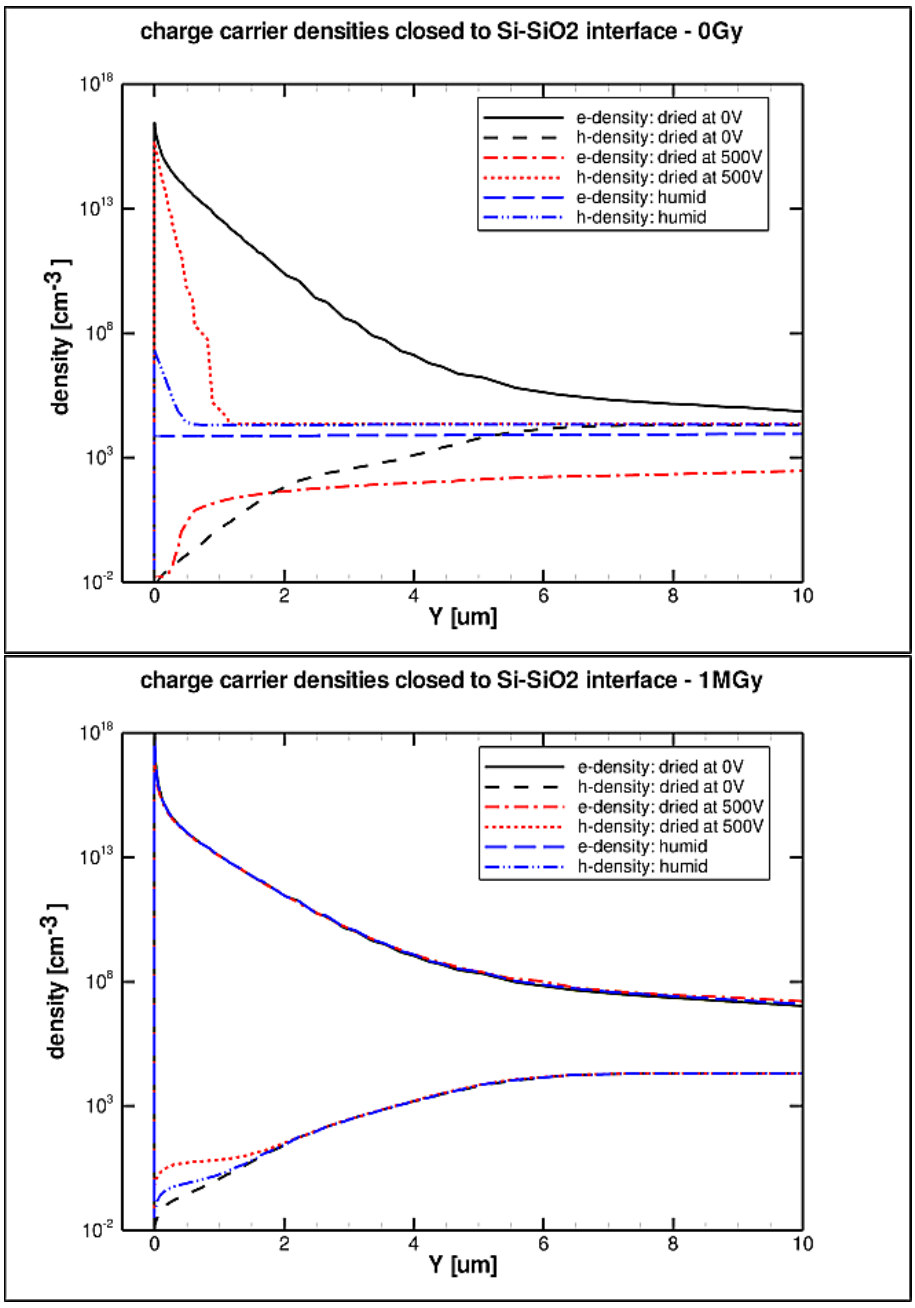

Figure 4.16: Simulated charge carrier densities close to the Si-SiO$_2$ interface in the symmetry plane between the strips for the sensor biased to 200 V and different measurement conditions. Left for $N_{int}^{eff} = 10^{11}$ cm^{-2}, corresponding to a non-irradiated sensor, and right for $N_{int}^{eff} = 10^{12}$ cm^{-2}, corresponding to a sensor irradiated to dose of 1 MGy. A high electron density at the interface ($y = 0$) is evidence for an electron-accumulation layer, a high hole density for an inversion layer.

Next we discuss the situation of hole losses which occur for the condition "dried at 500 V – 0 Gy". In this case the negative charges on the surface overcompensate the positive charges at the interface, and a hole-inversion layer forms below the Si-SiO$_2$ interface. This can be seen in the bottom left of Figure 4.15 and in Figure 4.16 as a high density of holes at the interface. The value found for the maximum hole density is $\sim 4 \cdot 10^{15}$ cm^{-3}. We note that the depth of the inversion layer is much smaller than for the accumulation layer and essentially independent of position x. The potential distribution presented in the bottom left plot of Figure 4.14 shows that the electric field distribution resembles the situation of a pad sensor: The electric field in the sensor points towards the Si-SiO$_2$ interface and the transverse field component is small. This explains the large value of the hole diffusion term σ_{diff} observed for this condition and reported in Table 4.3.

Finally we discuss the situation of no or little losses, which is observed for the condition "humid – 0 Gy". In this case the potential on the surface of the sensor is uniform, the redistributed surface charges compensate the positive interface charges of density N_{int}^{eff}, and neither an electron-accumulation nor a hole-inversion layer forms at the Si-SiO$_2$ interface. As shown in Figure 4.16 top, both electron and hole densities are below $\sim 10^8$ cm^{-3} at the Si-SiO$_2$ interface. From the corresponding potential distribution shown on the top left plot of Figure 4.14 we conclude, that the electric field close to the Si-SiO$_2$ interface is weak and points to the interface. Nevertheless, most holes generated in this region will diffuse until they reach a region of higher field and then drift to a readout strip.

The results of the simulations for the irradiated sensor for the three measurement conditions are shown on the right sides of Figures 4.14, 4.15 and the bottom of Figure 4.16. Given the high positive charge density at the interface of $N_{int}^{eff} = 10^{12}$ cm^{-2} electron-accumulation layers are present under all three conditions. Given that the charge densities change by 20 orders of magnitudes, the curves for the electron densities appear indistinguishable on top of each other. Nevertheless, the values at $y = 0$ are quite different: $2.5 \cdot 10^{18}$, $6 \cdot 10^{17}$ and $8 \cdot 10^{16}$ cm^{-3} for "dried at 0 V – 1 MGy", "humid – 1 MGy" and "dried at 500 V – 1 MGy", respectively. Qualitatively this dependence is expected from the differences in surface-charge distributions and also fits the measured numbers of the electrons and holes collected as presented in Table 4.3: Electron losses $\sim$90 % for "dried at 0 V – 1 MGy" and $\sim$30 % for "humid – 1 MGy". For the situation "dried at 500 V – 1 MGy", different to the expectation from the simulation, no or only minor electron or hole losses are observed. Given all the uncertainties in the assumptions made in the simulations, we are not worried by this difference. We note, that by changing the value of N_{int}^{eff} in the simulation, the accumulation layer also changes.

We summarise: The observed losses of electrons (holes) close to the Si-SiO$_2$ interface can be qualitatively understood by the shape of the electric field in the sensor close to the interface and by the formation of an electron-accumulation (hole-inversion) layer at the interface. Both are influenced by the distribution of charges on the surface of the sensor and by the density of charged states in the region of the Si-SiO$_2$ interface. The latter is a strong function of X-ray

radiation damage. After changing the sensor voltage it takes some time until the steady-state conditions of the surface-charge distribution are reached. The time constant, which can be as long as several days, depends on the humidity.

Relevance of the results

This chapter discusses the relevance of the measurements for the understanding, the design and the operation of segmented p^+n sensors.

First of all, the measurements give some insight into the complexities of the Si-SiO_2 interface and of possible effects of the properties of the passivation on sensors with and without surface radiation damage. They also show the difficulties in defining the correct boundary conditions on the surface of sensors, required for a realistic sensor simulation. Some insight has also been gained into the well known effect [49, 50] that, after changing the voltage it takes some time until steady-state conditions are reached and that the corresponding time constant is a strong function of the humidity [61]. Time constants can be as long as several days. Many users of silicon sensors have actually observed such "long-time run-aways". Depending on the design of the sensor, in particular if the metal of the strips does not overlap the SiO_2, breakdown at low bias voltages has been observed when the sensors are ramped up in a dry atmosphere [62]. We conclude that for sensors exposed to high doses of X-rays the oxide area not covered by metal should be minimized. However, the increase in capacitance and the resulting increase in readout noise has to be taken into account. For a hybrid pixel sensor, like the AGIPD sensor with a pixel size of 200 µm × 200 µm, a small inter-pixel gap of order 20 µm appears as a reasonable compromise.

Concerning the relevance for the efficient detection of radiation, we remind that light of 660 nm wavelength has an absorption length in silicon at room temperature of 3.5 µm and that the observed charge losses only occur close to the interface. Therefore the charge losses are relevant for short range particles only, like low-energy heavy ions entering the p^+ strip side of the sensor. It is clear from the studies presented, that the precise measurements of their energy is difficult and both positive and negative signals will appear on the readout strips. Such effects have actually been observed already quite some time ago [63] and a simplified explanation has been given.

For the detection of minimum-ionizing particles, the effects can certainly be ignored, as long as the thickness of the sensor is large compared to ∼50 µm. To the authors' knowledge, no effects of charge losses due to surface effects have been reported in such applications. The same is true for the detection of X-rays, in particular when they enter through the rear n^+ contact. As an example, for 12 keV X-rays the attenuation length is 250 µm and only 0.3 % of the photons convert in the last 5 µm of a 500 µm thick sensor. Measurements with light with 1052 nm wavelength, which also has an attenuation length of 250 µm, show no measurable charge losses and confirm this estimate.

One worry, which actually has triggered the study, is the situation which occurs at the European X-ray Free-Electron Laser, XFEL [1, 2]: $\sim 10^5$ photons of 12 keV will be deposited

within tens of femtoseconds in a pixel of size 200 µm × 200 µm followed by the next XFEL pulse after 220 ns. The question is: How long is the "memory" of the pixel for such large pulses, and does the memory change with surface damage? The studies presented show, that as far as surface effects are concerned, there are no problems: The charge lost locally in the accumulation layer spreads in picoseconds over the accumulation layer of the entire sensor. Plasma effects however, due to the high charge density generated by the high density of interacting photons, may very well result in memory times beyond the XFEL pulse spacing of 220 ns as shown in [18, 64, 8].

4.2.5 Summary

Using the Transient Current Technique, TCT, with sub-nanosecond focussed light pulses of 660 nm wavelength, the charge collection of p^+n strip sensors before and after 1 MGy of X-ray irradiation for charges produced close to the Si-SiO$_2$ interface has been investigated. The absorption length of 660 nm light in silicon at room temperature is 3.5 µm. Depending on applied bias voltage, bias history, humidity and X-ray irradiation, incomplete collection of either electrons or holes has been observed. The charge losses are due to electron-accumulation or hole-inversion layers at the Si-SiO$_2$ interface and the close-by electric field. The data can be described by a model which allows a quantitative determination of the losses of holes and electrons, and the widths of the accumulation and inversion layers below the Si-SiO$_2$ interface.

After changing the bias voltage, the charge distribution on the sensor surface is not in a steady state. The time it takes to reach steady-state conditions depends on humidity: Several days in a dry, and two orders of magnitude faster in a humid atmosphere. This difference is related to the decrease of surface resistivity with humidity.

For non-irradiated sensors little or no charge losses are observed when the surface of the sensor is in steady-state conditions. However, immediately after applying the bias voltage, electron losses occur when the voltage is increased, and hole losses when the voltage is decreased from a steady-state condition. For irradiated sensors electron losses are observed in steady state. The fraction of electrons lost increases when the voltage is ramped up after exposure to the initial test conditions, and decreases when ramped down.

The observations for sensors from two vendors built from silicon with different crystal orientations and different coupling of the aluminium strips to the p^+ implants are similar.

The results provide information on the surface-charge distribution and its impact on the accumulation or inversion layer, as well as on the electric field close to the interface of segmented sensors with and without X-ray-radiation damage. They also demonstrate the difficulties in defining the boundary conditions on the sensor surface for a realistic sensor simulation.

The observed charge losses are relevant for the detection of radiation with short attenuation length, like low-energy heavy ions, but have a minor effect for the detection of X-rays and minimum-ionizing particles for silicon sensors with thicknesses above 50 µm.

Acknowledgements

This work was performed within the AGIPD Project which is partially supported by the XFEL-Company. We would like to thank the AGIPD colleagues for the excellent collaboration. Support was also provided by the Helmholtz Alliance "Physics at the Terascale" and the German Ministry of Science, BMBF, through the Forschungsschwerpunkt "Particle Physics with the CMS-Experiment". J. Zhang is supported by the Marie Curie Initial Training Network "MC-PAD" We also are thankful to H. Spieler for essential advice and enlightening discussions.

4.3 Time developement of the electric field close to the Si-SiO_2 interface

This section is accepted for publication in Nuclear Instruments and Methods in Physics Research A with the title *Time dependence of charge losses at the Si-SiO_2 interface in p^+n-silicon strip sensors* [42].

Abstract

The collection of charge carriers generated in p^+n-strip sensors close to the Si-SiO_2 interface before and after 1 MGy of X-ray irradiation has been investigated using the transient current technique with sub-nanosecond focussed light pulses of 660 nm wavelength, which has an absorption length of 3.5 µm in silicon at room temperature. The paper describes the measurement and analysis techniques used to determine the number of electrons and holes collected. Depending on biasing history, humidity and irradiation, incomplete collection of either electrons or holes are observed. The charge losses change with time. The time constants are different for electrons and holes and increase by two orders of magnitude when reducing the relative humidity from about 70 % to less than 1 %. An attempt to interpret these results is presented.

4.3.1 Introduction

In this paper the time dependence of charge losses close to the Si-SiO_2 interface in p^+n-silicon strip sensors after changing the bias voltage in environments of different humidities is investigated. Measurements were performed on a non-irradiated sensor and on a sensor irradiated by ∼12 keV X-rays to a dose of 1 MGy. The work is part of the study of X-ray-radiation damage of segmented silicon sensors for the AGIPD detector [6, 7] at XFEL, the European X-ray Free-Electron Laser [1, 2], where X-ray doses of up to 1 GGy are expected.

In a previous publication [41] it has been shown that time resolved measurements (TCT - Transient Current Technique) for electron-hole pairs generated by a focussed laser close to the Si-SiO_2 interface, allows investigating the electric fields and the properties of possible accumulation layers. For a non-irradiated sensor it has been observed that, after biasing the sensor, the Si-SiO_2-interface region is not in steady-state conditions and that the time to reach steady-state conditions depends on humidity: It is about two orders of magnitude shorter for high compared to low relative humidity. In this paper we extend these measurements to a sensor irradiated to an X-ray dose of 1 MGy.

The cause of the time and humidity dependence for the non-irradiated sensor was explained by the time dependence of the electric boundary conditions on the surface of the sensor: Changing the bias voltage results in surface fields which cause a redistribution of surface charges until a uniform potential is reached. The strong dependence of the surface resistance on humidity [59] is responsible for the big difference in time constants.

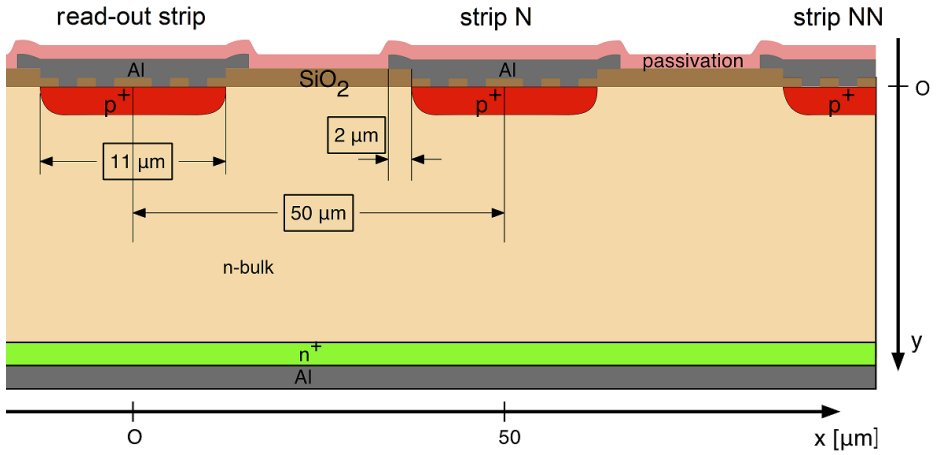

Figure 4.17: Schematic layout of the strip region of the DC-coupled Hamamatsu p^+n sensor, and coordinate definition (used in Section 4.3). The drawing is not to scale.

For given densities of oxide charges and charged interface traps, the electric boundary conditions on the sensor surface strongly influence the formation of accumulation layers and of the electrical fields close to the Si-SiO$_2$ interface. As the surface boundary conditions can influence the breakdown voltage [49, 62], their knowledge is highly relevant for the simulation of segmented silicon sensors [50], in particular for high X-ray doses and operation in vacuum.

4.3.2 Investigated sensor and measurement technique

A DC-coupled p^+n strip sensor produced by Hamamatsu Photonics [44] was investigated. Previous studies of the sensor are reported in Ref. [41, 18]. The cross section of the sensor is shown in Figure 4.17 and relevant sensor parameters are listed in Table 4.1. Measurements were performed before and after irradiation to a dose of 1 MGy (SiO$_2$) by ∼12 keV X-rays. All measurements were taken at 200 V bias voltage, well above the depletion voltage of 155 V.

Pulsed focussed red laser light with a wavelength of 660 nm was used to generate electron-hole (eh) pairs in the sensor at the p^+-strip side, just below the SiO$_2$ separating the read-out strips. Its penetrations depth in silicon is about 3.5 µm at room temperature. Hence, the charges were generated close to the Si-SiO$_2$ interface. The light was focussed to a Gaussian with $\sigma \approx 3$ µm. The pulses had a duration of 100 ps at FWHM, the number of generated eh pairs was about 100 000, and the repetition rate 1 kHz.

The current signals induced in the read-out strip were read out by DC-coupled Femto HSA-X-2-40 current amplifiers (∼50 Ω input impedance, 180 ps rise time) connected to a Tektronix digital oscilloscope with 2.5 GHz bandwidth (DPO 7254). Neighbouring strips were grounded via 50 Ω resistors. The charge Q_i on induced read-out strip i was calculated off-line by integrating the current signal over 16 ns.

The humidity during the measurements was varied between ≤ 1 % and ∼85 %, and the temperature was ∼24 °C. Humidity and temperature were logged with a TFD128 temperature

and humidity data logger. Some earlier measurements were done without data logger, and only approximate values of the humidity are known.

4.3.3 Determination of charge losses

This chapter presents the method used to determine the charge losses and shows evidence that in the p^+n-strip sensor investigated, depending on the biasing history, humidity and X-ray dose, situations without charge losses, with electron losses and with hole losses close to the Si-SiO_2-interface have been observed.

The electrons and holes generated by the laser drift in the electric field in the sensor thereby inducing currents in the electrodes. The current induced in electrode i by a charge q moving at position $\vec{x}$ with drift velocity $\vec{v}_{dr}$ can be calculated using the weighting potential ϕ_w^i:

$$I_i = q \cdot \vec{E}_w^i(\vec{x}) \cdot \vec{v}_{dr}(\vec{x}), \quad \vec{E}_w^i(\vec{x}) = \vec{\nabla}\phi_w^i(\vec{x}). \tag{4.1}$$

The weighting potential $\phi_w^i(\vec{x})$ is a measure of the capacitive coupling of a unit charge at position $\vec{x}$ to electrode i. It is one on electrode i, zero on all other electrodes, and between zero and one in the sensor volume. When a positive charge q moves from position $\vec{x}_0$ to electrode i, it induces a positive current with total charge $Q_i = q \cdot (1 - \phi_w^i(\vec{x}_0))$ in electrode i and negative currents with total charges $Q_j = -q \cdot \phi_w^j(\vec{x}_0)$ in all other electrodes $j \neq i$.

For a p^+n-strip sensor electrons drift to the n^+-rear contact and holes to the p^+ strips. Electrons collected at the rear contact induce positive signals in all p^+ strips. Holes however, induce a positive signal in the p^+ strip on which they are collected and negative signals in all other p^+ strips. If N_q eh pairs are generated anywhere in the sensor, and all holes are collected by strip i and all electrons by the rear contact, both electron as well as hole currents induced in strip i are positive, resulting in an induced charge $Q_i = N_q \cdot q_0$, where q_0 is the elementary charge. For strips j the currents induced by the electrons are positive and the currents induced by the holes negative, resulting in a bipolar signal of total charge $Q_j = 0$.

If not all charges are collected by the electrodes but some get stuck at position $\vec{x}_0$, the charge induced in a read-out strip RO which does not collect holes is:

$$Q_{RO} = \int I_{RO}\,\mathrm{d}t = (N_h \cdot q_0 - N_e \cdot q_0) \cdot (0 - \phi_w^{RO}(\vec{x}_0)) = (N_e - N_h) \cdot q_0 \cdot \phi_w^{RO}(\vec{x}_0), \tag{4.2}$$

where N_e is the number of electrons collected by the rear contact and N_h the number of holes collected by the strips. For full charge collection as well as for eh recombination $N_e = N_h$ and $Q_{RO} = 0$. If only electrons are lost Q_{RO} is positive and negative if only holes are lost.

In Ref. [41] it has been shown that the charge distribution on the sensor surface at the strip side influences the electric field in the sensor close to the Si-SiO_2 interface and that, depending on the biasing history and X-ray dose, situations with losses of electrons, losses of holes and no losses can be realised. This is demonstrated in Figure 4.18 (taken from Ref. [41]) which shows 3 examples of currents measured on the read-out strip RO, positioned at $x = 0$.

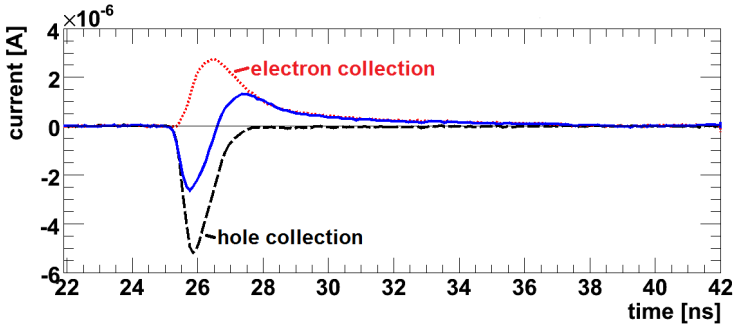

Figure 4.18: Induced current in the read-out strip at $x = 0$ for electron-hole pairs generated at $x = 30$ µm. Complete (solid line) and incomplete (dotted and dashed lines) charge collection is shown. For details see text.

For the coordinate system we refer to Figure 4.17. The sensor was biased to 200 V, well above the depletion voltage of 155 V, and the electron-hole pairs were generated by the laser at $x = 30$ µm just below the Si-SiO$_2$ interface. As this position is closer to the neighbouring strip N than to the readout strip RO, holes will only reach RO by diffusion and their number will be small.

- The solid (blue) line corresponds to the situation $e = h$, where both electrons and holes are collected (non-irradiated sensor in steady state at 200 V). Holes are collected quickly (∼2 ns) at strip N inducing a negative signal on the read-out strip RO. Electrons, which have to pass the entire sensor to reach the rear electrode, are collected more slowly (∼10 ns) inducing a positive signal in the read-out strip. Thus, the signal is bipolar and its integral is approximately zero.

- The dashed (black) line corresponds to the situation $N_e \ll N_h$, where mainly holes are collected (sensor irradiated to 1 MGy by ∼12 keV X-rays measured after ramping the voltage from 0 to 200 V in a dry atmosphere). The positive signal of the electrons is missing and only a short negative signal induced by the holes collected at the neighbouring strip N is observed.

- The dotted (red) line corresponds to the situation $e \gg h$, where mainly electrons are collected (non-irradiated sensor brought into a steady-state at 500 V and then biased at 200 V in a dry atmosphere). The negative signal of the holes is missing and only a positive current induced by electrons drifting to the rear side is observed.

The following method is used for determining the charge losses: Light is injected sufficiently far from the read-out strip RO to assure that no holes are collected by RO. For the measurements presented in the next chapter we choose RO at $x = 0$ and inject focussed light at $x_0 = 75$ µm, in the middle between two n^+ strips. To check the consistency of the results data are also taken for the light injected at $x_0 = 40$ µm. In addition, the signal from

the rear contact is recorded. Assuming that only one type of charge carrier is lost and eh recombination can be ignored, the "lost charge" is

$$Q_{lost} = (e - h) \cdot q_0 = Q_{RO}/\phi_w^{RO}(\vec{x}_0). \tag{4.3}$$

Q_{lost} is positive for hole losses and negative for electron losses. Given the quality of the bulk silicon (lifetime of the charge carriers much longer than the charge-collection time) and the fact that the sensor is operated well above the depletion voltage, charges can only be lost at the Si-SiO_2 interface or in a close-by accumulation layer. Thus the weighting potential at the Si-SiO_2 interface at the position where the eh pairs are produced is used for the analysis. Compatible with the measurements presented in Ref. [41], we use: $\phi_w^{RO} = 0.05$ at $x_0 = 75$ µm and 0.35 at $x_0 = 40$ µm.

4.3.4 Time dependence of charge losses

The measurements of the charge losses were performed for different humidities and bias histories. For the measurements the p^+ strips were grounded, either via the DC-coupled amplifiers or via 50 Ω resistors. The bias voltage was applied at the n^+ rear electrode. In Ref. [41] it has been observed for a non-irradiated sensor that, after changing the bias voltage, the distribution of surface charges is in a non-steady state, as evidenced by time dependent charge losses. It was found that the time to reach the steady state has a strong dependence on humidity. Here, we present further results on the time dependence of charge losses for the non-irradiated sensor and for the sensor irradiated to a dose of 1 MGy.

The measurement procedure was the following: By biasing the sensor either to 0 V or to 500 V (400 V for the irradiated sensor) in a humid atmosphere (> 60 % relative humidity) for at least 2 hours (typically a day and longer) steady-state conditions were assumed to have been reached. Then, for the measurements under dry conditions the relative humidity was reduced. After at least 2 hours under dry conditions, the bias voltage was changed to 200 V, the charge-loss measurements started approximately 30 seconds after 200 V had been reached, and the time dependence of the lost charges determined from measurements of Q_{RO} for eh pairs generated by the laser at position x_0.

The results for the non-irradiated sensor are shown in Figure 4.19. When changing the bias voltage from 0 to 200 V (Figure 4.19 left) initially ∼40 000 electrons are lost for both dry and humid conditions for ∼140 000 eh pairs generated by the laser. In steady-state conditions ∼10 000 holes are lost. For dry conditions (relative humidity < 1 %) steady-state conditions are reached in ∼6 hours, whereas for humid conditions (relative humidity ∼70 %) in ∼10 minutes. For comparison, also measurements for light injected at $x_0 = 40$ µm are shown. They agree with the $x_0 = 75$ µm measurements. As the weighting field at $x_0 = 40$ µm is 0.35 compared to 0.05 for $x_0 = 75$ µm, the fluctuations due to noise are about an order of magnitude smaller. However, it cannot be excluded that some of the holes reach the read-out electrode RO by diffusion. Therefore we only present results for $x_0 = 75$ µm in the following.

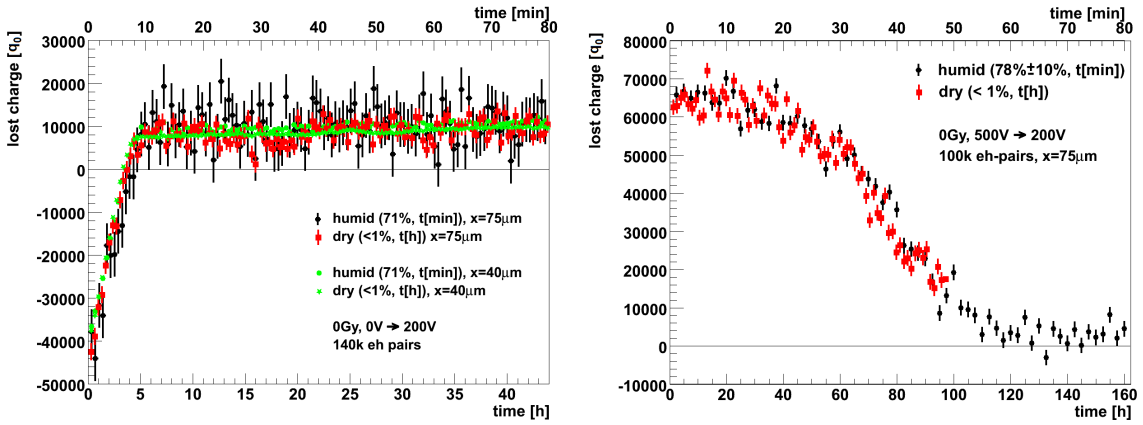

Figure 4.19: Lost charge Q_{lost}, in units of elementary charges, as a function of time after the change of the bias voltage for the non-irradiated sensor in a dry (red rectangulars) and humid (black dots) atmosphere for light injection at $x_0 = 75$ µm. Left: Increase of the bias voltage from 0 V to 200 V. The green curves show control measurements for light injection at $x_0 = 40$ µm. Right: Decrease of the bias voltage from 500 V to 200 V. Note that the time scale for "humid" is on the top and for "dry" on the bottom.

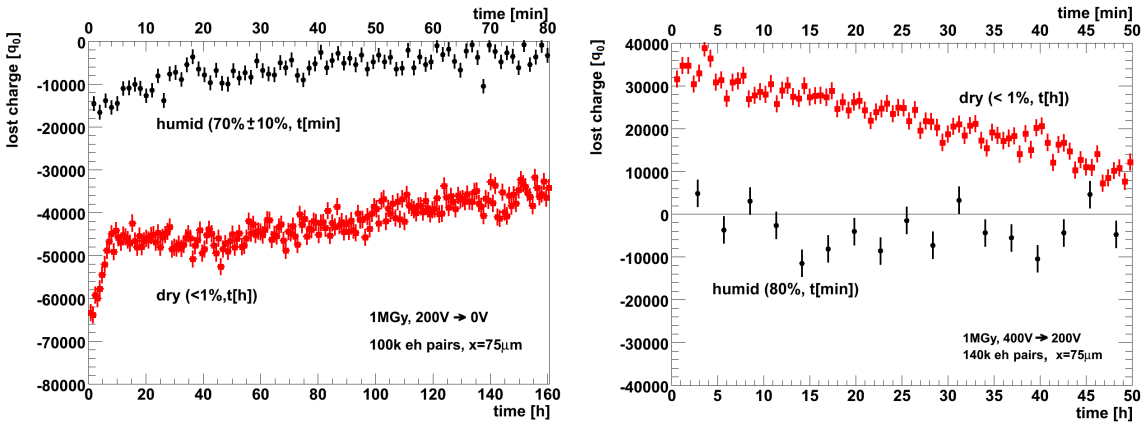

Figure 4.20: Lost charge Q_{lost}, in units of elementary charges, as a function of time after the change of the bias voltage for the irradiated sensor in a dry (red rectangulars) and humid (black dots) atmosphere. Left: Increase of the bias voltage from 0 V to 200 V. Right: Decrease of the bias voltage from 400 V to 200 V. Note that the time scale for "humid" is on the top and for "dry" on the bottom.

After changing the voltage from 500 V to 200 V (Figure 4.19 right), initially ∼65 000 holes are lost for both dry and humid conditions for ∼100 000 *eh* pairs generated. In steady-state conditions the hole losses reduce to a value between 0 and 10 000. In humid conditions it takes ∼50 minutes to reach this state, whereas in dry conditions it takes more than ∼100 hours.

We note that for dry conditions the time to reach the steady-state is about a factor 20 bigger for hole losses than for electron losses, and that the shapes of the time dependencies differ. In each case however, the shape of the time dependence for "humid" and "dry" scale. The scale factor for electron losses is ∼30. For hole losses a factor ∼120 is found, however, as the 78 % humidity had an uncertainty of ±10 % for this particular measurement, no strong conclusions can be drawn.

Figure 4.20 shows the results for the sensor irradiated to 1 MGy. After changing the voltage from 0 to 200 V electron losses are observed as for the non-irradiated sensor. The number of lost electrons however, is different for dry and humid conditions: ∼65 000 for "dry" and ∼15 000 for "humid", for ∼100 000 generated *eh* pairs. For "humid" a steady state of approximately zero electron losses is reached after about 1 hour. For "dry" the electron losses first decrease to ∼45 000 within approximately 10 hours. Then a much slower decrease is observed, reaching ∼35 000 after 160 hours when the measurements were stopped. The current collection ring of the irradiated sensor showed a large current for voltages above 400 V. Therefore, 400 V was chosen as maximum bias voltage. The initial charge losses after reducing the voltage from 400 to 200 V are approximately zero for "humid", whereas 35 000 holes are lost for "dry", for 140 000 generated *eh* pairs. As function of time the charge losses remain zero for "humid", whereas for "dry" the hole losses steadily decrease, reaching ∼10 000 after 50 hours.

We also note that the charge losses for the irradiated sensor behave quite differently compared to the irradiated sensor. For the irradiated sensor the initial losses differ between dry and humid conditions, and the time dependencies do not scale.

4.3.5 Discussion

In Ref. [41] the electron and hole losses and their time dependence have been explained with the help of detailed simulations, and their relevance for the operation of segmented p^+n sensors for the detection of X-rays and charged particles discussed: Biasing a p^+ sensor which has been in steady-state conditions at 0 V, results in a transverse electric field E_y (see Figure 4.17) in the sensor close to the Si-SiO_2 interface pointing into the sensor, and a tangential field E_x on the sensor surface pointing to the p^+ implants. The transverse field and a possible electron accumulation layer causes the loss of electrons, and the surface field causes a movement of charges on the sensor surface until the steady-state of a uniform potential is reached. For a sensor in steady state under bias, reducing the voltage results in the opposite situation: The electric field in the sensor points towards the SiO_2 and therefore holes are lost. The tangential fields initially point away from the strips until by charge movement the steady-state of a uniform potential is reached. The strong dependence of the time dependencies on humidity is

explained by the decrease of the surface resistivity with humidity [59]. If the steady state is reached due to surface currents, a scaling of the time dependence with the surface conductivity is expected.

The new measurement shown in Figure 4.19 for the non-irradiated sensor confirm the picture: Initial electron losses occur when the voltage is ramped up and hole losses when the voltage is ramped down. The initial steady-state charge losses are the same for "dry" and for "humid". The same holds for the steady-state losses. However, the time constants for reaching the steady state for hole losses is about an order of magnitude larger than for electron losses. This could be related to the surface charge distribution in steady state. We also note that in steady state a small hole loss of $\sim$5 % is observed.

The new measurements for the sensor irradiated to an X-ray dose of 1 MGy shown in Figure 4.20 are markedly different. Again, electron losses appear when the voltage is ramped up and hole losses when it is ramped down. However, the initial losses for "humid" and "dry" are very different and the time dependencies as function of humidity do not scale. In addition, the time to reach the steady-state in dry conditions are shorter for hole losses than for electron losses. We do not have explanations for these differences, but suspect that radiation induced traps in the SiO_2 and the resulting high electric fields in the SiO_2 are the cause.

4.3.6 Summary

The collection of charge carriers generated in p^+n-strip sensors close to the Si-SiO_2 interface before and after 1 MGy of X-ray irradiation has been investigated using the transient current technique with sub-nanosecond focussed light pulses of 660 nm wavelength, which has an absorption length of 3.5 µm in silicon at room temperature. Depending on the applied bias voltage, biasing history, humidity and irradiation, incomplete collection of either electrons or holes has been observed when generating the charges at the strip side of the sensor.

For the non-irradiated sensor electron losses are observed when the voltage is ramped up from zero to the operating voltage and hole losses when the operating voltage is reached from higher voltages. As a function of time the charge losses decrease until a steady state with hole losses between 0 and 10 % is reached. The shape of the time dependence and the time constant are different for hole and electron losses. At a given humidity the electron losses are about an order of magnitude faster. However, the time constants for both electron and hole losses increase by about two orders of magnitude, when the humidity is reduced from about 70 % to below 1 %. The observations are explained by changes of the charge distribution on the sensor surface. Initially, after changing the bias voltage the surface-charge distribution is not in a steady state, and the time constant to reach the steady state is related to the surface conductivity of positive and negative charge carriers, which are strong functions of humidity.

For the sensor irradiated to 1 MGy the situation is more complex: As for the non-irradiated sensor, in a dry atmosphere electron losses are observed when the operating voltage is reached from lower, and hole losses when it is reached from higher voltages. The time constant for the hole losses is similar as for the non-irradiated sensor, however, the shape of the dependence is

quite different. For electron losses a much longer time constant is found for the irradiated sensor. In a humid atmosphere already 30 seconds after the bias voltage is reached, the charge losses are small: approximately 15 % electron losses when the voltage is ramped up, and less than 10 % charge losses, when it is ramped down. We speculate that chemical effects and electric fields inside the SiO_2 and passivation layer due to charged traps are responsible for the differences.

The measurements demonstrate the well-known fact that the understanding X-ray-radiation damage in the SiO_2, at the Si-SiO_2 interface and its impact on sensor performance is highly complex.

Acknowledgements

This work was performed within the AGIPD Project which is partially supported by the XFEL-Company. We would like to thank the AGIPD colleagues for the excellent collaboration. Support was also provided by the Helmholtz Alliance “Physics at the Terascale” and the German Ministry of Science, BMBF, through the Forschungsschwerpunkt “Particle Physics with the CMS-Experiment”. J. Zhang is supported by the Marie Curie Initial Training Network “MC-PAD”.

4.4 Study of the accumulation layer using charge deposition, saturation and recovery

This section is accepted for publication in the journal Nuclear Instuments and Methods in Physics Research A with the title *Study of the accumulation layer and charge losses at the Si-SiO_2 interface in p^+n-silicon strip sensors* [43].

Abstract

Using the multi-channel Transient Current Technique the currents induced by electron-hole pairs, produced by a focussed sub-nanosecond laser of 660 nm wavelength close to the Si-SiO_2 interface of p^+n silicon strip sensors have been measured, and the charge-collection efficiency determined. The laser has been operated in burst mode, with bursts typically spaced by 1 ms, each consisting of 30 pulses separated by 50 ns. In a previous paper it has been reported that, depending on X-ray-radiation damage, biasing history and humidity, situations without charge losses, with hole losses, and with electron losses have been observed. In this paper we show for sensors before and after irradiation by X-rays to 1 MGy (SiO_2), how the charge losses change with the number of electron-hole pairs generated by each laser pulse, and the time interval between the laser pulses. This allows us to estimate how many additional charges in the accumulation layers at the Si-SiO_2 interface have to be trapped to significantly change the local electric field, as well as the time it takes that the accumulation layer and the electric field return to the steady-state situation. In addition, results are presented on the change of the pulse shape caused by the plasma effect for high charge densities deposited close to the Si-SiO_2 interface.

4.4.1 Introduction

The high instantaneous intensity and the 4.5 MHz repetition rate of the European X-Ray Free-Electron Laser (XFEL) [1, 2, 65] pose new challenges for imaging X-ray detectors [9, 66]. The specific requirements for the detectors include a dynamic range of 0 to more than 10^4 photons, with a clear separation of single photons from noise, of typically 12.4 keV per pixel for an XFEL pulse duration of less than 100 fs, and a radiation tolerance for doses up to 1 GGy (SiO_2) for three years of operation.

One question is, if all charges are collected in the 220 ns between XFEL pulses for the high instantaneous charge-carriers densities, or if pile-up effects appear. In Refs. [8, 18] the impact of the plasma effect [67], which occurs for high X-ray densities when the density of electron-hole (eh) pairs is large, typically of the order of the doping of the silicon crystal, has been studied. From these studies, it has been concluded that for 500 µm thick sensors the operating voltage should be at least 500 V in order to assure the complete signal collection in-between XFEL pulses and a sufficient narrow point spread function for the measurement of the shape of narrow Bragg peaks. The present work concentrates on the collection of

charges produced in the region below the Si-SiO$_2$ interface in segmented p^+n sensors, where the potential, under certain biasing conditions, has a saddle point and the electric field is zero. The multi-channel Transient Current Technique (m-TCT) for charges produced by a sub-nanosecond laser light of 660 nm (absorption length in silicon of about 3.5 µm at room temperature) is used for the studies.

The same study also allows a detailed investigation of the properties of the accumulation layer, which forms in segmented p^+n sensors at the Si-SiO$_2$ interface, and of the close-by electric field. This is the main topic of this manuscript.

In Ref. [41] it has been demonstrated that charge carriers produced close to the Si-SiO$_2$ interface can be lost, meaning, that they are not collected by an electrode of the sensor within $\lesssim$ 100 ns. Depending on the biasing history and on environmental parameters like humidity, situations with losses of electrons, of holes and without losses have been observed. The different situations are related to the density of oxide charges, which strongly depends on the X-ray dose with which the sensor has been irradiated, and on the potential distribution on the surface of the sensor's passivation layer, which changes when the biasing voltage is changed. Given the high surface resistivity of the passivation layer and its strong dependence on humidity, the time constants for reaching a steady-state of the surface potential can be as long as several days. As discussed in detail in Ref. [41], the cause of the charge losses is the electric field which, for an electron-accumulation layer points away from the Si-SiO$_2$ interface, and for a hole-accumulation layer towards it. In this field charge carriers drift towards the accumulation layer, and are trapped for times longer than the integration times used in the analysis of the m-TCT data.

In Ref. [42] the time dependence of the electron and hole losses close to Si-SiO$_2$ interface for an non-irradiated silicon strip sensor and a sensor irradiated by X-rays to 1 MGy (SiO$_2$) have been investigated as function of biasing history and relative humidity.

In the present work we investigate how many additional charges have to be trapped in the accumulation layers to significantly change the collection of charges from the region close to the Si-SiO$_2$ interface and thus the local electric field, and the time dependence of returning to the steady-state conditions of the accumulation layers.

The work has been done within the AGIPD collaboration [6, 7] which is developing a large-area pixel-detector system for experimentation at the European XFEL and other X-ray sources.

4.4.2 Measurement techniques and analysis

Sensors under investigation

The same DC-coupled p^+n strip sensors produced by Hamamatsu [44] as in Refs. [41, 42] were used for the investigations. Relevant sensor parameters are listed in Table 4.1, and a cross section of the sensor is shown in Figure 4.1. The sensors are covered by a passivation layer with openings at the two ends of each strip for bonding. One sensor was investigated as

produced, and another after irradiation to 1 MGy (SiO_2) with 12 keV photons and annealed for 60 minutes at 80 °C. The corresponding values for the oxide-charge density, N_{ox}, the integrated interface-trap density, N_{it}, and the surface-current density, J_{surf}, are listed in Table 4.2. The values have been derived from measurements on MOS capacitors and gate-controlled diodes fabricated on the same wafer as the sensors [31, 53, 54] and scaled to the measurement conditions.

Experimental setup

To study the charge transport and charge collection in the sensor, the instantaneous currents induced in the electrodes by the moving charges were measured (Transient Current Technique - TCT [55, 8, 18]). The multi-channel TCT setup, described in detail in [18], has been used for the measurements. The bias voltage was applied on the n^+ rear contact of the sensor. The current signal was read out on the rear contact and on 2 strips on the front side using Agilent 8496G attenuators, Femto HSA-X-2-40 current amplifiers and a Tektronix digital oscilloscope with 2.5 GHz bandwidth (DPO 7254). The readout strips were grounded through the DC-coupled amplifiers (∼50 Ω input impedance). The seven strips to the right and the seven strips to the left of the strips read out were connected to ground by 50 Ω resistors.

Electron-hole (eh) pairs were generated in the sensor close to its surface in-between the readout strips by red light from a laser focussed to an rms of 3 µm. The wavelength of the light was 660 nm, which has an absorption length in silicon at room temperature of approximately 3.5 µm. We note that 1 keV X-rays have a similar absorption length in silicon. The number of generated eh pairs was controlled by optical filters. For most of the measurements presented approximately 130 000 eh pairs were generated, corresponding to 470 X-rays of 1 keV. The laser was used in burst mode with 30 pulses per burst. The pulse structure is shown in Figure 4.21. The pulses in a burst were separated by $t_1 = 50$ ns, and the time interval between bursts $t_2 \approx 1$ ms, if not stated otherwise. To study the time dependence of the return to steady-state conditions after charges have been trapped, t_1 or t_2 were varied, with the other parameters fixed. For longer recovery times t_2 was varied between 500 ns and 10 ms and the signal from the first pulse of the burst was analysed. The recovery time Δt is defined as the time interval between the pulse analysed and its preceding pulse. Hence $\Delta t = t_2$ if the first pulse is analysed. For short recovery times t_2 was set to 1 ms, t_1 varied between 50 and

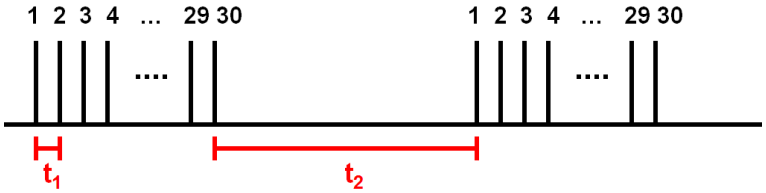

Figure 4.21: Schematic of the pulse structure. The laser was operated in burst mode with 30 pulses per burst. Pulses inside a burst were separated by the time interval t_1, and the time interval between bursts was t_2.

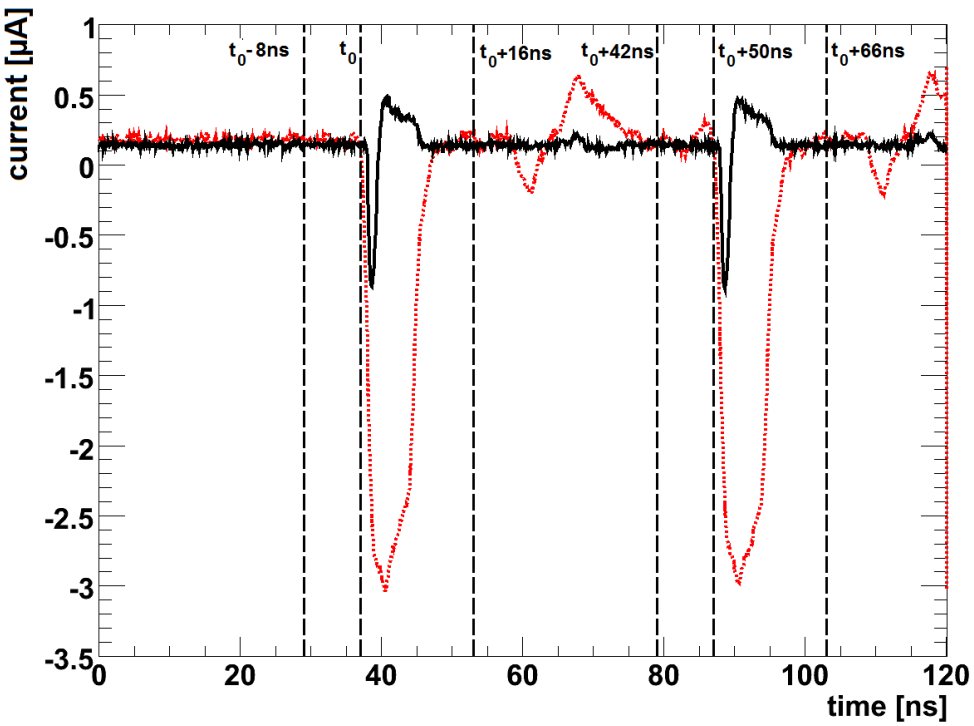

Figure 4.22: Current transients for the first two pulses of the burst for strip L (black solid line) and the rear contact (red dotted line) for 130 000 eh pairs generated at $x_0 = 75$ µm for $t_1 = 50$ ns and $t_2 = 1$ ms. The vertical lines indicate the limits used to determine the base line and the signal. The results shown are for the non-irradiated sensor in conditions "dried at 500 V" biased to 200 V.

500 ns, and the signal from pulse 30 analysed. In this case we have $\Delta t = t_1$. In this way two different measurements are available for $\Delta t = 500$ ns.

Measurement conditions

As discussed in detail in Refs. [41, 42], the observed charge losses depend on the X-ray-radiation damage and on the charge distributions inside and on top of the passivation layer. The latter changes when the biasing voltage is changed. After changing the biasing voltage, steady-state conditions are reached on top of the passivation layer after a time interval which, due to the dependence of the surface resistivity on humidity, strongly depends on the ambient relative humidity. In a dry atmosphere or in vacuum, this time can be as long as several days, whereas in a humid atmosphere, it can be as short as minutes. All measurements were performed at 200 V. The same biasing and environmental conditions were already used in Ref. [41]:

- "humid": Sensor biased to 200 V and kept in a humid atmosphere for > 2 hours (relative humidity > 60 %), i.e. in steady-state conditions on top of the passivation layer,
- "dried at 0 V": Sensor stored at 0 V for a long time to reach steady-state conditions

at 0 V, then kept in a dry atmosphere for > 1 hour (relative humidity < 5 %), and then biased to 200 V for the measurements; thus the charge distribution on top of the passivation layer corresponds to the 0 V condition,

- "dried at 500 V": Sensor kept for > 2 hours at 500 V in a humid atmosphere (relative humidity > 60 %) to reach steady-state conditions, then dried for > 1 hour, and afterwards biased at 200 V in a dry atmosphere for the measurements.

Analysis method

Figure 4.22 shows for the non-irradiated sensor biased to 200 V the current transients of the first two pulses of a pulse train measured at strip L and at the rear contact for 130 000 eh pairs generated at $x_0 = 75$ µm, half way between the readout strips R and NR, as shown in Figure 4.1. The red dotted line in Figure 4.22 shows the signal measured at the rear contact, and the black solid line the signal from strip L at $x = 0$, which is 1.5 times the strip pitch away from the position where the eh pairs were generated.

The signals are the sums of the currents induced by the holes, which drift to the p^+ strips, and the electrons, which drift to the n^+-rear contact. The holes are collected quickly, because the distance between the readout strips and the place where they were generated is small. The electron signals are significantly longer, as electrons have to traverse the entire sensor to reach the rear contact. The current transient on strip L is the sum of a short negative signal from the holes drifting to strips R and NR and a slower positive signal from the electrons drifting to the rear contact. In the rear contact the holes as well as the electrons induce negative signals. The bi-polar signals, starting approximately 20 ns after the start of the signal pulse, are due to reflections from the amplifiers, which were connected to the electrodes by 2 m long cables. The noise and the reflection for the rear contact are significantly higher than for the signal from the readout strips. This is due to the higher capacitance of the rear contact and the bias-T used to decouple the high voltage.

In the analysis the induced charge for the i-th pulse in a burst, Q_i, is calculated off-line by integrating the current over the time interval δt and subtracting the baseline current:

$$Q_i = \int_{\tau_i}^{\tau_i+\delta t} (I - I_{baseline})\,\mathrm{d}t \quad \text{with} \quad I_{baseline} = \frac{\int_{\tau_i-8\,\mathrm{ns}}^{\tau_i} I\,\mathrm{d}t}{8\,\mathrm{ns}}, \quad \text{and} \quad \tau_i = t_0 + (i-1)\cdot t_1. \tag{4.4}$$

As indicated in Figure 4.22, t_0 is the time shortly before the first pulse starts and a value $\delta t = 16$ ns was chosen for the measurements with 130 000 eh pairs. For the measurements in which the number of eh pairs was varied between 10^5 and 10^7, $\delta t = 40$ ns had to be chosen in order to collect the entire charge.

The number of charge carriers lost is obtained from Q^L, the charge induced in strip L in the following way: The integral of the hole signal is $Q_h^L = N_h \cdot q_0 \cdot (0 - \Phi_w^L(x_0))$. N_h is the number of holes collected, q_0 the elementary charge, and the term in parenthesis the difference of the weighting potential Φ_w^L for the readout strip L at the strips R and NR

where the holes are collected ($\Phi_w^L(R) = \Phi_w^L(NR) = 0$), and $\Phi_w^L(x_0)$, the weighting potential at the position x_0, where the holes were generated. The charge induced by the electrons is $Q_e^L = N_e \cdot (-q_0) \cdot (0 - \Phi_w^L(x_0))$, where N_e is the number of electrons collected at the rear contact. The total charge induced on strip L is:

$$Q^L = Q_e^L + Q_h^L = (N_e - N_h) \cdot q_0 \cdot \Phi_w^L(x_0). \tag{4.5}$$

If all holes and electrons are collected $N_e = N_h$ and $Q^L = 0$. For incomplete charge collection, assuming that there is negligible eh recombination and only electrons or only holes are lost, the amount of charge lost is given by:

$$Q_{lost} = (N_e - N_h) \cdot q_0 = Q^L / \Phi_w^L(x_0). \tag{4.6}$$

If more electrons than holes are collected $N_e > N_h$, Q_{lost} is positive, and the number of holes lost is obtained from $N_h^{lost} = Q_{lost}/q_0$. In a similar way, for $N_e < N_h$ the number of electrons lost is $N_e^{lost} = -Q_{lost}/q_0$.

In this paper measurements from strip L for light injected at the positions $x_0 = 40$ µm and $x_0 = 75$ µm are presented. For the corresponding weighting potentials $\Phi_w^L(x_0)$ values of 0.35 and 0.05 are used. For the analysis neither the signals from the rear contact nor from strip R are used, but it has been verified that the corresponding signals agree with the results of the analysis from strip L. For more details on this method of determining the charge losses and on the way the values of the weighting potentials were obtained, we refer to Ref. [41].

4.4.3 Results

The three biasing and environmental conditions under which the measurements have been performed have been defined in Section 4.4.2. First, for the non-irradiated and for the irradiated (1 MGy) sensor in the three experimental conditions it is shown how the charge losses for 130 000 eh pairs generated per pulse depend on the pulse number in the burst. Next, the time dependence of the recovery of the charge losses to the situation for the first pulse of the pulse train is investigated. Finally, for the irradiated sensor, the dependence of the charge losses on pulse number as function of the number of generated charge carriers in the range between 10^5 and 10^7 is shown. A discussion and qualitative explanations of the results are found in Section 4.4.4.

Charge losses as function of pulse number

Figures 4.23 and 4.24 show for the non-irradiated and the irradiated sensor for the three experimental conditions and ∼130 000 eh pairs generated per pulse, the fraction of charges lost as function of the pulse number in the burst. The main results are summarised in Table 4.5. The parameters of the burst mode were a time between the pulses $t_1 = 50$ ns, and a time between the bursts $t_2 = 1$ ms. As will be shown later the value $t_2 = 1$ ms is sufficient that the

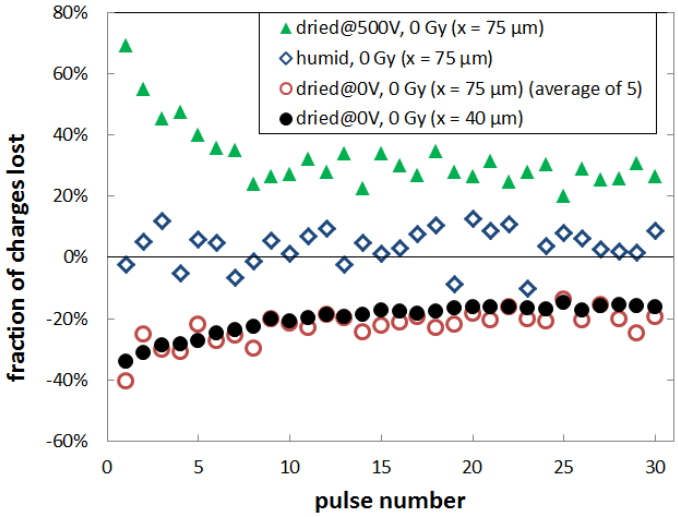

Figure 4.23: Fraction of charges lost as a function of pulse number in the burst for the non-irradiated sensor for ∼130 000 eh pairs generated per pulse at $x_0 = 75$ µm. In addition, some measurements with the laser at $x_0 = 40$ µm are shown. The sensor was biased at 200 V. The nomenclature characterizing the different measurement conditions are explained in the text. Positive values correspond to hole losses and negative to electron losses.

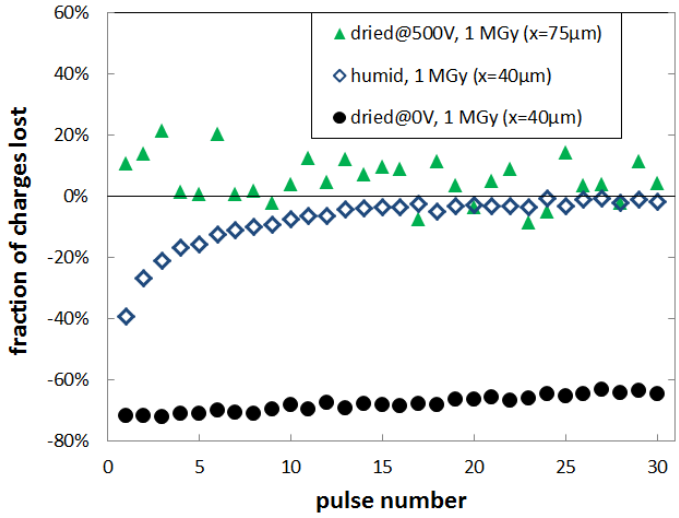

Figure 4.24: Fraction of charges lost as a function of pulse number for the irradiated sensor (1MGy). The other conditions are the same as for Figure 4.23.

condition	carrier type	pulse 1 losses	saturation losses	pulse no. saturation	no. charges lost for saturation
0 Gy, dried@500 V	h	70 %	25 %	∼8	∼500 000
0 Gy, humid	–	< 10 %	< 10 %	–	–
0 Gy, dried@0 V	e	35 %	20 %	∼8	∼300 000
1 MGy, dried@500 V	–	< 20 %	< 20 %	–	–
1 MGy, humid	e	40 %	< 5 %	∼15	∼250 000
1 MGy, dried@0 V	e	70 %	-	> 30	> 2 500 000

Table 4.5: Summary on the dependence of the charge losses on pulse number for 130 000 eh pairs produced, extracted from Figures 4.23 and 4.24. Presented are, for the non-irradiated and the irradiated sensor and three measurement conditions, the type of charge carriers lost, the initial losses for pulse number one, the saturation value of the charge losses, the pulse number at which the losses reach saturation, and the total number of charges lost until the saturation is reached.

charge losses have recovered to the steady-state values before the first pulse of the following burst.

In Figure 4.23 the fractions of charges lost for the two laser positions, $x_0 = 40$ µm and $x_0 = 75$ µm, for the condition "dried at 0 V" are shown. It can be seen, that the fluctuations for $x_0 = 40$ µm are much smaller than for $x_0 = 75$ µm. The reason is the difference in weighting potential, which is in the denominator in Equation (4.6). It is 0.35 for $x_0 = 40$ µm and 0.05 for $x_0 = 75$ µm. However, $x_0 = 40$ µm is only 15 µm away from the center between the strips R and L, and not for all conditions it can be assured, that no holes reach the readout strip L by diffusion, which is assumed in the analysis. In Ref. [41] it has been shown that there are situations where the diffusion of the holes is sufficiently small, so that the measurements at $x_0 = 40$ µm give reliable results for the charge losses. This is the case for "dried at 0 V", and the results are compatible with the measurements at $x_0 = 75$ µm. In the following, if no holes diffuse to strip L the results for $x_0 = 40$ µm are shown, else the results for $x_0 = 75$ µm.

Charge losses as function of recovery time

Figures 4.25 and 4.26 show the fraction of charges lost as a function of the recovery time Δt, defined in Section 4.4.2, for the irradiated and non-irradiated sensor biased at 200 V and ∼130 000 eh pairs generated. For the measurements at $\Delta t = 500$ ns there are two data points. As discussed in Section 4.4.2, one is obtained from pulse number 30 for the laser timing $t_1 = 500$ ns and $t_2 = 1$ ms, the other from pulse number 1 for the timing $t_1 = 50$ ns and $t_2 = 500$ ns. It is seen that the values are compatible. Smooth transitions from the reduced charge losses at short recovery times to the larger steady-state losses, corresponding to the losses for the first pulse in Figures 4.23 and 4.24, are observed.

In order to obtain a quantitative description of the measurements, they are fitted by the

phenomenological function

$$f_{lost}(\Delta t) = f_{lost}^{\infty}\left(1 - e^{-(\Delta t/t_0)^p}\right), \tag{4.7}$$

with the free parameters, the steady-state fraction of charges lost, f_{lost}^{∞}, the time constant, t_0, and the power in the exponent, p. The fit results are presented in Table 4.6. The discussion of the results is postponed to Section 4.4.4.

Effects of high charge densities

For the study of one consequence of the plasma effect, the increase of the pulse length, Figure 4.27 shows the current transients of the first two pulses of the pulse train for the

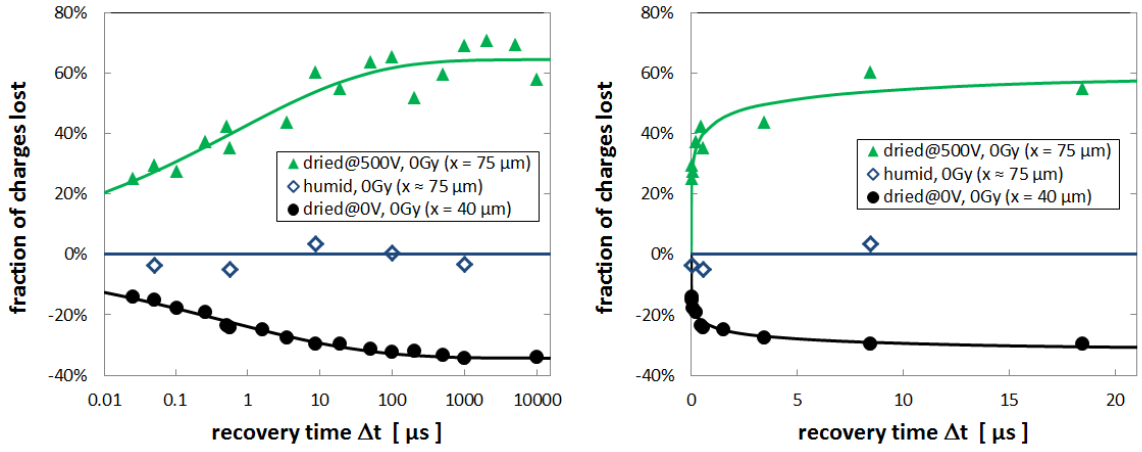

Figure 4.25: Fraction of charges lost as a function of the recovery time Δt for the non-irradiated sensor biased at 200 V for ∼130 000 eh pairs generated. Left: Logarithmic time axis. Right: Linear time axis.

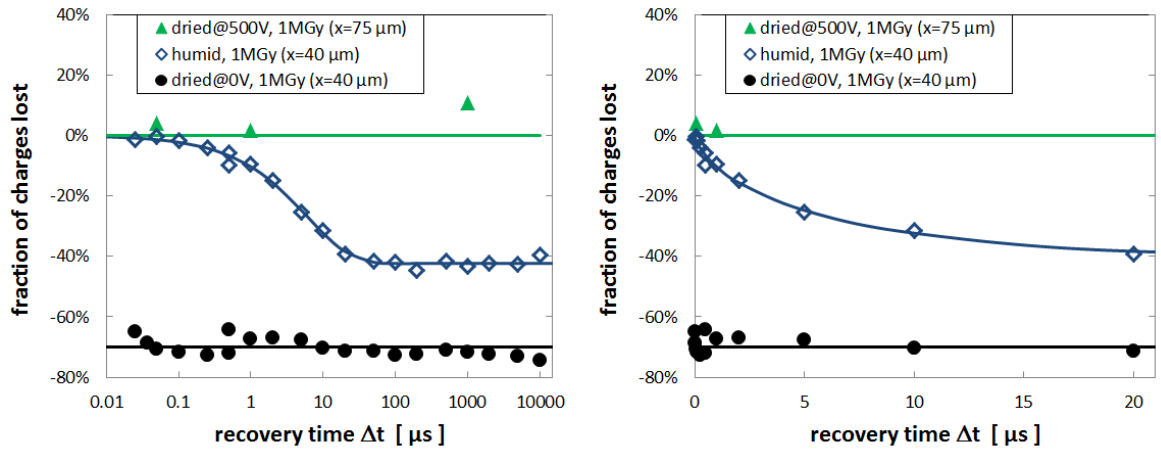

Figure 4.26: Fraction of charges lost as a function of the recovery time Δt for the irradiated sensor biased at 200 V for ∼130 000 eh pairs generated. Left: Logarithmic time axis. Right: Linear time axis.

condition	type	f_{lost}^{∞}[%]	t_0 [µs]	p
0 Gy, dried@500 V	h	64.2 ± 1.8	$0.65^{+0.57}_{-0.26}$	0.23 ± 0.06
0 Gy, humid	–	< 10	–	–
0 Gy, dried@0 V	e	-34.3 ± 0.3	$0.42^{+0.06}_{-0.05}$	0.21 ± 0.013
1 MGy, dried@500 V	–	< 20	–	–
1 MGy, humid	e	-45.6 ± 0.5	6.0 ± 0.4	$0.71^{+0.05}_{-0.03}$
1 MGy, dried@0 V	e	$\sim$73	–	–

Table 4.6: Summary of the dependence of the charge losses on recovery time Δt for 130 000 eh pairs produced, extracted from Figures 4.25 and 4.26. Presented are, for the irradiated and non-irradiated sensor and three measurement conditions, the type of charge carriers lost, and the parameters obtained when fitting Equation (4.7) to the data; the steady-state fraction of charges lost, f_{lost}^{∞}, the time constant, t_0, and the power in the exponent, p. In three cases no or little dependence on recovery time is found and the data described by a constant.

readout strip L and the rear contact, for 10^5, $3.6 \cdot 10^5$, $3.6 \cdot 10^6$ and 10^7 eh pairs produced at $x_0 = 75$ µm for the irradiated sensor biased to 200 V in the condition "dried at 0 V". We note that the condition "dried at 0 V" corresponds to operation conditions typical for sensors.

Whereas the shapes of the signals from the rear contact (red dotted lines), which are mainly due to the electrons, are similar for 10^5 and $3.6 \cdot 10^5$ eh pairs, a significant change is observed for higher intensities. The signal peaks at $\sim$10 ns, compared to $\sim$2 ns, and the signal extends up to $\sim$35 ns compared to $\lesssim$ 20 ns. Also the signals from strip L (black solid lines) change significantly. The short negative signals due to the holes moving to strips R and NR and the slower positive signals are very much reduced when normalised to the number of eh pairs generated. The reason is that both electrons and holes are trapped in the eh plasma, which dissolves by ambipolar diffusion, and the positive electron signal is to a good extent compensated by the negative signal induced by the holes moving towards strips R and NR.

Next we have investigated for the irradiated sensor in the condition "dried at 0 V", where electron losses of $\sim$70 % with little dependence on pulse number and recovery time had been observed, how the number of generated eh pairs influences the charge losses as function of pulse number. The laser was used in burst mode with 30 pulses with the parameters $t_1 = 50$ ns and $t_2 = 1$ ms, and the number of eh pairs generated at $x_0 = 40$ µm was varied between 10^5 and 10^7. In order to take into account the increase of the pulse length due to the plasma effect, for this analysis the integration time δt in Equation (4.4) was increased to 40 ns, as indicated in Figure 4.27.

Figure 4.28 shows the fraction of electrons lost as function of the pulse number for different numbers of eh pairs generated per pulse. For 10^5 eh pairs the number of electrons lost per pulse decreases with pulse number from $\sim$70 % to $\sim$60 % without reaching a constant value up to 30 pulses. This is similar to the data presented in Figure 4.24. For higher numbers of generated eh pairs, the fraction of electrons lost for the first pulse decreases, and a strong

further decrease is observed for the following pulses. The values at high pulse numbers also decrease with the numbers of generated *eh* pairs. For $3.6 \cdot 10^5$ a saturation value of ∼30 % is obtained. For 10^7 it is as small as ∼2 %. The observation that the fraction of electrons lost decreases with increasing number of generated *eh* pairs already for the first pulse agrees with the expectation, that the local electric field changes already before the charges from that particular pulse are collected.

4.4.4 Discussion

Plasma effect

With respect to the questions, if there are pile-up effects due to charges trapped in the region below the Si-SiO_2 interface, we conclude from Figure 4.27, that a significant lengthening of

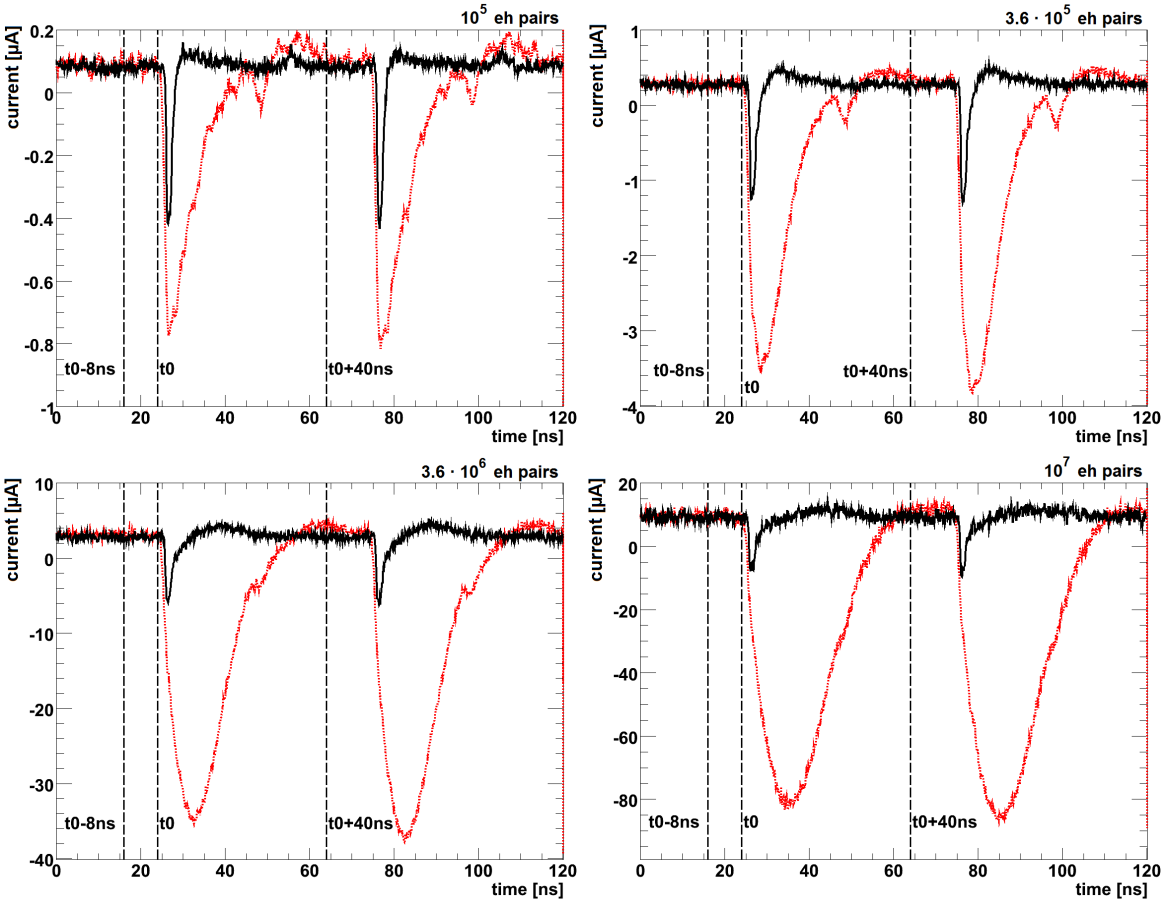

Figure 4.27: Current transients for the first two pulses of the pulse train for strip L (black solid line) and the rear contact (red dotted line) as function of the number of *eh* pairs produced at $x_0 = 75$ µm for $t_1 = 50$ ns and $t_2 = 1$ ms. The vertical lines indicate the limits used to determine the base line ($t_0 - 8$ ns to t_0) and the signal (t_0 to $t_0 + 40$ ns). The measurements were made with the irradiated sensor in the condition "dried at 0 V" biased to 200 V. Top left: 10^5 *eh* pairs. Top right: $3.6 \cdot 10^5$ *eh* pairs. Bottom left: $3.6 \cdot 10^6$ *eh* pairs. Bottom right: 10^7 *eh* pairs.

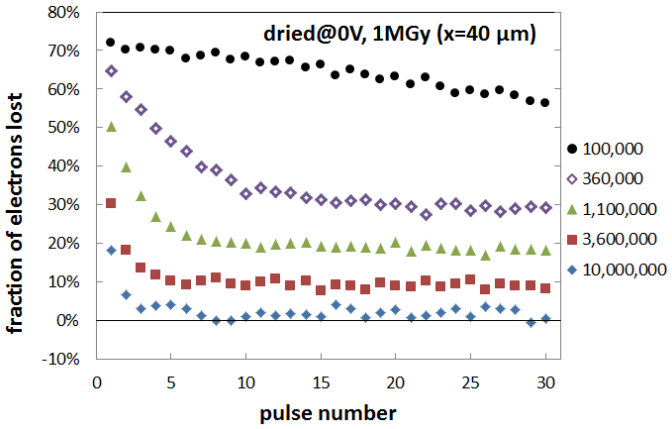

Figure 4.28: Fraction of electrons lost as a function of the pulse number in the burst for the irradiated sensor biased at 200 V for the condition "dried at 0 V". Between 10^5 and 10^7 *eh* pairs per pulse were generated at $x_0 = 40$ µm with pulse spacing $t_1 = 50$ ns and burst spacing $t_2 = 1$ ms.

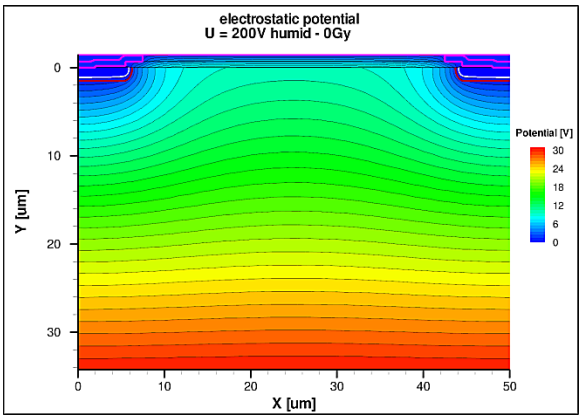

Figure 4.29: Simulated potential distribution for the non-irradiated sensor biased to 200 V with the biasing condition "humid". See Figure 4.1 for the coordinate system.

the current pulse occurs only when more than $3.6 \cdot 10^5$ *eh* pairs are produced by the laser. For the AGIPD sensor the X-rays enter through the n^+ rear contact, and only ∼0.3 % of 12.4 keV X-rays (absorption length ∼250 µm in silicon) interact in the ∼5 µm close to the Si-SiO$_2$ interface, and thus ∼3.6·10^4 12.4 keV X-rays are required to produce $3.6 \cdot 10^5$ *eh* pairs there. We conclude, that the low-field region close to the Si-SiO$_2$ interface does not result in increased pulse lengths due to the plasma effect for the situation expected at the European XFEL, and that the conclusions of Ref. [8] remain valid.

Explanation of the charge losses

A detailed discussion and an explanation of the dependence of the charge losses on X-ray dose and biasing history has been presented in Ref. [41]. It is briefly summarised here. Figure 4.29, taken from Ref. [41], shows the simulated potential distribution for "humid", the situation

where no charge losses are observed. In the calculations a positive oxide-charge density of 10^{11} cm^{-2} for a non-irradiated sensor has been assumed. At the Si-SiO_2 interface the potential has a parabolic shape in the x direction, with a maximum value of ∼10 V in the center between the p^+ strips. In the y direction the potential increases. Thus, for eh pairs produced by the laser close to the interface, the electrons drift in the y direction to the rear contact, the holes along the x direction to the p^+ strips, and no charges are lost.

The simulated potential for the condition "dried at 0 V", where electrons are lost, is shown on the left of Figure 4.30, again taken from Ref. [41]. For this condition the charge on top of the SiO_2 layer remains approximately zero, as it has been for the sensor at zero volt in steady-state conditions. The positive oxide charges cause an electron-accumulation layer at the Si-SiO_2 interface at a value of the potential of ∼29 V, a saddle point of the potential ∼5 µm below the interface, and an electric field pointing from the SiO_2 into the silicon. Thus electrons drift towards the Si-SiO_2 interface where they are lost, i.e. not collected in the time interval during which the induced current is integrated.

The right side of Figure 4.30 shows the potential for the condition "dried at 500 V". In the humid steady-state condition at 500 V negative charges accumulate on top of the SiO_2. When the voltage is reduced to 200 V in dry conditions, the negative surface charges remain, overcompensate the positive oxide charges, produce a hole-accumulation layer at a potential value of ∼4 V at the Si-SiO_2 interface and an electric field which points from the silicon into the SiO_2. Thus holes drift to the Si-SiO_2 interface and are lost.

Explanation of the change of the charge losses

Next we give a qualitative explanation of the change of the charge losses as function of pulse number and recovery time for the non-irradiated sensor.

As seen in Figures 4.23 and 4.25, if no charges are lost, i.e. all charges are collected before the next laser pulse arrives, the charge losses remain zero. This is expected, as the conditions

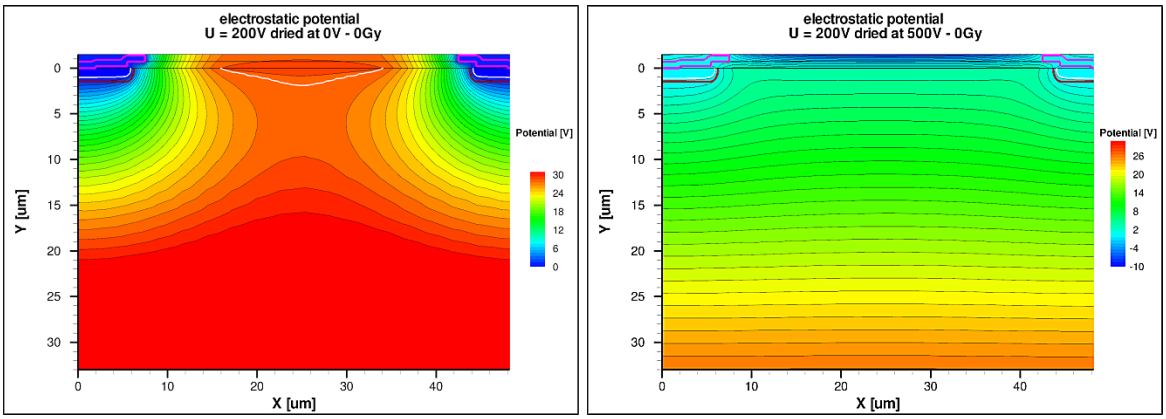

Figure 4.30: Simulated potential distributions for the non-irradiated sensor biased to 200 V for different biasing conditions. Left: "dried at 0 V". Right: "dried at 500 V". See Figure 4.1 for the coordinate system.

do not change from pulse to pulse.

If, as for the situation "dried at 500 V", positive charges are trapped close to the interface, the value of the potential at the interface in-between the p^+ strips will increase and approach the no-charge-loss situation shown in Figure 4.29. As summarised in Table 4.5, after ∼8 pulses of ∼130 000 eh pairs spaced by 50 ns, the initial hole losses of ∼70 % have decreased to a saturation value of ∼25 %. We conclude that after ∼8 pulses, the additionally trapped charges move away from the position where they were produced in the 50 ns time interval between the laser pulses. For the recovery of the charge losses Figure 4.25 shows a fast increase in the first few microseconds, followed by a much slower increase. The full recovery is reached at $\Delta t \approx 500$ µs. We assume that the recovery is due to the diffusion of the excess holes over the potential barrier.

Qualitatively the observations for the electron and for the hole losses are similar. The main difference is that the initial losses are ∼35 % for electrons, compared to ∼70 % for holes. Comparing the potential distributions shown in Figure 4.30, bigger charge losses are expected for holes than for electrons. The electric field responsible for hole trapping (right) is higher and extends over a larger region than the one for electron trapping (left). As in the case of hole trapping, trapped electrons change the potential towards the zero-loss situation. However, trapped electrons reduce the value of the potential at the interface, whereas trapped holes increase it.

Next we discuss the results for the irradiated sensor. The X-ray irradiation to 1 MGy increases the oxide-charge and interface-trap densities to an effective positive oxide-charge density of $\sim 2 \cdot 10^{12}$ cm^{-2} [31]. In addition, the surface current increases by several orders of magnitude due to the interface states.

Figure 4.24 shows, that for the condition "dried at 500 V" no charge losses are observed when ∼130 000 eh pairs are generated per pulse. Apparently the negative surface charges on top of the passivation layer compensate the high effective oxide-charge density. For "humid" the density of negative surface charges is smaller, and does not fully compensate the positive oxide charges, and electron losses of ∼40 % for the first pulse are observed. For "dried at 0 V" the surface-charge density is essentially zero, resulting in even higher electron losses of ∼70 % for the first pulse.

The electron losses as a function of pulse number for the irradiated sensor behave quite differently than for the non-irradiated sensor. For "humid" and 130 000 eh pairs generated per pulse, the electron losses decrease to essentially zero after ∼15 pulses, whereas for "dried at 0 V" they hardly decrease and show no sign of saturation. As seen in Figure 4.28, a much higher number of eh pairs is required for the irradiated sensor in the condition "dried at 0 V" to significantly change the electron losses. Also the shape of the recovery of the electron losses, shown in Figure 4.26 for the irradiated sensor in conditions "humid", is different. Whereas for the non-irradiated sensor an initial partial recovery with time constants of less than 1 µs is followed by a slow full recovery until ∼200 µs, the electron losses for the irradiated sensor recover with a single time constant of ∼6 µs. We note, that in the discription by Equation

(4.7), $p \approx 1$ we interprete as a single time constant, and $p < 1$ we interprete as a recovery with both, slower and faster components (compare Figures 4.25 and 4.26).

We finally comment, that we have made no attempt to simulate the dependence of the charge losses for the pulse structure used in the experiments. Given that it is a 3-D problem with charges spreading over large distances in-between the p^+ strips, a realistic simulation appeared out of reach.

Discussion of charge losses for high intensities

To further study the dependence of the electron losses on pulse number for the irradiated sensor in the condition "dried at 0 V", the number of eh pairs generated per pulse was varied between 10^5 and 10^7. The results are shown in Figure 4.28. It is observed that the fraction of electrons lost for the first pulse decreases from ∼70 % for 10^5 to ∼20 % for 10^7 eh pairs. The explanation for this dependence is, that the charges deposited in a given pulse already change the local electric field, and thus already influence the charge collection for this first pulse. It is also observed that for $\gtrsim 3.6 \cdot 10^5$ eh pairs generated, the electron losses saturate for higher pulse numbers. The saturation value decreases from ∼30 % for $3.6 \cdot 10^5$ to ∼2 % for 10^7. We interpret this as evidence, that for the high radiation-induced effective oxide charge density and essentially zero negative charge on top of the SiO_2 layer, the maximum value of the potential at the Si-SiO_2 interface is high and many electrons have to be trapped to significantly reduce the electron losses. From the decrease of the charge losses for the first pulse with eh intensity, we estimate that of the order of 10^6 electrons have to be trapped locally in order to reduce the electron losses by about a factor 2. This number is significantly higher than for the irradiated sensor in conditions "humid", where already electron losses of $\sim 10^5$ make a significant difference, or for the electron and hole losses for the non-irradiated sensor.

4.4.5 Summary

Using the multi-channel Transient Current Technique, the currents induced by electron-hole pairs, produced by a focussed sub-nanosecond laser of 660 nm wavelength close to the Si-SiO_2 interface of p^+n-silicon strip sensors, have been measured, and charge-collection efficiencies determined. Sensors, before and after irradiation by 1 MGy (SiO_2) X-rays, have been investigated.

For high densities of electron-hole pairs deposited close to the Si-SiO_2 interface the plasma effect results in a significant increase in pulse length. However, the number of X-rays required to generate charge densities in this region so that these effects become significant are too high, to be of relevance for the AGIPD detector at the European XFEL.

As already reported previously, dependent on radiation dose and biasing history, not all electrons or holes are collected at the contacts of the sensors within the typical readout integration times of order $\lesssim 100$ ns, but are trapped close to the Si-SiO_2 interface. These lost

charges result in a non-steady state of the accumulation layers and the nearby electric fields, which causes a reduction of the charge losses. The number of trapped charges required to significantly reduce further charge losses and possibly reach constant values, varies between $\sim 10^5$ and $\sim 10^6$ in the investigated cases. The recovery times to steady-state conditions depend on the X-ray dose with which the sensor had been irradiated.

Qualitative explanations of the findings have been given. Even if the results presented may be of limited practical relevance for the user of silicon sensors, they provide further insight into the complexities of the Si-SiO$_2$-interface region of segmented p^+n-silicon sensors.

Acknowledgements

This work was performed within the AGIPD Project which is partially supported by the European XFEL-Company. We would like to thank the AGIPD colleagues for the excellent collaboration. Support was also provided by the Helmholtz Alliance “Physics at the Terascale”, and the German Ministry of Science, BMBF, through the Forschungsschwerpunkt “Particle Physics with the CMS-Experiment”. J. Zhang was supported by the Marie Curie Initial Training Network “MC-PAD”.

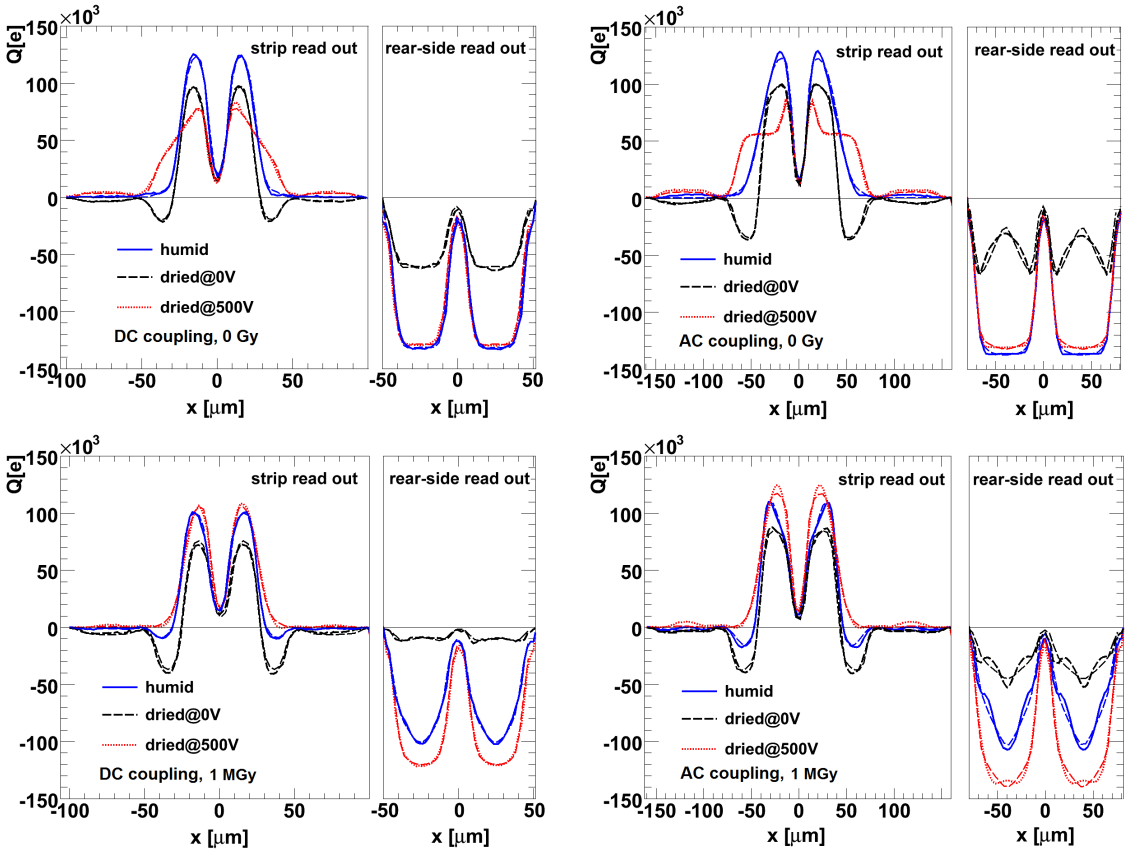

Figure 4.31: Strip and rear-side signals as a function of the light-spot position, x, for the data (thick lines, see legend) and the model calculation (thin dashed lines, same color). Left: DC-coupled sensor with a pitch of 50 µm produced by Hamamatsu, Right: AC-coupled sensor with a pitch of 80 µm produced by CiS. Top: non-irradiated. Bottom: after 12 keV x-ray irradiation to a dose of 1 MGy. Strip L, which is located at x=0 µm, is used for the strip read out. The shown x range is also the range over which the fit is performed. The chosen x range for read-out strip L from −100 µm to +100 µm (−160 µm to +160 µm for the AC-coupled sensor) is equivalent to a range from 0 to 50 µm (0 to 80 µm) for four read-out strips NR, R, L, and NL (see Figure 4.1 for coordinate system).

4.5 Additional material

4.5.1 Strip and rear-side signals in data and model calculation

In Section 4.2 a model calculation is introduced to describe the integrated signals on read-out strips and on the rear-side contact as a function of position of the light spot which is used for *eh*-pair generation. A DC-coupled sensor produced by Hamamatsu [44] is used. A fit is performed and results are presented in Table 4.3. To verify that the data is described by the model calculation, the integrated signals as a function of light-spot position are compared in Figure 4.31. The data is well described by the model calculation for both strip read out and rear-side read out.

So far, measurements on a DC-coupled sensor with a pitch of 50 µm and crystal-orientation

	humid 0 Gy	dried@500 V 0 Gy	dried@0 V 0 Gy	humid 1 MGy	dried@0 V 1 MGy	dried@500 V 1 MGy
N_e^c	140 000	142 000	11 000	106 000	43 000	147 000
N_e^e	135 000	133 000	83 000	51 000	18 000	110 000
N_h	126 000	6 000	134 000	162 000	124 000	110 000
x_0	0.70 µm	0.66 µm	0.08 µm	-0.43 µm	-0.11 µm	-0.46 µm
d_{acc}	(62 µm)	39 µm	59 µm	8 µm	59 µm	(6 µm)
σ_{diff}	13.9 µm	(400 µm)	3.4 µm	6.7 µm	3.7 µm	9.2 µm

Table 4.7: Results of the fits using the model described in Section 4.2.4 for the sensor produced by CiS. Values of d_{acc} in parentheses indicate that the charge losses are insufficient for a reliable determination of the width of the accumulation layer. Values of σ_{diff} in parenthesis indicate that the number of collected holes are insufficient for a reliable determination of the hole diffusion parameter. The laser is adjusted to generate ∼140 000 eh-pairs.

<111> produced by Hamamatsu [44] have been presented. These measurements are now supplemented by measurements on an AC-coupled sensor with a pitch of 80 µm and crystal orientation <100> produced by CiS [45]. For both sensors relevant sensor parameters are listed in Table 4.1.

In order to describe the measurements of the CiS sensor, some parameters in the model calculation are adjusted. The width of the aluminium strip is increased to 16 µm and the pitch to 80 µm. The numbers for the weighting potentials in the gap centre are adjusted to $\phi_w^{0.5} = 0.4$ for the closest strips, which are 0.5 pitches away, $\phi_w^{1.5} = 0.04$ for the next strips, which are 1.5 pitches away, and $\phi_w^{Rear} = 0.06$ for the rear-side read out. The other parameters, e.g. the width of the light profile, are kept the same as for the DC-coupled sensor (see Section 4.2.2).

The fit results for the AC-coupled sensor are listed in Table 4.7 and are similar to the fit results for the DC-coupled sensor, which are shown in Table 4.3 and discussed in Section 4.2.3. A comparison of the observed charge losses for the two different sensor technologies is given in Table 4.8. Sensors are compared before and after 12 keV x-ray irradiation to a dose of 1 MGy (SiO_2), in humid atmosphere and in dry atmosphere for different biasing histories. In each condition the charge losses are similar for the two sensor technologies:

- $\lesssim$20 % charge losses are observed for "humid – 0 Gy" and "dried at 500 V – 1 MGy",
- electron losses are observed for "dried at 0 V – 0 Gy", "humid – 1 MGy" and "dried at 0 V – 1 MGy",
- hole losses are observed for "dried at 500 V – 0 Gy".

However, the amount of charge losses may be different. The biggest difference is observed for "dried at 500 V, 0 Gy", with 90 % hole losses for the AC-coupled sensor with 80 µm pitch and 55 % hole losses for the DC-coupled sensor with 50 µm pitch. Differences in charge carrier losses are connected to differences in the electrostatic potential. Possibly the difference in gap size is relevant, which is 60 µm compared to 39 µm (Table 4.1).

sensor and pitch	humid 0 Gy	dried@500 V 0 Gy	dried@0 V 0 Gy	humid 1 MGy	dried@0 V 1 MGy	dried@500 V 1 MGy
CiS 80 µm	$\lesssim$20 %	90 % h	c: 90 % e e: 40 % e	c: 30 % e e: 60 % e	c: 70 % e e: 85 % e	$\lesssim$20 %
Hamamatsu 50 µm	$\lesssim$20 %	55 % h	c: 65 % e e: 55 % e	c: 30 % e e: 50 % e	c: 100 % e e: 90 % e	$\lesssim$20 %

Table 4.8: Comparison of the main charge losses observed in the AC-coupled CiS sensor with a pitch of 80 µm and in the DC-coupled Hamamatsu sensor with a pitch of 50 µm. In the case of electron losses the upper number refers to the amount of electron losses if the charge is generated at the gap centre, and the second number refers to the amount of electron losses if the charge is generated close to the edge of the strip implant.

λ	830 nm	660 nm
N_e^c	49 000	0
N_e^e	73 000	9 400
N_h	108 000	126 000
x_0	-1.93 µm	0.77 µm
d_{acc}	34.7 µm	36 µm
σ_{diff}	1.2 µm	2.1 µm

Table 4.9: Fit results for measurements using laser light of the wavelength $\lambda = 830$ nm for the condition "dried at 0 V – 1 MGy". For comparison also the data for $\lambda = 660$ nm is given, which is taken from Table 4.3.

4.5.2 A measurement of the saddle point of the electrostatic potential

In previous sections interface charge losses are studied for charge generation using laser light with a wavelength of 660 nm. Light of this wavelength has a penetration depth of ∼3.5 µm at room temperature in silicon. The observed charge losses give insight in the electric-field direction very close to the Si-SiO_2 interface.

In this section the studies are extended to charge carrier generation using laser light with a wavelength of 830 nm, which has a penetration depth of ∼13 µm at room temperature in silicon. The measurements with 830 nm light give insight in the electric field in the bulk region between the p^+ strips, a few µm below the Si-SiO_2 interface. In the framework of this thesis only one case, the DC-coupled sensor in the condition "dried at 0 V – 1 MGy", is discussed. The condition "dried at 0 V" is typical for sensors in experiments.

Table 4.9 shows the fit results for both 830 nm light and 660 nm light. The results are similar, but less electrons are collected if the charge is generated using 660 nm light. In both cases little diffusion ($\sigma_{diff} < 3$ µm) and a large accumulation layer width ($d_{acc} > 34$ µm) are observed. Also in both cases more holes than electrons are collected. The laser intensities are not known and the number of generated eh pairs can only be estimated from the measurements. The difference in number of holes collected may be explained by ∼20 000 less eh pairs being generated with the 830 nm laser.

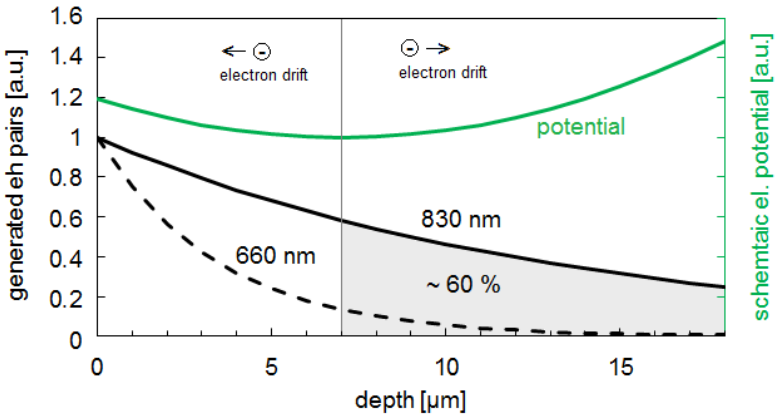

Figure 4.32: Schematic explanation for the fraction of electrons lost for *eh*-pair generation by 660 nm and by 830 nm light. An electrostatic potential with a saddle point at a depth of 7 µm below the gap centre is assumed. The gray area shows the fraction of *eh* pairs (generated by 830 nm light) for which full charge collection is expected.

The main difference is the fraction of lost electrons. For charge carriers generated very close to the Si-SiO$_2$ interface, using 660 nm light, ∼95 % of the electrons are lost. For charge carrier generation further in the bulk, using 830 nm light, only ∼30 to 50 % of the electrons are lost. For measurements using 660 nm light, electron losses are already explained in Section 4.2.4: the electrons are generated close to a potential maximum, which is located at the Si-SiO$_2$ interface (Figure 4.14), and remain at the interface during the integration time. The same explanation can be used for the loss of charge carriers generated with 830 nm light: Electrons which are generated close to the potential maximum stay at the interface. However, the electrons generated further away from the interface drift to the rear contact and are not lost.

Assuming that the collection of electrons is dominated by the local electric field, those electrons which are generated in the region with the electric field pointing away from the interface will drift to the interface and remain there. Figure 4.14 shows the simulated electrostatic potential with a saddle point at a depth of ∼7 µm for the condition "dried at 0 V – 1 MGy". For this potential, electrons are collected at the interface, if they are generated in the 7 µm deep region between saddle point and interface. Electrons which are generated outside of this region are collected at the rear-side contact and hence are not lost at the interface.

For 830 nm light ∼40 % of the electrons are generated in the first 7 µm, and for 660 nm light ∼90 % (Figure 4.32). In the measurements using 830 nm light ∼50 % electron losses are observed around the gap centre, corresponding to a saddle point in the electrostatic potential ∼9 µm below the interface. However, given the systematic uncertainties of the model calculation, the fit results are also compatible with a saddle point 7 µm below the interface. We conclude that the simulated electrostatic potential is compatible with charge-collection measurements for the state under investigation, "dried at 0 V – 1 MGy". The measurements with 830 nm light nicely confirm the interpretation of the charge losses due to the electric-field

distribution in the region close to the Si-SiO_2 interface.

4.5.3 Time development of interface charge losses as a function of humidity

In Section 4.3 the time development of interface charge losses is investigated after the bias voltage is changed. Between 100 000 and 140 000 eh pairs are generated close to the Si-SiO_2 interface using light of 660 nm wavelength. For the non-irradiated sensor the time development of charge losses is shown in Figure (4.19), and the relevant observations are summarised here:

- 0 V $\rightarrow$ 200 V: electron losses are observed directly after the bias voltage is changed. After 230 min in the case of dry atmosphere ($<$ 1 % humidity), and after 8 min, in the case of humid atmosphere ($>$ 60 % humidity), no more electron losses are observed.
- 500 V $\rightarrow$ 200 V: hole losses are observed directly after the bias voltage is changed. After 90 h in the case of dry atmosphere, and after 45 min, in the case of humid atmosphere, hole losses are reduced to 20 000.
- In both cases a steady state with $\sim$10 000 hole losses is observed.

Hence, observed time constants are approximately two orders of magnitude shorter in humid conditions compared to dry conditions.

Now measurements for the non-irradiated sensor are extended, using different humidities for both cases, 0 V $\rightarrow$ 200 V and 500 V $\rightarrow$ 200 V. Results are summarised in Table 4.10 and shown in Figure 4.33. It is found that if the time constants are compared to the time constant in a dry atmosphere ($time_{relative} = time/time_{dry}$) they can be described as a function of humidity by the same curve for 0 V $\rightarrow$ 200 V and for 500 V $\rightarrow$ 200 V (Figure 4.33).

Further the sheet resistance for different humidities, taken from Ref. [59], is shown. It is found that the humidity dependence is similar for the time constants relevant for interface charge losses, and for the sheet resistance. We conclude that the humidity dependence of the time development of interface charge losses is compatible with surface-charge transport described by the sheet resistance.

ramping	humidity	time to reach 0 electron losses	rel. time constant
0 V → 200 V	< 1 %	230 min	1
0 V → 200 V	44 to 48 %	73 min	0.32
0 V → 200 V	71 %	8 min	0.035
0 V → 200 V	83 %	1.25 min	0.005
0 V → 200 V	83 %	1 min	0.004

ramping	humidity	time to reach 20 000 hole losses	rel. time constant
500 V → 200 V	< 1 %	5400 min	1
500 V → 200 V	33 to 47 %	2400 min	0.44
500 V → 200 V	67 to 73 %	225 min	0.041
500 V → 200 V	> 60 %	45 min	0.008

Table 4.10: Time constants for different humidities. In some cases the humidity changed during the measurement and in one case the humidity was not logged.

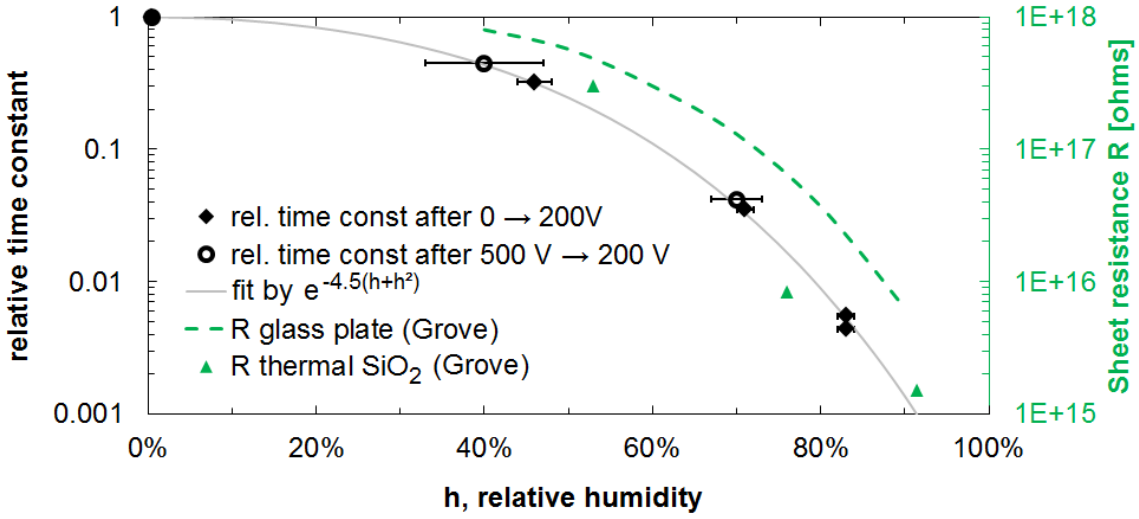

Figure 4.33: Humidity dependence of time constants relevant for interface charge losses compared to the sheet resistance. Shown time constants are taken from Table 4.10, data on the sheet resistance is taken from Ref. [59].

Chapter 5

Charge losses in the silicon bulk of pad sensors

5.1 Introduction

The Large Hadron Collider (LHC) [4] was built to uncover fundamental questions in particle physics. Protons are accelerated to a design energy of 7 TeV and are brought to collision inside of different experiments. For the two general-purpose experiments CMS [12, 13] and ATLAS [68, 69], the design luminosity is 10^{34} cm^{-2}/s. In 2011 and 2012 protons with an energy of 3.5 TeV and 4 TeV were used, and in July 2012 a new particle was observed in both general-purpose experiments [70, 71]. Up to now its features are in agreement with the standard-model Higgs boson. With increasing integrated luminosity and higher collision energies further discoveries are expected. After the LHC shutdown which is currently ongoing until 2014 proton energies of 6.5 TeV are foreseen in 2015 [72, 73]. Another LHC upgrade is foreseen in ∼2022 to increase the luminosity.

After the upgrade of the LHC to the high-luminosity LHC (HL-LHC) the design luminosity will be increased to 10^{35} cm^{-2}/s, and the detectors will experience both a higher occupancy and more radiation damage. For the silicon tracker of CMS, the increased luminosity corresponds to an integrated particle flux of about $1.5 \cdot 10^{16}$ cm^{-2} for the innermost pixel layers (10^{15} cm^{-2} for the innermost strip layers) after five years of operation [74, 75].

Radiation induced defects will alter the sensor properties. The three main consequences are:

- a change in effective doping concentration, which leads to an increase of operation voltage needed to fully deplete the sensors, or to a drop in signal if sensors cannot be fully deleted,
- an increase of the concentration of current-generation centres, which leads to an increase of dark current, power consumption, heat generation and noise,
- radiation induced defects act as trapping centres, which will lead to a signal drop due

to a delayed collection of charge carriers in respect to the integration times of typically ∼25 ns.

Silicon sensors now being used in the CMS tracker would not achieve the required performance at the high radiation fields due to significant signal reduction [76]. Sensors with improved radiation hardness must be used to provide sufficient signal to the read-out system.

In order to reduce the dark current, and consequently the power consumption and heat generation, an improved cooling system is needed. In the HL-LHC a low-mass CO_2-cooling system will be used in the CMS detector with a foreseen operating temperature of -20 °C.

Further, two different approaches are used to increase the radiation tolerance of sensors, in order to provide sufficient signal: material engineering and device engineering.

For material engineering the sensor bulk material is changed. Either silicon with a different impurity concentration is used, e.g. silicon with a high oxygen concentration, or a different material be used, like SiC, GaN or diamond [77]. Oxygen-rich silicon was observed to have less changes in the effective doping concentration compared to oxygen-lean silicon [78, 35]. As a consequence a smaller operating voltage is sufficient to fully deplete the sensors and to ensure sufficient signal at moderate voltages and power consumption.

For device engineering the sensor layout is changed. After irradiation thin sensors are known to have a higher charge-collection efficiency (CCE) than thick sensors. Due to a short collection distance, less charge losses in trapping centres occur. Additionally, full depletion is reached at lower voltages compared to thicker sensors. However, in thinner sensors less charge is generated by minimum-ionising particles (mip), and for a given fluence and a given bias voltage an optimal thickness has to be determined. The concept of 3D sensors [79, 80] combines the advantages of both thick and thin sensors. A relatively thick sensor provides a high number of generated *eh* pairs, and a short collection distance perpendicular to the particle tracks provides a high CCE and a low full-depletion voltage. However, the production of 3D sensors is more sophisticated compared to the production of planar sensors, making them an option for the innermost layers only.

In the framework of the CMS-tracker upgrade, different planar-sensor layouts and different sensor materials are tested after proton and neutron irradiation to HL-LHC fluences to find the best sensor layout and the best sensor material for the upgrade. For this effort a large amount of samples have been ordered by Hamamatsu Photonics (HPK) [44] and are measured in different institutes (CMS tracker campaign). More information on the campaign can be found in [81]. Pad sensors are used to investigate differences of silicon materials, independently of sensor-layout effects. Materials obtained with different growing methods (float zone, magnetic Czochralski and epitaxial), and of different thicknesses (100, 200 and 320 µm) are investigated. The 320 µm thick sensors underwent a deep-diffusion process to reduce the active sensor thickness by the introduction of dopants [82]. In this chapter, charge-collection measurements for 200 and 320 µm thick pad sensors of float-zone and magnetic-Czochralski silicon are reported.

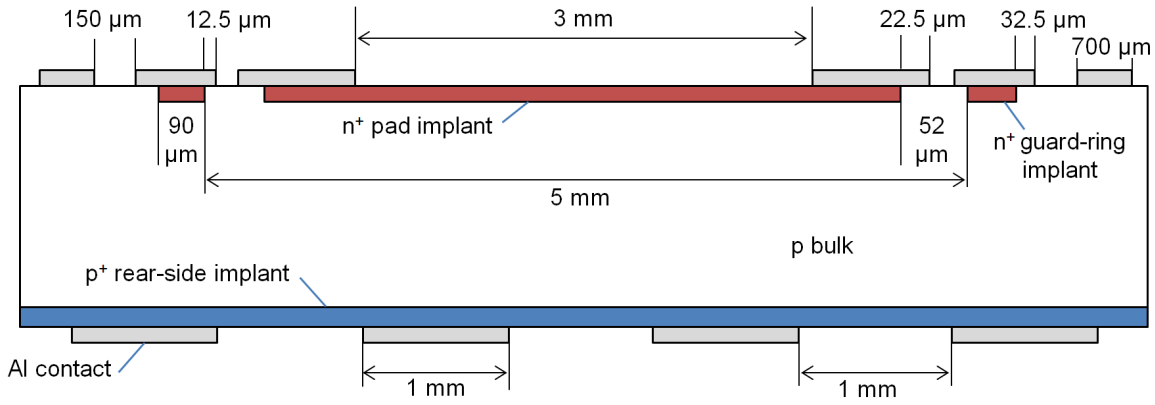

Figure 5.1: Schematic cross-section of the pad sensors used in this chapter with p-doped bulk. The drawing is not to scale.

5.2 Investigated samples

The investigated samples are part of the CMS tracker campaign and are produced by HPK. Other measurements on this material are presented in [36, 82, 83, 84].

For the pad-sensor measurements presented in this work, mainly pad sensors with an active area of ∼0.25 cm^2 (Figure 5.1) are used. Additionally, smaller sensors with a pad area of ∼0.044 cm^2 are available. If large sensors are available, they are used to determine the CCE and the active thickness. The active thickness is determined from the capacitance between the pad implant and the rear-side implant of non-irradiated sensors at ∼100 V above full depletion, assuming an effective pad area of 0.25 cm^2 for the capacitive coupling between pad and rear side. The guard ring and the pad are grounded and the high voltage is applied to the rear side of the sensor.

An overview of the used materials is given in Table 5.1. The <100> oriented silicon crystals are grown using either the float-zone method (FZ) or the magnetic-Czochralski method (MCz). Some of the FZ materials underwent a deep-diffusion process (dd-FZ) where high doping concentrations are introduced to reduce the active thickness [82]. Both n-type material (p$^+$-n-n$^+$) and p-type material (n$^+$-p-p$^+$) are used in this work. The physical thickness shown in Table 5.1 is given by the producer [44], and the oxygen content is determined in secondary ion mass spectrometry measurements (SIMS) in Warsaw [85]. The active thickness is determined for many sensors of each material and both the average value and its fluctuation is reported.

The material names used in this chapter are given in Table 5.1, and contain the growing (and thinning) method (MCz, FZ, dd-FZ), the approximate active thickness in µm (200 or 300), and the initial doping type of the silicon bulk (N for n-type or P for p-type). For the charge-collection measurements presented in this chapter, the TCT setup for pad sensors is used (Section 3.2.1).

material name	physical thickness	active thickness	oxygen content	V_{fd} before irradiation
MCZ-200N	200 µm	198 ± 9 µm	$\sim 5 \cdot 10^{17}$ cm^{-3}	150 V
MCZ-200P	200 µm	200 ± 9 µm	$\sim 5 \cdot 10^{17}$ cm^{-3}	100 V
FZ-200N	200 µm	202 ± 3 µm	unknown	90 V
FZ-200P	200 µm	199 ± 7 µm	unknown	120 V
dd-FZ-300N	320 µm	296 ± 6 µm	$\sim 1 \cdot 10^{17}$ cm^{-3}	190 V
dd-FZ-300P	320 µm	287 ± 12 µm	$\sim 1 \cdot 10^{17}$ cm^{-3}	230 V
dd-FZ-200N	320 µm	216 ± 9 µm	$\sim 3 \cdot 10^{17}$ cm^{-3}	100 V
dd-FZ-200P	320 µm	205 ± 5 µm	$\sim 3 \cdot 10^{17}$ cm^{-3}	90 V

Table 5.1: Overview of the materials investigated in this chapter. Details see text.

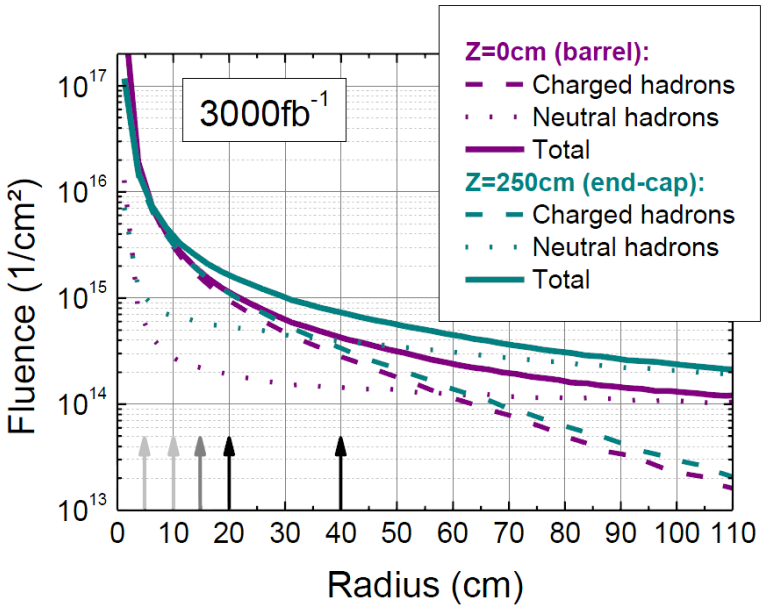

Figure 5.2: Expected HL-LHC fluences after 3000 fb^{-1} at different positions in the CMS tracker according to [74, 75], taken from [83]. The arrows show the radii for which the corresponding fluences are investigated.

5.3 Irradiations

Irradiations are performed to simulate the expected radiation damage in silicon sensors at different positions in the CMS tracker for HL-LHC fluences. FLUKA simulations [86, 87] are used to predict fluences of charged and neutral hadrons at different positions in the CMS tracker after the phase-2 upgrade and an integrated luminosity of 3000 fb^{-1}. The simulations are performed within the CMS collaboration and will be reported in Ref. [74, 75]. Based on the simulated particle fluences which are shown in Figure 5.2 fluences are chosen for the irradiation program.

Either reactor neutrons, protons of different energies, or a mixture of 23 MeV protons and reactor neutrons are used for the irradiation.

particle type	neq fluences [10^{14} neq/cm^2]	irradiated materials
protons (23 MeV)	2.9, 10	dd-FZ, MCz
reactor neutrons	4	dd-FZ, MCz
protons (23 MeV) + neutrons	6.9 (2.9+4), 15 (10+5)	dd-FZ, MCz
protons (23 GeV)	2.87, 10.8, 15.9, 29.4, 131	MCz, FZ

Table 5.2: Irradiations performed on samples studied in this chapter. There is a 10 percent uncertainty on all fluences.

Neutrons Irradiations with reactor neutrons are performed at the research reactor of the Jozef Stefan Institute in Ljubljana [88]. Neutron fluences of $4 \cdot 10^{14}$ cm^{-2} and $5 \cdot 10^{14}$ cm^{-2}, with a mean neutron energy of ∼1 MeV, have been achieved. The irradiation time is ∼4 and ∼5 minutes respectively, and is performed at a room temperature of about 25 °C. After irradiation the sensors are kept cool to avoid annealing.

23 MeV protons 23 MeV proton irradiations are performed at the ZAG Zyklotron AG in Karlsruhe [89]. Fluences of $3 \cdot 10^{14}$ neq/cm^2 and $1 \cdot 10^{15}$ neq/cm^2 have been achieved. The samples are cooled during and after irradiation to avoid annealing.

23 GeV protons 23 GeV proton irradiations are performed at the Proton Synchrotron (PS) at CERN. Fluences between $3 \cdot 10^{14}$ neq/cm^2 and $1.3 \cdot 10^{16}$ neq/cm^2 have been achieved. The samples are not cooled during irradiation but kept at about 30 °C. For the higher fluences the irradiation time is several weeks and annealing during irradiation must be taken into account. Scaled to a temperature of 60 °C, effective annealing times during irradiation are between ∼10 and ∼75 min at 60 °C. Measurements on sensors after 23 GeV proton irradiation presented in this work are done as irradiated, i.e. without any additional annealing.

Mixed irradiation Mixed irradiation is performed using 23 MeV protons and reactor neutrons. After proton irradiation the sensors are annealed for 10 min at 60 °C, capacitance, current and charge-collection measurements are performed, and afterwards the sensors are irradiated with neutrons. Fluences of $7 \cdot 10^{14}$ neq/cm^2 and $1.5 \cdot 10^{15}$ neq/cm^2 have been achieved.

Further mixed irradiations are foreseen in the framework of the HPK campaign: Irradiations with neutrons, followed by irradiations with 23 MeV protons are planned to check whether the order of irradiation is relevant. Also studies combining irradiations with 23 GeV protons and irradiations with reactor neutrons are ongoing.

Storage of irradiated samples Irradiated samples are kept cold for both storage (below -20 °C) and shipping (below 0 °C). Defect kinetics during storage and shipping are considered to be negligible compared to an annealing time of 10 min at 60 °C. If the annealing during irradiation is effectively less than 10 min at 60 °C, the sensors are annealed until the effective annealing time is 10 min at 60 °C.

Overview of irradiated materials The irradiated materials and the fluences are listed in Table 5.2. The dd-FZ materials are irradiated with 23 MeV protons, reactor neutrons and a mixture of both 23 MeV protons and reactor neutrons, but not with 23 GeV protons due to limited resources. The FZ materials are so far only investigated after 23 GeV proton irradiation, but not after irradiation with any other particle type. Up to now direct comparisons are only possible between MCz and FZ materials after 23 GeV irradiation and between MCz and dd-FZ materials after irradiation with any other particle type, but not between FZ and dd-FZ materials.

5.4 Analysis

5.4.1 Determination of the charge-collection efficiency

The CCE is determined from the ratio of collected charge of the device under test (dut) to the collected charge of a non-irradiated reference sensor:

$$CCE_{dut} = \frac{Q_{dut}}{Q_{ref}}. \tag{5.1}$$

All investigated non-irradiated sensors are fully depleted at 400 V, and Q_{ref} is taken at this voltage for a non-irradiated sensor of the same type (material, thickness and initial doping). E.g. for an irradiated 200 µm thick MCz n-type sensor a non-irradiated 200 µm thick MCz n-type sensor will be used as reference. The reference sensor is not necessarily from the same wafer as the device under test.

The uncertainty on the CCE is estimated to be 3 % (Section 3.2.4).

5.4.2 Determination of the signal for minimum-ionising particles

The most probable value (mpv) for the expected signal of a mip traversing the sensor is estimated from the measured CCE. According to the Particle Physics Booklet [15] the most probable number of eh pairs generated by a mip in a 300 µm thick silicon sensor is about 22 000. In this work the mip signal is calculated from the measured CCE and the active sensor thickness d as following:

$$Signal = CCE \cdot 22\,000 \cdot \frac{d}{300\ \mu\text{m}}. \tag{5.2}$$

5.4.3 Determination of trapping parameters

In this section two alternative ways to describe trapping in irradiated sensor are explained: the description using an effective trapping time, and the description using an effective drift distance.

Effective trapping time

A common approach to describe charge losses in silicon sensors is the use of an effective trapping time, τ. It can be extracted from time-resolved current signals if the time resolution is sufficient and if either assumptions on the drift-velocity profile, or assumptions on the trapping time are made. If τ is assumed to be a constant which is neither position nor voltage dependent, it can be determined from time-resolved charge-collection measurements using the charge correction method (CCM) [90, 91, 92]. The advantage of the CCM is that no knowledge on the CCE is required and hence no reference measurement is needed.

In the last years, different methods to extract the effective trapping time have been investigated. In Refs. [14, 19] it is shown that the assumption of an overall constant trapping time does not describe the CCE for electrons moving in highly irradiated silicon sensors. This can be seen in Figure 5.3 taken from Ref. [19]. Figure 5.3 and the model calculation used in the figure are described in detail in Ref. [19] and will be summarised here briefly. The CCE is determined experimentally for 150 µm thick epitaxial silicon pad sensors after neutron irradiation, using the transient current technique (TCT) and charge generation by red laser light of 672 nm wavelength. A model calculation is used assuming a quadratic dependence of the electric field on position and different parameterisations of the trapping time. Both the time-resolved current signals and the CCE as a function of bias voltage are described.

It is found that if a constant effective trapping time is assumed (τ const), the CCE as a function of bias voltage is not described, and if a linearly field dependent trapping time is assumed ($\tau = \tau_0 + \tau_1 \cdot E$), the CCE as a function of bias voltage is described (Figure 5.3). In Ref. [19] it is also observed that the CCE is described if a linearly-voltage-dependent trapping time is assumed, as it is also done in Ref. [14].

In order to distinguish between a dependence on the local electric field, and a dependence on the average electric field, i.e. the applied voltage, trapping must be studied as a function of sensor depth ($\tau(x)$). Changes in the applied bias voltage affect not only the electric field, but also the local hole and electron current densities and consequently the occupation of trapping centres. Hence many different explanations for a voltage dependent trapping time are possible.

In this work, charge losses are not studied as a function of sensor depth and only effective numbers can be given. Instead a simple model is used, based on the concept of the effective drift distance $\bar{\lambda}$. The main advantage compared to the description using an effective trapping time is that neither assumptions on the drift-velocity profile nor time-resolved current signals are required.

Effective drift distance

In this work the effective drift distance $\bar{\lambda}$ is calculated for a given voltage above full depletion using the CCE and the sensor thickness. With the drift distance, λ, an exponential reduction of free charge carriers drifting in positive x-direction, N, due to trapping is described as

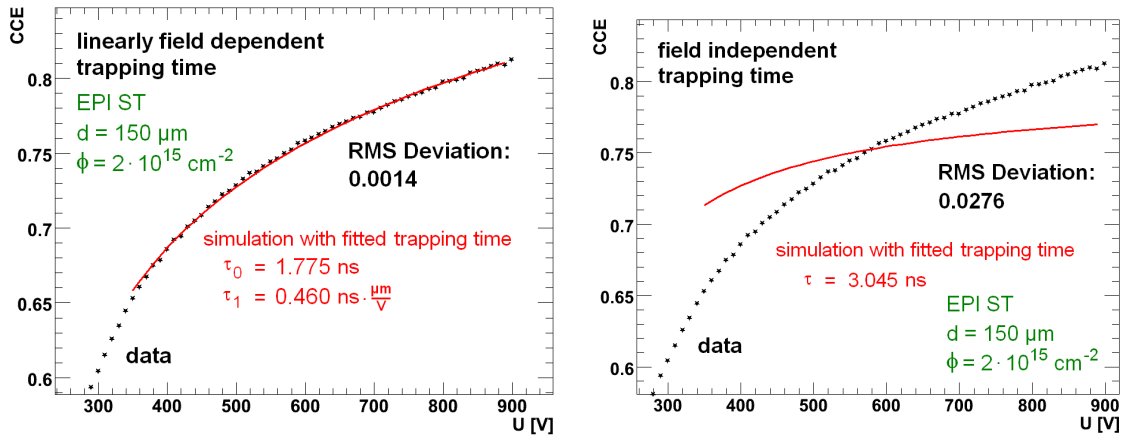

Figure 5.3: CCE as a function of bias voltage compared to model calculations using different trapping models taken from [19]. Left: assuming a linearly field dependent trapping time ($\tau = \tau_0 + \tau_1 \cdot E$). Right: assuming a constant trapping time τ const.

follows:

$$\mathrm{d}N = -\frac{N}{\lambda}\,\mathrm{d}x. \tag{5.3}$$

A drift distance λ large compared to the active sensor thickness corresponds to many charge carriers reaching the collecting electrode. Due to a position-dependent electric field distribution and a position-dependent occupation of trapping centres, the distance that free charge carriers drift before being trapped is in general a position dependent number, $\lambda = \lambda^{e,h}(x)$. It may be different for drifting electrons (e) and drifting holes (h). Since especially the occupation of trapping centres is not known quantitatively, in this work only an effective drift distance $\bar{\lambda}$ is calculated. $\bar{\lambda}$ is the drift distance, that in the case of $\lambda^{e,h}(x) = \bar{\lambda}$ gives the measured CCE. The simplification of $\lambda^{e,h}(x)$ to a single constant $\bar{\lambda}$ is only meaningful for voltages sufficiently above full depletion. Otherwise low-field regions are present with effectively zero drift distance.

If eh pairs are generated using light of 672 nm wavelength (∼3.5 µm penetration depth in silicon), the signal is dominated by the collection of one charge carrier type only (Section 3.2), and $\bar{\lambda}$ may be considered to be the effective drift distance for that carrier type. If eh pairs are generated using light of 1063 nm wavelength, both electrons and holes contribute significantly to the signal, and $\bar{\lambda}$ may be considered as an effective average of electron drift distance ($\lambda^e(x)$) and hole drift distance ($\lambda^h(x)$).

For charge carriers generated close to the sensor surface (e.g. by red light of 672 nm wavelength) the relation between the CCE and $\bar{\lambda}$ is given by

$$CCE_{red} = \frac{\bar{\lambda}}{d}\left(1 - e^{-\frac{d}{\bar{\lambda}}}\right), \tag{5.4}$$

and for charge carriers generated approximately uniformly along the sensor depth (e.g. by

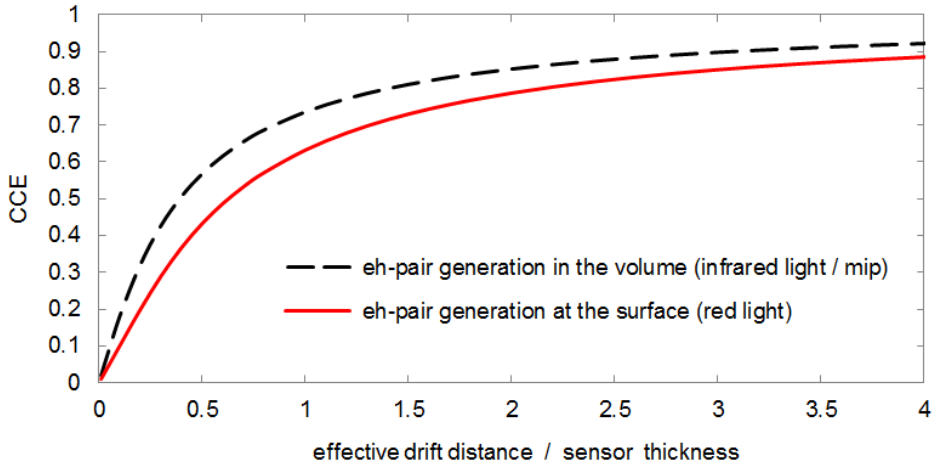

Figure 5.4: CCE as a function of effective drift distance, $\bar{\lambda}$, for charge carriers generated at the surface (red line) and charge carriers generated along the sensor depth (black, dashed line), according to Equations (5.4) and (5.5).

infrared light of 1063 nm wavelength) it is given by

$$CCE_{infrared} = 2 \cdot \frac{\bar{\lambda}^2}{d^2} \left(e^{-\frac{d}{\bar{\lambda}}} - 1 + \frac{d}{\bar{\lambda}} \right). \tag{5.5}$$

The relations are shown in Figure 5.4 and a derivation is given below.

For $\lambda(x) = \bar{\lambda}$, the number of free charge carriers drifting in the positive x-direction (N) changes as following:

$$\mathrm{d}N = -\frac{N}{\bar{\lambda}} \mathrm{d}x. \tag{5.6}$$

For N_0 particles traveling from $x = 0$ to $x > 0$ it follows:

$$N(x) = N_0 \cdot e^{-x/\bar{\lambda}}. \tag{5.7}$$

According to the Shockley-Ramo theorem for pad sensors, a point charge q_0 drifting with drift velocity v_{dr} induces a current on the pad read out, $I = v_{dr} \cdot q_0/d$. If drifting charge carriers are trapped, the amount of drifting charge q is non-constant, but given by

$$q(x - x_0) = N_0 \cdot q_0 \cdot e^{-\frac{x-x_0}{\bar{\lambda}}} = Q_0 \cdot e^{-\frac{x-x_0}{\bar{\lambda}}}, \tag{5.8}$$

where N_0 is the number of drifting charge carriers at $x = x_0$, q_0 is the charge of one charge carrier, and $Q_0 = N_0 \cdot q_0$ is the charge at x_0. For a pad sensor with thickness d, and a distance travelled, l, the integrated signal Q^l is then given by

$$Q^l = \int I \, \mathrm{d}t = \int \frac{q(x(t))}{d} \cdot v_{dr} \, \mathrm{d}t = \int_0^l \frac{Q_0 \cdot e^{-x/\bar{\lambda}}}{d} \, \mathrm{d}x = \frac{\bar{\lambda} \cdot Q_0}{d} \left(1 - e^{-l/\bar{\lambda}} \right). \tag{5.9}$$

For eh pairs generated by 672 nm light, the penetration depth of the light into the silicon

(3.5 µm) may be neglected. Using this approximation, only one charge carrier type drifts from $x = 0$ to $x = d$, and the CCE is given by

$$CCE_{red} = \frac{Q^d}{Q_0} = \frac{\bar{\lambda}}{d}\left(1 - e^{-\frac{d}{\bar{\lambda}}}\right), \tag{5.10}$$

according to Equation (5.9) with $l = d$.

For measurements with charge carriers generated by 1063 nm light, the attenuation length in silicon is large compared to the thickness of the investigated sensors and an uniform charge-carrier generation along the sensor depth may be assumed. Now both electron and hole drift are relevant. If a total charge Q_0 is generated, the locally generated charge density is given by $\rho = Q_0/d$.

Let us consider the drift of electrons first. For each distance, l, to the electron-collecting electrode, with $0 < l < d$, there are $\rho \cdot \Delta l$ electrons generated in the region $l < x < l + \Delta l$. For small Δl their contribution, ΔQ^l, to the total electron signal, $Q_{e,infrared}$, may be calculated using Equation (5.9):

$$\Delta Q^l = \frac{\bar{\lambda}^e \rho \Delta l}{d}\left(1 - e^{-l/\bar{\lambda}^e}\right). \tag{5.11}$$

The total induced signal, due to the drift of all electrons, is hence given by

$$Q_{e,infrared} = \int_0^d \frac{\bar{\lambda}^e \rho}{d}\left(1 - e^{-l/\bar{\lambda}^e}\right) \mathrm{d}l = \frac{(\bar{\lambda}^e)^2 \cdot Q_0}{d^2}\left(e^{-\frac{d}{\bar{\lambda}^e}} - 1 + \frac{d}{\bar{\lambda}^e}\right). \tag{5.12}$$

The CCE is hence given by

$$\begin{aligned} CCE_{infrared} &= \frac{Q_{e,infrared} + Q_{h,infrared}}{Q_0} \\ &= \left(\frac{\bar{\lambda}^e}{d}\right)^2 \cdot \left(e^{-\frac{d}{\bar{\lambda}^e}} - 1 + \frac{d}{\bar{\lambda}^e}\right) + \left(\frac{\bar{\lambda}^h}{d}\right)^2 \cdot \left(e^{-\frac{d}{\bar{\lambda}^h}} - 1 + \frac{d}{\bar{\lambda}^h}\right), \end{aligned} \tag{5.13}$$

and if the same $\bar{\lambda}$ is used for electrons and holes by

$$CCE_{infrared} = 2 \cdot \frac{\bar{\lambda}^2}{d^2}\left(e^{-\frac{d}{\bar{\lambda}}} - 1 + \frac{d}{\bar{\lambda}}\right). \tag{5.14}$$

5.5 Results

In this section the measured charge-collection efficiencies will be presented, as well as corresponding mip signals and effective drift distances. For the generation of eh pairs mainly laser light of 1063 nm wavelength is used. 1063 nm light traverses the whole sensor and generates eh pairs along the whole sensor depth, similar to mips or other high-energetic charged particles which are of relevance at the CMS detector. Results are presented as a function of irradiation type and fluence, as a function of bias voltage, for different operating temperatures, at different annealing states and for different materials. Additionally a comparison to measurements with

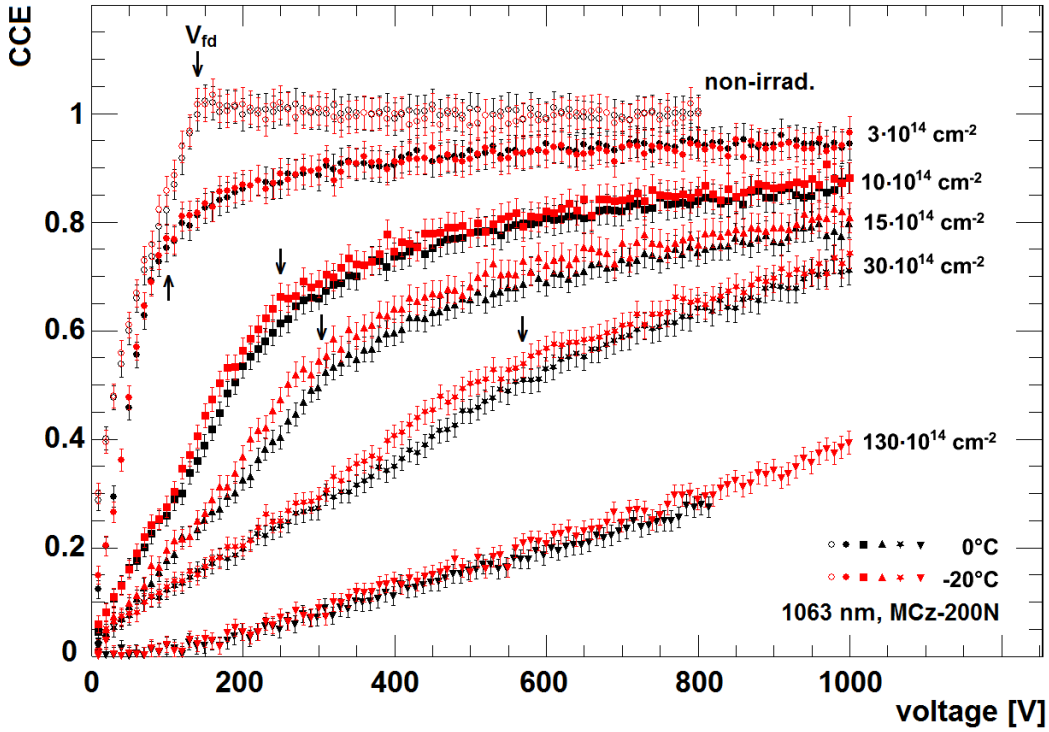

Figure 5.5: CCE for 200 µm thick MCz n-type sensors for different fluences of 23 GeV protons. Measured at 0 °C and -20 °C with the charge generated using laser light of 1063 nm wavelength. The sensors are measured as irradiated. The arrows indicate the full-depletion voltage obtained in CV measurements (-20 °C, 455 Hz).

charge generation close to the sensor surface is given, using 672 nm light.

5.5.1 Voltage dependence

Figure 5.5 shows the CCE as a function of voltage, for MCz sensors after irradiation with 23 GeV protons with different fluences and temperatures. For non-irradiated sensors, the collected charge increases with the depletion depth, and for fully depleted sensors the charge is approximately constant. The full-depletion voltage, V_{fd}, can be easily read off at the kink of the curve (Figure 5.5), which might also be defined as the point where the negative curvature of the shown CCE curve is maximal.

At moderate fluences ($\leq 1.5 \cdot 10^{15}$ neq/cm^2), a strong increase of the CCE with voltage is observed at low voltages, followed by a moderate increase at higher voltages. However, the CCE is not constant at high voltages and does not reach unity. Further, no clear kink, which would be indicating full depletion of the sensor, is observed. In analogy to the non-irradiated case, V_{fd} may be defined as the voltage of the point of maximal (negative) curvature of the CCE. Such a definition is similar to the full-depletion voltage extracted from CV measurements, which is indicated in Figure 5.5 by arrows. In this work the term “full-depletion voltage” will be used as a qualitative description of the CCE curve, and does not claim to give direct information on the amount of free charge carriers in the sensor, nor on the electric-field

distribution.

For high fluences ($\geq 3 \cdot 10^{15}$ neq/cm^2), the transition between strong increase of the CCE to a moderate increase is less pronounced. For the highest fluence investigated, $13 \cdot 10^{15}$ neq/cm^2, the slope of the CCE remains approximately constant up to 1000 V, which is the limit of the used setup.

After irradiation the CCE is smaller than unity for all voltages (up to 1000 V) and for all sensors investigated in this work (200 and 300 µm thick sensors).

5.5.2 Temperature dependence

At low voltages, around and below the full-depletion voltage, the CCE may depend on temperature and is slightly higher at -20 °C compared to 0 °C. A typical example of the temperature dependence is shown in Figure 5.5. At high voltages however, no significant difference between -20 °C and 0 °C is observed in the CCE.

For the highest fluence of $13 \cdot 10^{15}$ neq/cm^2, measurements at 0 °C are only performed up to 800 V, due to a high sensor current (∼800 µA at 800 V).

5.5.3 Annealing behaviour

The CCE is not observed to be annealing-time dependent at voltages sufficiently above the full-depletion voltage. Two typical examples are shown in Figure 5.6. At low voltages, $V < V_{fd}$, the CCE is annealing-time dependent. Up to an annealing time of 80 min at 60 °C the CCE increases, for higher annealing time it decreases. At high voltages, $V \gg V_{fd}$, no dependence on annealing time is observed.

Figure 5.7 shows the mip signals at 600 V as a function of annealing time for different materials after $4 \cdot 10^{14}$ cm^{-2} neutron irradiation. For most materials, little dependence on the annealing time is found at 600 V. Only for the 300 µm thick float-zone p-type material (dd-FZ-300P) a clear increase of the signal is observed for 80 min at 60 °C compared to both lower and higher annealing times.

5.5.4 Material dependence

In this section the CCE measurements for different materials will be presented. At first, measurements on MCz materials and on dd-FZ materials after 23 MeV proton irradiation with a fluence of 10^{15} neq/cm^2 will be presented. For these materials the most pronounced effects have been observed. Thereafter, an overview over all investigations is given.

Comparison of MCz and dd-FZ materials after 10^{15} neq/cm^2

In Figure 5.8 the CCE as a function of voltage is shown for different materials after 23 MeV proton irradiation with a fluence of 10^{15} neq/cm^2 . The charge is generated using laser light of 1063 nm wavelength. The following observations are made:

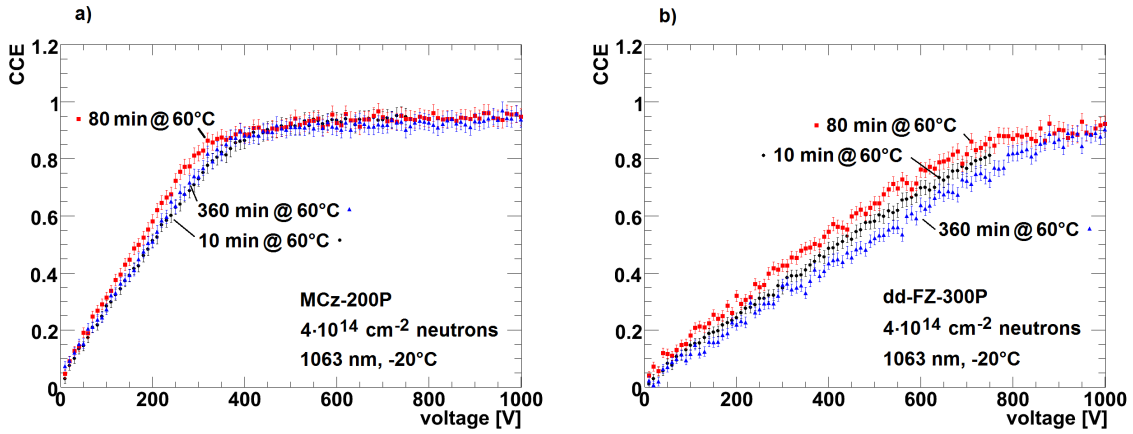

Figure 5.6: Annealing behaviour of the CCE as a function of voltage after irradiation with $4 \cdot 10^{14}$ cm^{-2} neutrons. Measured at -20 °C, using laser light of 1063 nm wavelength. a) For a 200 µm thick MCz p-type sensor. b) For a 300 µm thick float zone p-type sensor.

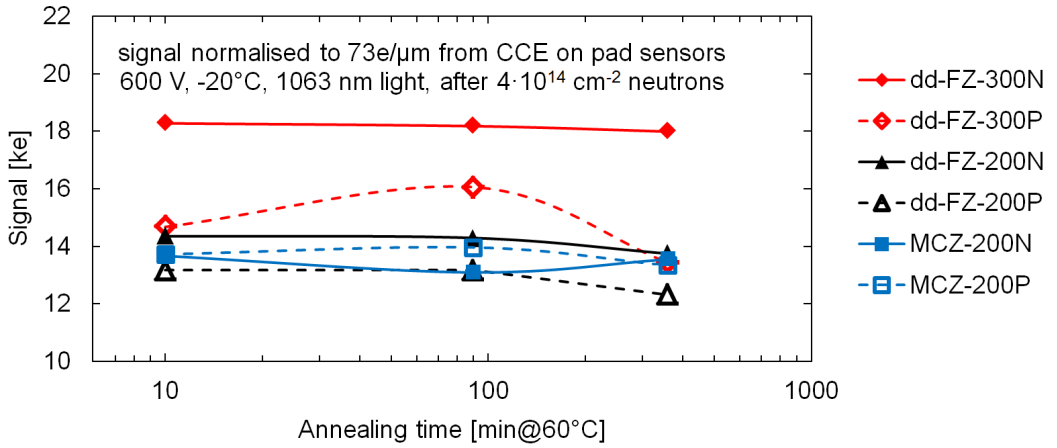

Figure 5.7: Annealing behaviour of the mip signal at 600 V for different materials after irradiation with $4 \cdot 10^{14}$ cm^{-2} neutrons. Measured at -20 °C with the charge generated using 1063 nm light. Lines are to guide the eye.

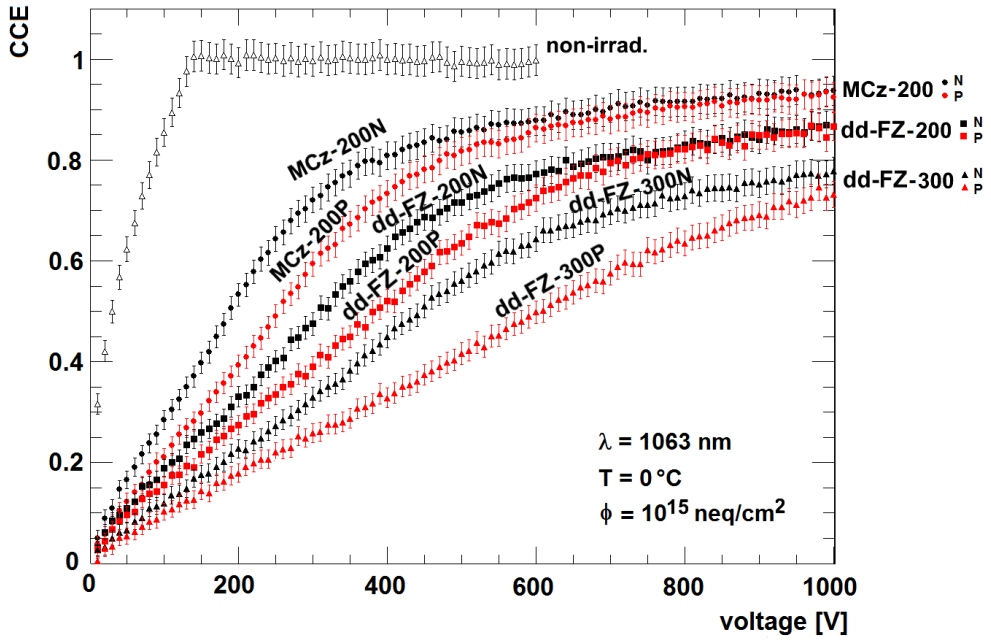

Figure 5.8: CCE as a function of voltage for MCz and dd-FZ materials after 23 MeV proton irradiation with a fluence of 10^{15} neq/cm^2. The charge is generated using laser light of 1063 nm wavelength at a temperature of 0 °C. For comparison also a non-irradiated sensor is shown.

- For all voltages MCz-200 material has higher CCE than the dd-FZ-200 material, and the dd-FZ-300 material has lowest CCE ($CCE_{MCz-200} > CCE_{dd-FZ-200} > CCE_{dd-FZ-300}$ for all V).

- For all three materials, at low voltages, the CCE is higher for the n-type sensor than for the corresponding p-type sensor ($CCE_{n-type} > CCE_{p-type}$ for $V \lesssim V_{fd}$).

- For all three materials, at high voltages, the CCE is the same for the n-type sensor as for the corresponding p-type sensor ($CCE_{n-type} \approx CCE_{p-type}$ for $V \gg V_{fd}$), where for the dd-FZ-300-P material $V \gg V_{fd}$ is barely reached at 1000 V.

Corresponding mip signals are calculated according to Equation (5.2) and shown in Figure 5.9. The signal for 300 µm material crosses the signals of 200 µm thick materials at voltages of ∼500 V for n-doped bulk and at voltages of ∼700 V for p-doped bulk. For higher voltages the mip signal is larger in 300 µm thick material.

The effective drift distance as a function of bias voltage is shown in Figure 5.10. The results are derived using Equation (5.5) and the active thickness is taken from Table 5.1. For all materials the effective drift distance increases with bias voltage without signs of saturation. The uncertainty of the effective drift distance is dominated by the uncertainty of the CCE (3 %) and is large for small amounts of charge losses, i.e. if $1 - CCE \ll 1$.

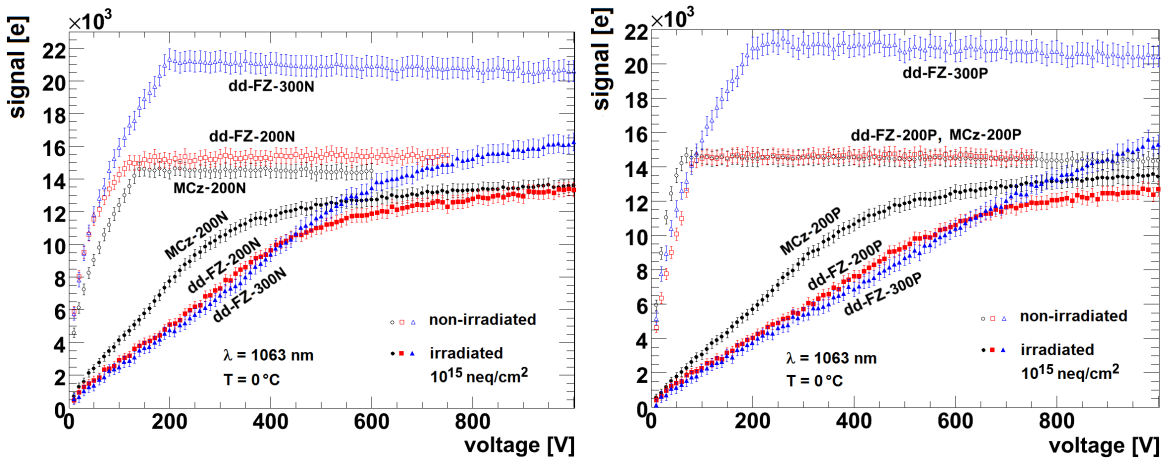

Figure 5.9: Most probable value for the signal of a minimum-ionising particle traversing the sensor. The shown data is calculated from the CCE presented in Figure 5.8 according to Equation (5.2). Different sensors after 23 MeV proton irradiation with a fluence of 10^{15} neq/cm^2 are shown. Left: n-type sensors. Right: p-type sensors. The shown error bars correspond to a CCE uncertainty of 3 %.

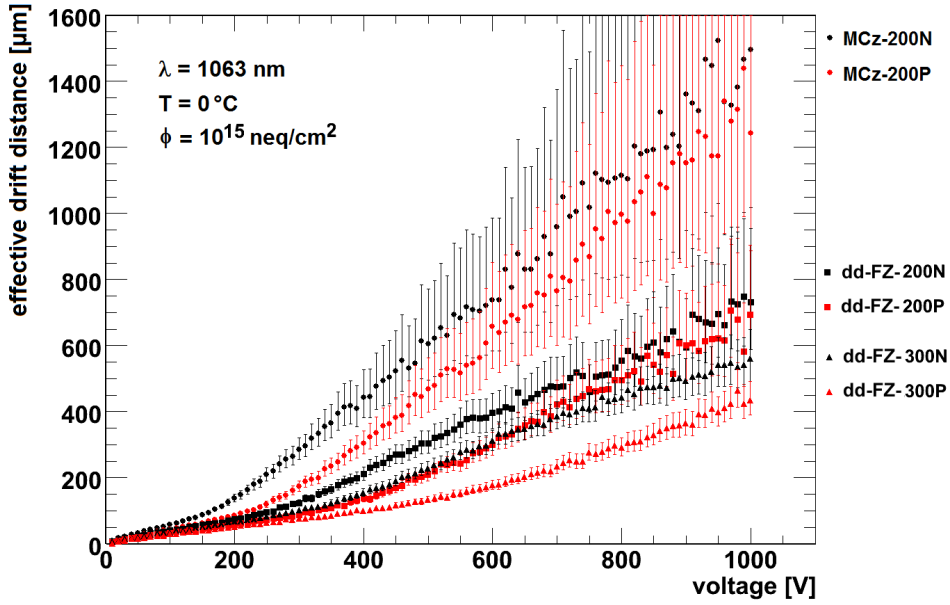

Figure 5.10: The effective drift distance for MCz and dd-FZ materials after 23 MeV proton irradiation with a fluence of 10^{15} neq/cm^2 is shown. The error bars correspond to a CCE uncertainty of 3 %.

particle type	neq fluence [10^{14} cm^{-2}]	CCE for MCZ-200N	CCE for MCZ-200P	CCE for dd-FZ-200N	CCE for dd-FZ-200P	CCE for dd-FZ-300N	CCE for dd-FZ-300P
23 MeV protons	2.9	0.97	0.92	0.87	0.85	0.86	0.85
23 MeV protons	10	0.87	0.89	0.76	0.72	0.64	0.48
reactor neutrons	4	0.94	0.94	0.90	0.88	0.84	0.70
mixed (p+n)	2.9+4	0.88	0.87	0.84	0.76	0.67	0.53
mixed (p+n)	10+5	0.77	0.69	0.64	0.59	0.46	0.37

Table 5.3: CCE at 600 V bias voltage after irradiation with reactor neutrons and 23 MeV protons. Light of 1063 nm wavelength is used for charge generation at a temperature of -20 °C. The sensors are measured after annealing of 10 minutes at 60 °C.

Overview over all investigated materials

An overview of CCE measurements for sensors of the same materials as discussed above, after irradiation with reactor neutrons and after irradiation with 23 MeV protons of different fluences, is given in Table 5.3. The CCE is shown at a bias voltage of 600 V and a temperature of -20 °C. No significantly different effects are observed, compared to those already discussed above.

An overview of CCE measurements for sensors after 23 GeV proton irradiation is given in Table 5.4. The CCE is shown at a bias voltage of 600 V and a temperature of -20 °C. Standard FZ material (n-type and p-type), and MCz material (n-type and p-type) is used. The CCE is similar for both materials and both doping types. In all cases it decreases with fluence, from ∼0.95 at the lowest fluence ($2.87 \cdot 10^{14}$ neq/cm^2) to ∼0.2 at the highest fluence ($131 \cdot 10^{14}$ neq/cm^2). The CCE for other voltages can be found in the appendix.

An overview of the mip signals as a function of fluence is given in Figure 5.11, for all investigated materials and all irradiations performed. Data is shown at bias voltages of 600 V (left) and 900 V (right), at a temperature of -20 °C. The strongest dependence seen in this figure is the dependence on the sensor thickness after irradiation with reactor neutrons and 23 MeV protons (Figure 5.11 bottom). For non-irradiated sensors and for sensors irradiated to low fluences, higher signals are observed for the 300 µm thick materials. At 600 V the signals in 300 µm thick and 200 µm thick dd-FZ sensors are similar after $\sim 7 \cdot 10^{14}$ neq/cm^2 for p-doped bulk and after $\sim 15 \cdot 10^{14}$ neq/cm^2 for n-doped bulk, and at higher fluences less signals is observed in the thicker materials. At 900 V the signals are similar after $\sim 15 \cdot 10^{14}$ neq/cm^2 for p-doped bulk, and for n-type bulk the thicker sensors have higher signals for all fluences investigated.

At higher fluences only measurements on 200 µm thick sensors (MCz and FZ) after 23 GeV

particle type	neq fluence [10^{14} cm^{-2}]	CCE for MCZ-200N	CCE for MCZ-200P	CCE for FZ-200N	CCE for FZ-200P
23 GeV protons	2.87	0.92	0.96	0.98	0.91
23 GeV protons	10.8	0.81	0.85	0.83	0.80
23 GeV protons	15.9	0.72	0.76	0.80	0.76
23 GeV protons	29.4	0.54	0.59	0.61	0.58
23 GeV protons	131	0.21	0.23	0.19	0.22

Table 5.4: CCE at 600 V bias voltage after irradiation with 23 GeV protons. Light of 1063 nm wavelength is used for charge generation at a temperature of -20 °C. The sensors are measured as irradiated. Some annealing took place during irradiation.

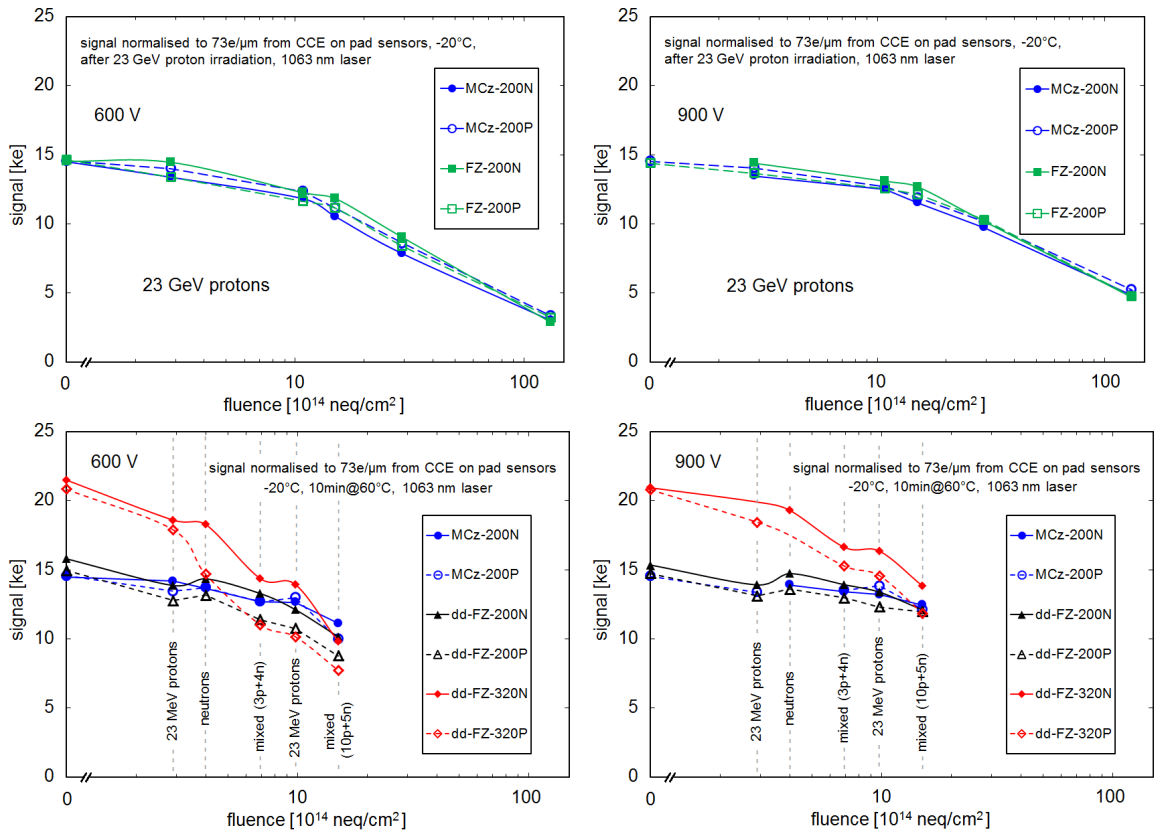

Figure 5.11: Mip signals as a function of fluence at 600 V (left) and 900 V (right) for all materials and irradiations investigated in this work. The sensors are measured at -20 °C with the charge generated using 1063 nm laser light. After irradiation with 23 GeV protons (top), the sensors are measured as irradiated. After irradiation with 23 MeV protons, neutrons or both (bottom), the sensors are measured after 10 min annealing at a temperature of 60 °C. Lines are to guide the eye.

proton irradiation are available and little dependence on the material is observed. At 900 V higher signals, i.e. less charge losses, are observed compared to 600 V. At the highest fluence the signal increases from ∼3000 electrons at 600 V to ∼5000 electrons at 900 V.

5.5.5 Dependence on position of *eh*-pair generation

The CCE is shown for charge carriers generated at different positions in a 200 µm thick MCz sensor after 23 MeV proton irradiation with a fluence of 10^{15} neq/cm^2 in Figure 5.12a. Laser light with a wavelength of 672 nm is used to generate *eh* pairs at the n^+ side (front-side illumination) and at the p^+ side (rear-side illumination) of the n-on-p sensor, and laser light with a wavelength of 1063 nm is used to generate *eh* pairs uniformly along the sensor depth. For $V > 150$ V a lower CCE is observed for charge carriers generated close to the sensor surfaces, compared to the CCE of charge carrier generated along the sensor depth.

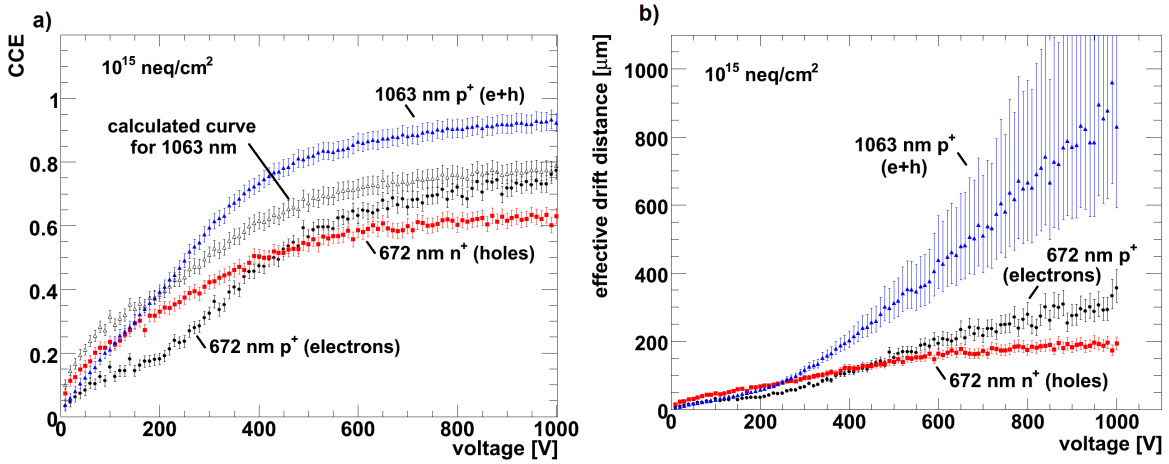

Figure 5.12: CCE (a) and effective drift distance (b) as a function of voltage for different positions of *eh*-pair generation. Light of 672 nm and 1063 nm wavelength is used. Data is shown for a 200 µm thick p-type MCz sensor after irradiation with 23 MeV protons to a fluence of 10^{15} neq/cm^2. (b) is calculated from (a) using Equation 5.5 for illumination with 1063 nm light and using Equation 5.4 for p^+ and n^+ illumination with 672 nm. The calculated CCE curve in (a) is calculated from the effective drift distances for 672 nm light shown in (b) according to Equation 5.13.

The effective drift distance for charge carriers generated at different positions in the sensor is shown in Figure 5.12b. The effective drift distances for electrons, obtained from 672 nm light p^+ illumination, and for holes, obtained from 672 nm light n^+ illumination, are used to calculate the expected CCE for illumination with 1063 nm light assuming a position independent drift distance according to Equation 5.13. It is found that the calculated CCE at high voltages is ∼12 % higher then the measured CCE for 1063 nm light.

5.6 Discussion

5.6.1 Voltage dependence

At low voltages, below V_{fd}, regions with zero or very small electric fields occur (non-depleted regions). If *eh* pairs are generated in the non-depleted regions they either recombine or get trapped in radiation-induced trapping centres before they contribute significantly to the signal, due to their very small drift velocities. With increasing bias voltage the width of the low-field region decreases, i.e. the depleted volume gets larger, and more charge carriers may contribute significantly to the signal.

The increase in the CCE is expected to be strongest until the electric field is relatively high over the whole sensor depth. A further increase of voltage still enhances the local electric fields and leads to higher drift velocities and less charge trapping. Consequently the CCE is still expected to rise. The measured CCE as a function of voltage shows such a dependence: a strong rise at low voltages followed by a moderate increase at higher voltages (Figures 5.5 and 5.8). At high fluences the CCE keeps increasing strongly up to 1000 V (Figure 5.5), indicating that up to that voltage, there are still regions with low electric fields present in the sensor.

5.6.2 Temperature dependence

Changes in the temperature affect the current generation, the drift velocity and the detrapping time of trapped charge carriers. Changes in the drift velocity, due to a temperature change of 20 °C, are in the order of 10 %, and will not be discussed here. However, the current generation is significantly lower at -20 °C compared to 0 °C. Hence, the current-induced occupation of traps (double junction) is less significant. At the same time, longer detrapping times increase the double-junction effect, because traps are occupied for a longer time once they are filled. No simple prediction can be made in the framework of this thesis, whether and how much the space charge (or the effective doping concentration, N_{eff}) is changed. However, the observed changes in CCE are well described by a slightly lower full-depletion voltage at -20 °C, compared to 0 °C (Figure 5.5) which corresponds to a decrease in space charge for not-type-inverted n-type sensors. A decrease of space charge for lower temperatures is also observed in Ref. [93] where the electric-field distribrution is simulated for irradiated sensors using two defect levels in the forbidden silicon band gap and Shockley-Read-Hall statistics.

5.6.3 Annealing behaviour

The annealing behaviour of the CCE may be explained by a change in V_{fd}. At a given low voltage, $V < V_{fd}$, the total width of the depleted regions depends on V_{fd}. If V_{fd} decreases, the electric-field distribution is more uniform and there is less non-depleted volume. Consequently more charge carriers contribute to the signal and the CCE is increased. At sufficiently high voltages, $V \gg V_{fd}$, no low-field regions are present, and the amount of charge carriers

contributing to the signal does not depend on V_{fd}.

A shift of the full-depletion voltage with annealing time was already observed and explained by defect kinetics elsewhere (Section 2.3.2, [17]). Up to 80 min at 60 °C, the density of radiation induced acceptors decreases. In the case of type inverted sensors, which were initially n-type, this leads to lower full-depletion voltages, and the effect is called beneficial annealing. For longer annealing times an increase of acceptor concentration is observed and the effect is called reverse annealing.

If the signal, which is proportional to the CCE, is plotted as a function of annealing time and for a fixed bias voltage V, two cases may be distinguished: If the full-depletion voltage is sufficiently small ($V_{fd} \ll V$), the sensor is fully depleted independent of annealing time, and no difference in signal height is expected. If the full-depletion voltage is higher than the bias voltage ($V_{fd} > V$), the depletion width changes with annealing time due to a change in effective doping concentration, N_{eff}, and hence a change in signal is expected. This is exactly what is observed in Figure 5.7. A strong change in signal (> 1000 e) is only observed for the dd-FZ-300P material, which has a full-depletion voltage $V_{fd} > 600$ V as seen in Figure 5.6.

5.6.4 Material and thickness dependence

n-type vs. p-type sensors

The CCE dependence on the initial doping type (Figure 5.8) may be explained by a difference in the absolute value of effective doping concentration, $|N_{eff}|$, which is proportional to V_{fd}. At high voltages, $V \gg V_{fd}$, the electric-field distribution has little dependence on N_{eff}, and charge collection in n-type and p-type sensors is similar. At low voltages, $V \lesssim V_{fd}$, the CCE is smaller for higher values of V_{fd}, due to a smaller depletion width. After irradiation with 23 MeV protons, all investigated n-type sensors underwent type inversion ($N_{eff} < 0$) and have a lower full-depletion voltage than the corresponding p-type sensors, which did not undergo type inversion ($N_{eff} < 0$). Hence after irradiation the effective doping concentration has the same sign for both initial doping types, and its absolute value is larger for not type-inverted sensors, since the initial dopants only then contribute positively to the absolute value.

It should be noted, that the electrodes in pad sensors are symmetric, i.e. the only difference in charge collection between p-type sensors (n^+-p-p^+), and n-type sensors (p^+-n-n^+) is given by the bulk doping.

300 µm vs. 200 µm thick sensors

For a depletion width of less than 200 µm, little difference between 200 µm and 300 µm thick sensors is expected for the electric-field distribution and hence for the charge collection. Consequently the signal, which corresponds to a mip traversing the sensor, is similar in both cases for low voltages $V \lesssim V_{fd}$ (Figure 5.9). For higher voltages, more charge carriers contribute to the signal for 300 µm thick sensors. Similar effects are observed for dd-FZ-200 and dd-FZ-300 materials.

For low voltages where the mip signals are similar for 300 µm and 200 µm thick sensors, the CCE is less in 300 µm sensors due to the higher mip signals in non-irradiated 300 µm sensors. At high voltages, $V \gg V_{fd}$, the average electric field in 300 µm thick sensors is smaller than the average electric field in 200 µm sensors. Consequently also the drift velocity is smaller, which explains the observation of a shorter effective drift distance, as well as the lower CCE (Figures 5.10 and 5.8).

MCz, FZ and dd-FZ materials

It is well known that irradiation-induced defects depend on the particle type, on the particle energy [94] and on the silicon material [78, 35]. Typically materials with a high oxygen concentration (MCz) are distinguished from materials with a low oxygen concentration (FZ). After irradiation with 23 MeV protons, more charge losses (and shorter effective drift distances) are observed in dd-FZ-200 sensors compared to MCz-200 sensors (Figures 5.8 and 5.10), hinting at a higher concentration of non-filled trapping centres in dd-FZ material. Due to the similar oxygen content in dd-FZ and MCz materials according to SIMS measurements (Table 5.1), this observation is somehow surprising. In previous studies no significant material dependence was found in trapping parameters [92].

Similar CCEs are found in FZ and MCz sensors after irradiation with 23 GeV protons. This corresponds to a similar concentration of non-filled trapping centres in this case. 23 GeV protons create more cluster defects compared to low energy protons [94]. It is not clear whether a difference between MCz and FZ material is observed only for low energy irradiations, or whether a difference is observed only if deep diffused material (320 µm thick sensors with an active thickness of ∼200 µm) is compared with material of 200 µm physical and active thickness. Further studies are foreseen with ∼200 µm thick FZ material after 23 MeV proton irradiation.

5.6.5 Dependence on the position of *eh*-pair generation

For charge carriers generated along the sensor depth by 1063 nm light a higher CCE is observed compared to the CCE for charge carriers generated close to the implants by 672 nm light. As already observed in Figure 5.4 this is expected even if the effective drift distances were the same for cases. If the effective drift distances are calculated from the measurements using 672 nm light and this drift distances are used to calculated the corresponding CCE for 1063 nm light, then the calculated CCE is higher then the measured CCE for 672 nm light (Figure 5.12a). However, the measured CCE for 1063 nm light is significantly higher then the calculated CCE, and the observed effective drift distances are not the same for 672 nm light and 1063 nm light but depends on the position of *eh*-pair generation.

The observation that charge carriers generated at the surface experience more trapping, i.e. that a shorter effective drift distance is observed, is qualitatively expected due to a non-uniform occupation of radiation-induced defects. As already known from the double-junction

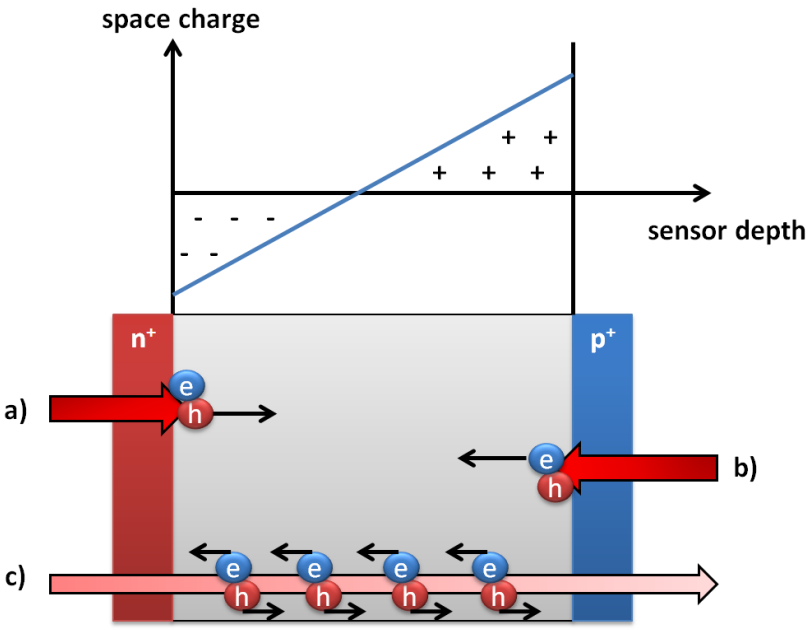

Figure 5.13: Schematic space-charge distribution in the silicon bulk according to the double-junction effect and TCT illumination modes. Illumination with laser light at the n^+ electrode using light of 672 nm wavelength (a), at the p^+ electrode using light of 672 nm wavelength (b), and at the n^+ electrode using light of 1063 nm wavelength (c).

effect [33, 34], the occupation of states is such, that negative space charge accumulates in the bulk close to the n^+ electrode and positive space charge accumulates in the bulk close to the p^+ electrode as shown in Figure 5.13. Hence we expect a high density of non-occupied electron traps close to the p^+ electrode and a high density of non-occupied hole traps at the n^+ electrode.

If eh pairs are generated close to the electrodes (672 nm light), the signal is dominated by one charge carrier type. For illumination at the n^+ electrode, the signal is dominated by the drift of holes to the p^+ electrode. All holes traverse the region with negative space charge and presumably high hole-trapping probability close to the n^+ electrode (Figure 5.13). If they are trapped in this region their contribution to the signal is very small due to the short distance travelled. For illumination at the p^+ electrode the corresponding effect for electron trapping takes place.

If eh pairs are generated along the sensor depth (1063 nm light), electrons are collected at the n^+ electrode and holes are collected at the p^+ electrode. Only a few electrons traverse the region of high electron-trapping probability close to the p^+ electrode, and only a few holes traverse the region of high hole-trapping probability close to the n^+ electrode. The CCE is expected to be relatively high corresponding to a high effective drift distance. Hence, the observation of different effective drift distances for different illumination modes is qualitatively in agreement with a non-uniform trap occupancy according to the double-junction effect.

5.7 Summary on charge losses in the silicon bulk

Charge losses in irradiated silicon pad sensors have been studied as a function of sensor thickness, doping type, material, irradiation type, fluence, voltage, temperature and position of charge-carrier generation. The sensors have been irradiated by reactor neutrons, 23 MeV protons and 23 GeV protons. For most investigations charge carriers have been generated along the whole sensor depth using laser light with a wavelength of 1063 nm. For light of this wavelength the distribution of eh-pair generation is similar as for particles present at the CMS experiment, like mips or other high-energetic particles. The CCE has been determined with a precision of 3 %, and the corresponding signal for mips has been calculated, as well as effective drift distance.

At moderate particle fluences ($\leq 1.5 \cdot 10^{15}$ neq/cm^2 for n-type sensors after 23 GeV irradiation), two voltage regions have been identified. A strong increase in the CCE has been observed at low voltages, and a moderate increase at higher voltages. In the high-voltage region, no dependence on temperature, annealing state or initial doping type has been observed, but only a dependence on irradiation, sensor thickness and material. In the low-voltage region the CCE additionally depends on temperature, annealing time and initial doping type corresponding to a change of the full-depletion voltage. At high fluences ($\geq 3 \cdot 10^{15}$ neq/cm^2 for n-type sensors after 23 GeV irradiation), no saturation of the CCE has been observed and the CCE depends on temperature for all voltages up to 1000 V, corresponding to the

low-voltage region below full depletion.

Deep-diffused float-zone material (dd-FZ) of different active thickness has been studied up to fluences of $1.5 \cdot 10^{15}$ neq/cm^2 of neutrons and 23 MeV protons. For a given voltage, the effective drift distance has been observed to be shorter for thicker sensors, corresponding to a lower value of the average electric field. However, the signal induced by a mip traversing the sensor has been observed to be larger for thick sensors, if the voltage is sufficiently high, corresponding to a higher number of *eh* pairs contributing to the signal. For dd-FZ silicon of 200 µm and 300 µm thickness operated at 600 V after mip signals are similar after $1.5 \cdot 10^{15}$ neq/cm^2 for n-type bulk and after $7 \cdot 10^{14}$ neq/cm^2 for p-type bulk. For higher fluences higher signals are observed in the 200 µm thick sensors, and for lower fluences higher signals are observed in the 300 µm thick sensors.

Float-zone (FZ) and magnetic-Czochralski (MCz) material of 200 µm thickness has been compared after irradiation with 23 GeV protons to fluences up to $13 \cdot 10^{15}$ neq/cm^2, and are found to give similar CCE and mip signals at sufficiently high bias voltages (600 V). Further, 320 µm thick FZ material which underwent a deep diffusion process to reduce the active thickness to ∼200 µm was compared to 200 µm thick MCz material. After irradiation with 23 MeV proton fluences of 10^{15} neq/cm^2 a higher CCE has been observed in MCz material, which corresponds to a longer effective drift distance in MCz.

Effective trapping parameters for charge generation at different sensor depths have been compared and indications for position dependent trapping have been found. The effective drift distance for *eh* pairs generated close to the surface, using light of 672 nm wavelength, has been found to be shorter than the effective drift distance for *eh* pairs generated along the sensor depth, using light of 1063 nm wavelength. It has been concluded that the charge collection is not compatible with the assumption of position independent trapping, but that more charge carriers are trapped close to the non-collecting electrode(n^+ for holes, p^+ for electrons). The observed position dependence of trapping probability qualitatively agrees with the expected trap occupation due to the double junction in irradiated silicon.

The studies give insight about charge carrier losses in pad sensors at HL-LHC fluences. While similar charge collection has been observed for FZ and MCz material after irradiation with 23 GeV protons, less CCE has been observed in dd-FZ material compared to MCz material after irradiation with 23 MeV protons. Both the tested FZ material and the tested MCz material seem to be an option for the strip region of the CMS tracker after the HL-LHC upgrade. dd-FZ material is an option if a higher physical thickness is required for mechanical stability. However, for CMS after the HL-LHC upgrade a digital read out is foreseen and the seed signal in strip sensors has to be studied and compared to the noise. Studies of the strip signals and the comparison to the charge collection in pad sensors will be reported in Ref. [36].

Chapter 6

Summary and Conclusion

6.1 Investigations on strip sensors

Segmented p^+n silicon strip sensors from two different producers have been used to study the electric field below the SiO_2 separating the strip implants using charge-collection measurements. *eh* pairs have been generated a few µm below and very close to the Si-SiO_2 interface by focussed and sub-ns pulsed laser light of 830 nm and 660 nm wavelength, respectively. Electrons trapped at the interface indicate an electric field pointing out of the SiO_2, and holes trapped at the interface indicate an electric field pointing into the SiO_2. The sensors have been investigated before and after irradiation with 12 keV x-rays to a dose of 1 MGy in the SiO_2.

It has been found that the electric field close to the Si-SiO_2 interface depends on the irradiation dose, on the biasing history and on the humidity. For the non-irradiated sensors the observations are qualitatively as expected from electrostatic-potential simulations for different boundary conditions at the surface. For the irradiated sensors it has been found that the dependences on humidity and on biasing history of the charge collection are not described by simulations if the charge of the radiation-induced interface states is approximated by a constant oxide-charge density.

The accumulation layers which form at the Si-SiO_2 interface have been studied operating the laser, which is used for *eh*-pair generation, in burst mode. 30 pulses per burst with different time spacings are used to study the charging up of the accumulation layers and the recovery of lost charge carriers. It is found that up to ∼500 000 additional charge carriers can be added to the accumulation layers in a non-irradiated sensor. Depending on the biasing history the additional charge carriers are holes being added to an already existing hole-accumulation layer, or electrons being added to an already existing electron-accumulation layer. For an irradiated sensor up to a few million additional electrons can be added to the accumulation layer. In the studied cases a significant amount of further additional charge carriers can be added to the accumulation layers (∼25 % to ∼60 % of the maximal amount of additional charge carriers) after a recovery time of 1 µs. The accumulation layer returns to the steady-state condition, the condition where the maximal amount of additional charge carriers can be added, after

$\sim$100 µs.

The studied region close to the Si-SiO_2 interface is relevant for the sensor stability and the studies provide an understanding of the influence of biasing history and humidity. For device simulations they give information about how to determine the boundary conditions on the top of the passivation layer.

6.2 Investigations on pad sensors

The charge-collection efficiency, CCE, in silicon pad sensors manufactured using crystal growth with different technologies has been investigated after irradiation with neutrons and protons as a function of particle fluence, bias voltage, temperature, annealing time and position of *eh*-pair generation. Mainly light of 1063 nm has been used for the generation of *eh* pairs and the achieved precision on the CCE is $\sim$3%. Additionally, signals corresponding to minimum-ionising particles traversing the sensor and effective drift distances of the generated charge carriers have been calculated from the CCE.

After irradiation with 23 GeV protons of fluences between $3 \cdot 10^{14}$ and $1.3 \cdot 10^{16}$ neq/cm^2 no significant difference in the CCE in 200 µm thick sensors of FZ silicon and of MCz silicon has been observed. After irradiation with reactor neutrons and 23 MeV protons the signals in dd-FZ sensors of 200 µm active thickness are $\sim$10 % lower (at 600 V) compared to the signals in 200 µm thick MCz sensors. Further, the bigger physical thickness of 320 µm for dd-FZ sensors is a disadvantage for physics analyses at the CMS experiment. However, since 320 µm thick sensors are easier to handle due to the higher mechanical stability, they are still an option for the phase-II upgrade of the CMS detector.

Depending on the fluence, on the applied bias voltage and on the initial doping type, either bigger or smaller signals are observed in sensors with an active thickness of $\sim$300 µm compared to sensors with an active thickness of $\sim$200 µm. At 600 V higher signals are observed in $\sim$300 µm thick sensors up to fluences of $\sim 1.5 \cdot 10^{15}$ neq/cm^2 for n-type bulk and up to $\sim 7 \cdot 10^{14}$ neq/cm^2 for p-type bulk. At higher fluences bigger signals are observed in 200 µm thick sensors. For the inner strip layers of the CMS tracker, fluences of up to $\sim 1.5 \cdot 10^{15}$ neq/cm^2 are expected after the phase-II upgrade, and both sensors with 200 µm and sensors with 300 µm active thickness are options. Finally, charge-collection measurements on segmented sensors are needed to decide which thickness to use in which region.

A dependence of the CCE on temperature and annealing time has been observed at voltages around and below the full-depletion voltage and can be described by a temperature and annealing-time dependent full-depletion voltage. At higher voltages no temperature or annealing-time dependence of the CCE has been observed.

The CCE and the effective drift distance has been also calculated for *eh* pairs generated close to the sensor surface using laser light of 660 nm wavelength. The measurements are not compatible with a position-independent trapping probability if they are compared to measurements using light of 1063 nm wavelength and the observed discrepancy is qualitatively

in agreement with a position-dependent occupation of radiation-induced trapping centres due to the dark current.

The observations made give insight into the important effects caused in the silicon bulk after hadron irradiation. They can be used to improve the understanding of charge collection in segmented sensors in which both material effects and sensor-layout effects are significant, and they can be used to tune device simulations in order to describe the charge losses in the silicon bulk due to radiation-induced defects.

Appendix

The CCE at different bias voltages

bias voltage	CCE for dd-FZ-200N	CCE for dd-FZ-200P	CCE for dd-FZ-320N	CCE for dd-FZ-320P	CCE for MCz-200N	CCE for MCz-200P
100 V	0.61	0.33	0.33	0.20	0.84	0.54
200 V	0.81	0.64	0.64	0.38	0.92	0.84
300 V	0.83	0.79	0.78	0.56	0.95	0.89
400 V	0.87	0.83	0.83	0.73	0.97	0.91
500 V	0.85	0.85	0.86	0.82	0.97	0.92
600 V	0.88	0.85	0.87	0.86	0.98	0.92
700 V	0.90	0.86	0.88	0.87	0.99	0.93
800 V	0.90	0.87		0.88		0.93
900 V	0.88	0.88		0.89		0.92
1000 V	0.90	0.88		0.89		0.93
100 V	0.19	0.16	0.14	0.10	0.29	0.22
200 V	0.33	0.27	0.24	0.18	0.53	0.40
300 V	0.48	0.39	0.35	0.26	0.71	0.61
400 V	0.63	0.51	0.47	0.32	0.80	0.76
500 V	0.73	0.63	0.57	0.41	0.84	0.86
600 V	0.77	0.72	0.65	0.49	0.87	0.89
700 V	0.79	0.77	0.70	0.57	0.88	0.92
800 V	0.82	0.81	0.73	0.63	0.91	0.94
900 V	0.85	0.82	0.76	0.70	0.91	0.95
1000 V	0.85	0.85	0.78	0.73	0.92	0.96

Table 1: CCE for sensors after 23 MeV proton irradiation to fluences of $2.9 \cdot 10^{14}$ neq/cm^2 (top) and $9.8 \cdot 10^{14}$ neq/cm^2 (bottom). The sensors are measured after annealing of 10 minutes at 60 °C. Light of 1063 nm wavelength is used for charge generation at a temperature of -20 °C.

bias voltage	CCE for dd-FZ-200N	CCE for dd-FZ-200P	CCE for dd-FZ-320N	CCE for dd-FZ-320P	CCE for MCz-200N	CCE for MCz-200P
100 V	0.30	0.22	0.20	0.15	0.46	0.29
200 V	0.58	0.43	0.37	0.26	0.78	0.51
300 V	0.80	0.63	0.57	0.37	0.88	0.74
400 V	0.86	0.78	0.72	0.49	0.91	0.87
500 V	0.90	0.85	0.81	0.60	0.93	0.92
600 V	0.91	0.88	0.85	0.70	0.94	0.94
700 V	0.90	0.90	0.88	0.79	0.94	0.94
800 V	0.92	0.91	0.89		0.94	
900 V	0.93	0.91	0.90		0.96	
1000 V	0.93	0.93	0.90			

Table 2: CCE for sensors after ∼1 MeV neutron irradiation to a fluence of $4 \cdot 10^{14}$ cm^{-2}. The sensors are measured after annealing of 10 minutes at 60 °C. Light of 1063 nm wavelength is used for charge generation at a temperature of -20 °C.

bias voltage	CCE for dd-FZ-200N	CCE for dd-FZ-200P	CCE for dd-FZ-320N	CCE for dd-FZ-320P	CCE for MCz-200N	CCE for MCz-200P
100 V	0.21	0.17	0.11	0.11	0.29	0.22
200 V	0.37	0.33	0.23	0.23	0.52	0.40
300 V	0.56	0.43	0.35	0.28	0.72	0.59
400 V	0.72	0.59	0.46	0.35	0.82	0.75
500 V	0.81	0.70	0.58	0.45	0.86	0.82
600 V	0.84	0.76	0.67	0.53	0.88	0.87
700 V	0.84	0.83	0.70	0.61	0.91	0.90
800 V	0.87	0.85	0.75	0.68	0.92	0.91
900 V	0.88	0.87	0.77	0.73	0.92	0.93
1000 V	0.89	0.87	0.80	0.79	0.93	0.94
100 V	0.13	0.15	0.09	0.09	0.17	0.13
200 V	0.23	0.24	0.16	0.15	0.29	0.25
300 V	0.33	0.30	0.23	0.21	0.43	0.36
400 V	0.43	0.41	0.28	0.26	0.59	0.49
500 V	0.53	0.50	0.38	0.33	0.69	0.61
600 V	0.64	0.59	0.46	0.37	0.77	0.69
700 V	0.71	0.67	0.52	0.45	0.80	0.77
800 V	0.78	0.74	0.62	0.51	0.83	0.80
900 V	0.77	0.80	0.64	0.57	0.86	0.83
1000 V	0.81	0.84	0.66	0.64	0.87	0.85

Table 3: CCE for sensors after mixed irradiation to fluences of $6.9 \cdot 10^{14}$ neq/cm^2 (top) and $14.8 \cdot 10^{14}$ neq/cm^2 (bottom). After irradiation with 23 MeV protons to a fluence of $2.9 \cdot 10^{14}$ neq/cm^2 ($9.8 \cdot 10^{14}$ neq/cm^2) and after 10 minutes annealing at 60 °C the samples are irradiated with ∼1 MeV neutrons with a fluence of $4 \cdot 10^{14}$ neq/cm^2 ($5 \cdot 10^{14}$ neq/cm^2). The sensors are measured after an additional 10 minutes annealing at 60 °C after neutron irradiation. Light of 1063 nm wavelength is used for charge generation at a temperature of -20 °C.

bias voltage	CCE for MCz-200N	CCE for MCz-200P	CCE for FZ-200N	CCE for FZ-200P
100 V	0.27	0.30	0.41	0.25
200 V	0.57	0.59	0.65	0.50
300 V	0.69	0.71	0.74	0.66
400 V	0.74	0.77	0.79	0.73
500 V	0.78	0.80	0.81	0.77
600 V	0.82	0.84	0.84	0.80
700 V	0.83	0.84	0.86	0.81
800 V	0.84	0.85	0.88	0.83
900 V	0.86	0.87	0.90	0.86
1000 V	0.88	0.89	0.92	0.86
100 V	0.20	0.19	0.25	0.22
200 V	0.37	0.38	0.53	0.43
300 V	0.55	0.56	0.65	0.60
400 V	0.64	0.65	0.72	0.68
500 V	0.69	0.70	0.76	0.73
600 V	0.73	0.74	0.81	0.76
700 V	0.77	0.78	0.81	0.78
800 V	0.76	0.81	0.84	0.81
900 V	0.80	0.82	0.87	0.83
1000 V	0.81	0.84	0.88	0.84
100 V	0.11	0.11	0.16	0.12
200 V	0.20	0.20	0.29	0.20
300 V	0.27	0.29	0.44	0.30
400 V	0.38	0.39	0.52	0.43
500 V	0.48	0.49	0.57	0.52
600 V	0.54	0.55	0.62	0.58
700 V	0.59	0.60	0.65	0.62
800 V	0.64	0.65	0.68	0.67
900 V	0.67	0.68	0.70	0.70
1000 V	0.72	0.72	0.73	0.73

Table 4: CCE for sensors after 23 GeV proton irradiation to fluences of $10.8 \cdot 10^{14}$ neq/cm^2 (top), $15.0 \cdot 10^{14}$ neq/cm^2 (middle), and $29.4 \cdot 10^{14}$ neq/cm^2 (bottom). The sensors are measured as irradiated with effective annealing times between ∼10 minutes at 60 °C and ∼60 minutes at 60 °C. Light of 1063 nm wavelength is used for charge generation at a temperature of -20 °C.

List of Figures

List of Tables

Bibliography

[1] M. Altarelli et al. (Eds.), *XFEL: The European X-Ray Free-Electron Laser, Technical Design Report*, Preprint DESY 2006-097, DESY, Hamburg 2006, ISBN 978-3-935702-17-1 (2006).

[2] The website of the European X-Ray Free-Electron Laser: `http://www.xfel.eu/`.

[3] Deutsches Elektronen-Synchrotron, Notkestrasse 85, D-22607 Hamburg, Germany, `http://www.desy.de/`.

[4] Lyndon Evans and Philip Bryant, *LHC Machine*, JINST 3 S08001 (2008).

[5] CERN, 385 Route de Meyrin, 1217 Meyrin, Switzerland, `http://cern.ch/`.

[6] B. Henrich et al., *The adaptive gain integrating pixel detector AGIPD, a detector for the European XFEL*, Nucl. Instr. and Meth. A 633 Suppl. 1(2011) S11-S14.

[7] `http://photon-science.desy.de/research/technical_groups/detectors/projects/agipd/`.

[8] J. Becker et al., *Impact of plasma effects on the performance of silicon sensors at an X-ray FEL*, Nucl. Instr. and Meth. A 615 (2010) 230.

[9] H. Graafsma, *Requirements for and development of 2 dimensional X-ray detectors for the European X-ray Free Electron Laser in Hamburg*, 2009 JINST 4 P12011 (2011).

[10] J. Schwandt et al., *Optimization of the radiation hardness of silicon pixel sensors for high x-ray doses using TCAD simulations*, JINST 7 C01006 (2012).

[11] J. Schwandt, *Design of a radiation hard silicon pixel sensor for X-ray science*, PhD thesis, University of Hamburg, in preparation.

[12] The CMS Collaboration, *The CMS experiment at the CERN LHC*, JINST 3 S08004 (2008).

[13] The website of the CMS Experiment at CERN, `http://cms.web.cern.ch`.

[14] J. Lange, *Radiation Damage in Proton-Irradiated Epitaxial Silicon Detectors*, Diploma thesis, University of Hamburg, DESY-THESIS-2009-022 (2008).

[15] Particle Data Group, *Particle Physics Booklet*, `http://pdg.lbl.gov` (2012).

[16] S. M. Sze and Kwok K. NG, *Physics of Semiconductor Devices*, John Wiley & Sons (2007).

[17] M. Moll, *Radiation Damage in Silicon Particle Detectors*, PhD thesis, University of Hamburg, DESY-THESIS-1999-040 (1999).

[18] J. Becker, *Signal development in silicon sensors used for radiation detection*, PhD thesis, University of Hamburg, DESY-THESIS-2010-33 (2010).

[19] T. Pöhlsen, *Charge Collection and Space Charge Distribution in Neutron-Irradiated Epitaxial Silicon Detectors*, Diploma thesis, University of Hamburg, DESY-THESIS-2010-013 (2010).

[20] C. Jacoboni et al., *A review of some charge transport properties of silicon*, Solid-State Electronics, Vol. 20, 77-89 (1977).

[21] J. Becker et al., *Measurements of charge carrier mobilities and drift velocity saturation in bulk silicon of* $\langle 111 \rangle$ *and* $\langle 100 \rangle$ *crystal orientation at high electric fields*, Solid State Electronics, 56 (2011) 104-110.

[22] Z. Li and V. Eremin, *Carrier drift mobility study in neutron irradiated high purity silicon*, Nucl. Instr. and Meth. A 362 (1995) 338-343.

[23] A. Chilingarov et al., *Carrier mobilities in irradiated silicon*, Nucl. Instr. and Meth. A 477 (2002) 287-292.

[24] W. Shockley, *Currents to Conductors Induced by a Moving Point Charge*, J. Appl. Phys. 9 (1938) 635.

[25] S. Ramo, *Currents Induced by Electron Motion*, IRE 27 (1939) 636.

[26] Walter Blum, Werner Riegler and Luigi Rolandi, *Particle Detection with Drift Chambers (Particle Acceleration and Detection)*, Springer (2008).

[27] L.-A. Hamel and M. Julien, *Generalized demonstration of Ramo's theorem with space charge and polarization effects*, Nucl. Instr. and Meth. A 597 (2008) 207.

[28] Helmuth Spieler, *Lectures on Detector Techniques – Semiconductor Detectors Part 1*, `http://www-physics.lbl.gov/~spieler/SLAC_Lectures/PDF/Sem-Det-I.pdf`.

[29] J. Lange et al., *Charge Multiplication Properties in Highly Irradiated Epitaxial Silicon Detectors*, Proceedings of Science (VERTEX 2010) 025.

[30] E. H. Nicollian and J. R. Brews, *MOS (Metal Oxide Semiconductor) Physics and Technology*, John Wiley & Sons (1982).

[31] J. Zhang et al., *Study of radiation damage induced by 12 keV X-rays in MOS structures built on high resistivity n-type silicon*, Journal of Synchrotron Radiation, 19 (2012) 340.

[32] G. Lindström et al., *Radiation hardness of silicon detectors – a challenge from high-energy physics*, Nucl. Instr. and Meth. A 426 (1999) 1.

[33] V. Eremin et al., *The origin of double peak electric field distribution in heavily irradiated silicon detectors*, Nucl. Instr. and Meth. A 476 (2002) 556-564.

[34] V. Eremin et al., *Double peak electric field distortion in heavily irradiated silicon strip detectors*, Nucl. Instr. and Meth. A 535 (2004) 662-631.

[35] G. Lindström, *Radiation damage in silicon detectors*, Nucl. Instr. and Meth. A 512 (2003) 30-43.

[36] J. Erfle, *Radiation damage in silicon sensors*, PhD thesis, University of Hamburg, in preparation.

[37] K. Rajkanan et al., *Absorption coefficient of silicon for solar cell calculations*, Solid-State Electronics, 22, 9, 793-795 (1979).

[38] Advanced Laser Diode Systems A.L.S. GmbH, `http://www.alsgmbh.com/`.

[39] PicoQuant GmbH, Rudower Chaussee 29, D-12489 Berlin, Germany, `http://picoquant.de/`.

[40] H. Kröhnke, *Aufbau eines β-Messstandes zur Untersuchung von Strahlenschäden an Silizium-Sensoren*, Diplomarbeit, University of Hamburg (2012).

[41] T. Poehlsen et al., *Charge losses in segmented silicon sensors at the Si-SiO_2 interface*, Nucl. Instr. and Meth. A 700 (2013) 22-39.

[42] T. Poehlsen et al., *Time dependence of charge losses at the Si-SiO_2 interface in p^+n-silicon strip sensors*, Nucl. Instr. and Meth. A (2013), DOI: 10.1016/j.nima.2013.03.035.

[43] T. Poehlsen et al., *Study of the accumulation layer and charge losses at the Si-SiO2 interface in p^+n-silicon strip sensors*, accepted for publication in Nucl. Instr. and Meth. A, DOI: 10.1016/j.nima.2013.04.026.

[44] Hamamatsu Photonics K.K., `http://www.hamamatsu.com/`.

[45] CiS Forschungsinstitut für Mikrosensorik und Photovoltaik GmbH, Konrad-Zuse-Strasse 14, 99099 Erfurt, Germany, `http://www.cismst.org/`.

[46] J. Zhang, *X-ray Radiation Damage Studies and Design of a Silicon Pixel Sensor for Science at the XFEL*, PhD thesis, University of Hamburg, submitted (2013).

[47] J. Kemmer, *Fabrication of low noise silicon radiation detectors by the planar process*, Nucl. Instr. and Meth. 169 (1980) 499.

[48] J. Kemmer, *Improvement of detector fabrication by the planar process*, Nucl. Instr. and Meth. 226 (1984) 89.

[49] A. Longoni, M. Sampietro and L. Strüder, *Instability of the behaviour of high resistivity silicon detectors due to the presence of oxide charges*, Nucl. Instr. and Meth. A 288 (1990) 35.

[50] R.H. Richter et al., *Strip detector design for ATLAS and HERA-B using two-dimensional device simulation*, Nucl. Instr. and Meth. A 377 (1996) 412.

[51] V. Eremin et al., *The charge collection in single side silicon microstrip detectors*, Nucl. Instr. and Meth. A 500 (2003) 121.

[52] E. Verbitskaya et al., *Effect of SiO2 Passivating Layer in Segmented Silicon Planar Detectors on the Detector Response*, IEEE Transaction on Nuclear Science, vol. 52 no. 5 (2005).

[53] J. Zhang et al., *Study of X-ray Radiation Damage in Silicon Sensors*, JINST 6 C11013 (2011).

[54] H. Perrey, *Jets at Low Q2 at HERA and Radiation Damage Studies for Silicon Sensors for the XFEL*, PhD thesis, University of Hamburg, DESY-THESIS-2011-021 (2011).

[55] H.W. Kraner et al., *The Use of the Signal Current Pulse Shape to Study the Internal Electric Field Profile and Trapping Effects in Neutron Damaged Silicon Detectors*, Nucl. Instr. and Meth. A 326 (1993) 350.

[56] Synopsys TCAD, `http://www.synopsys.com`.

[57] M.M. Atalla, A.R. Bray and R. Lindner, *Stability of thermally oxidized silicon junctions in wet atmospheres*, Proc. IEEE 106 B (1960) 1130.

[58] W. Shockley et al., *Mobile electric charges on insulating oxides with applications to oxide covered p-n junctions*, Surface Science 2 (1964) 277.

[59] A.S. Grove, *Physics and Technology of Semiconductor Devices*, John Wiley & pr (1967).

[60] P.P. Heimann and J.E. Olsen, *A sensitive method for measuring surface conductivity of insulators*, J. Appl. Phys. 53 (1982) 546.

[61] A. Chilingarov, D. Campbell and G. Huges, *Interstrip capacitance stabilization at low humidity*, Nucl. Instr. and Meth. A 560 (2006) 118.

[62] F.G. Hartjes, *Moisture sensitivity of AC-coupled silicon strip sensors*, Nucl. Instr. and Meth. A 5552 (2005) 168.

[63] J. Yorkston et al., *Interstrip surface effects in oxide passivated ion-implanted silicon strip detectors*, Nucl. Instr. and Meth. A 262 (1987) 353.

[64] J. Becker et al., *Simulation and experimental study of plasma effects in planar silicon sensors*, Nucl. Instr. and Meth. A 624 (2010) 715.

[65] Th. Tschentscher for the European XFEL project team, *Layout of the X-Ray Systems at the European XFEL*, XFEL.EU Technical Report (2011), DOI: 10.3204/XFEL.EU/TR-2011-001.

[66] R. Klanner et al., *Challenges for Silicon Pixel Sensors at the European XFEL*, submitted to Nucl. Instr. and Meth. A, and arXiv 1212.5045 (2012).

[67] P.A. Tove and W. Seibt, *Plasma effects in semiconductor detectors*, Nucl. Instr. and Meth. 51 (1967) 261.

[68] ATLAS Collaboration, *The ATLAS Experiment at the CERN Large Hadron Collider*, JINST 3 S08003 (2008).

[69] The website of the ATLAS Experiment at CERN, `http://atlas.web.cern.ch`.

[70] The ATLAS Collaboration, *Observation of a new particle in the search for the Standard Model Higgs boson with the ATLAS detector at the LHC*, Physics Letters B 716 (2012) 1-29.

[71] The CMS Collaboration, *Observation of a new boson at a mass of 125 GeV with the CMS experiment at the LHC*, Physics Letters B 716 (2012) 30-61.

[72] E. Todesco et al., *Energy of the LHC after the 2013–2014 shutdown*, Proceedings of Chamonix 2012 workshop on LHC Performance.

[73] `http://press.web.cern.ch/press-releases/2012/12/first-lhc-protons-run-ends-new-milestone`, CERN Press Office (2012).

[74] Steffen Müller, *The Beam Condition Monitor 2 and the Radiation Environment of the CMS Detector at the LHC*, PhD thesis, University of Karlsruhe, CERN-THESIS-2011-085, CMS-TS-2010-042.

[75] M. Guthoff, PhD thesis, Karlsruher Institut für Technologie, in preparation.

[76] U. Soldevila, *Radiation-hard silicon for LH-LHC trackers*, JINST 6 C12035 (2011).

[77] M. Bruzzi on behalf of the CERN RD50 Collaboration, *Material engineering for the development of ultra-radiation hard semiconductor detectors*, Nucl. Instr. and Meth. A 518 (2004) 336-337.

[78] G. Lindström et al., *Radiation hard silicon detectors – developments by the RD48 (ROSE) collaboration*, Nucl. Instr. and Meth. A 466 (2001) 308-326.

[79] C. Kenney and S. Parker, *Silicon Detectors with 3-D Electrode Arrays: Fabrication and Initial Test Results*, IEEE Transaction on Nuclear Science, vol. 46 no. 4 (1999).

[80] G. Pellegrini et al., *First double-sided 3-D detectors fabricated at CNM-IMB*, Nucl. Instr. and Meth. A 592 (2008) 38-43.

[81] K.-H. Hoffmann, *Campaign to identify the future CMS tracker baseline*, Nucl. Instr. and Meth. A 658 (2011) 30-35.

[82] A. Junkes, *Influence of Radiation Induced Defect Clusters on Silicon Particle Detectors*, PhD thesis, University of Hamburg, DESY-THESIS-2011-031 (2011).

[83] G. Steinbrück for the CMS Tracker Collaboration, *Towards Radiation Hard Sensor Materials for the CMS Tracker Upgrade*, CERN-CMS Conference Report, CR-2012-308 (2012).

[84] A. Dierlamm on behalf of the CMS Tracker Collaboration, *CMS HPK Sensor Characterisation*, Contribution to the 21st International Workshop on Vertex Detector (2012).

[85] A. Barcz et al., *Extremely deep SIMS profiling: oxygen in FZ silicon*, Applied Surface Science 203-204 (2003) 396-399, and private communication.

[86] G. Battistoni et al., *The FLUKA code: Description and benchmarking*, AIP Conference Proceeding 896, 31-49 (2007).

[87] The official FLUKA site, `http://www.fluka.org/`.

[88] J. Stefan Institute, Jamova cesta 39, 1000 Ljubljana, Slovenia, `http://www.ijs.si/`.

[89] ZAG Zyklotron AG, Hermann-von-Helmholtz-Platz 1, D-76344 Eggenstein-Leopoldshafen, Germany, `http://www.zyklotron-ag.de/`.

[90] G. Kramberger, *Signal development in irradiated silicon detectors*, PhD thesis, University of Ljubljana (2001).

[91] T. J. Brodbeck et al., *A new method of carrier trapping time measurement*, Nucl. Instr. and Meth. A 455 (2000) 645-655.

[92] G. Kramberger et al., *Determination of effective trapping times for electrons and holes in irradiated silicon*, Nucl. Instr. and Meth. A 476 (2002) 645-651.

[93] M. Schwartz et al., *Observation, modeling, and temperature dependence of doubly peaked electric fields in irradiated silicon pixel sensors*, Nucl. Instr. and Meth. A 565 (2006) 212-220.

[94] M. Huhtinen, *Simulation of non-ionising energy loss and defect formation in silicon*, Nucl. Instr. and Meth. A 491 (2002) 194-215.

Acknowledgements

Most of all I want to thank my doctoral father Robert Klanner for his excellent supervision. Especially for the possibility to publish three papers, together with him and my other colleagues, which are now part of this thesis. Robert Klanner's critical and accurate view on both the measurements and the written texts made the papers and the understanding of the observed effects to what they are today. Also I am thankful to the other co-authors for the great collaboration, especially to Joern Schwandt who performed the extremely helpful device simulations and to Eckhart Fretwurst for his accurate inspections. Further, I am thankful to Helmuth Spieler for inspiring discussions and to the unknown referees of the peer-review processes for useful comments which helped to improve the clearity of the papers significantly.

I am also very thankful to the other members of the examination board, to Heinz Graafsma for being willing to act as a referee for this thesis, to Erika Garutti and Eckhard Elsen for being willing to act as referees for the thesis defence, and to Georg Steinbrueck for chairing the examination board.

Many thanks also belong to my colleagues of the detector-laboratory group who are involved in the pad-sensor measurements. Especially to Joachim Erfle for the coordination of the irradiations, the annealing and the capacitance and current measurements, and for providing data extracted in sophisticated ways from the database, to Peter Buhmann for his technical support with the experimental setups and for his supervision of the student assistants, and to the student assistants for performing so many measurements, especially to Evangelos, Jascha and Marc who performed most of the TCT measurements on pad sensors which are discussed in this thesis. I am also very thankful to Erika Garutti and Georg Steinbrueck for their support and comments.

Also I am thankful for the help of my family, especially to my brother Stephan for suggestions on the thesis layout, and to my fiancée Jennifer for her constructive feedback on both my English and the way of presenting. And finally I want to give thanks to the living God for the development of all the effects investigated and for making life as enjoyable as it is.

Kapitel 1, 2, 3, 4.1, 4.5, 5 und 6 habe ich selbstständig verfasst. Kommentare von meinem Betreuer Prof. Dr. Robert Klanner sowie von weiteren Mitarbeitern des Instituts habe ich berücksichtigt.

Bei Kapitel 4.2, 4.3 und 4.4 handelt es sich um drei gemeinschaftliche Arbeiten, die im Journal Nucl. Instr. and Meth. A veröffentlicht oder zur Veröffentlichungen akzeptiert wurden. Bei den drei Veröffentlichungen bin ich sowohl Erstautor als auch Kontaktperson. Die Ladungssammlungsmessungen und deren Beschreibung durch Modellrechnungen habe ich durchgeführt. Diese Messungen sind der zentrale Teil der experimentellen Arbeit der Veröffentlichungen. Ebenso habe ich die Messungen der Streifenströme bei verschiedenen Luftfeuchten und Spannungshistorien durchgeführt.

Die für die Diskussion wesentlichen Sensorsimulationen hat Jörn Schwandt durchgeführt und die Röntgenbestrahlung der untersuchten Sensoren sowieso Messungen an Gate-Kontrollierten Dioden hat Jiaguo Zhang durchgeführt.Der Text wurde sowohl durch mich, als auch durch Prof. Dr. Robert Klanner editiert. Kommentare weiterer Autoren sowie der unbekannten Gutachter des Peer-Review-Prozesses wurden berücksichtig.

Hiermit versichere ich, dass ich keine anderen als die angegebenen Quellen und Hilfsmittel verwendet habe.

Mit der Ausleihe dieser Arbeit bin ich einverstanden.

Thomas Pöhlsen, Hamburg den 26. April 2013